DESIGN AND ANALYSIS OF AN ATTITUDE DETERMINATION AND

CONTROL SUBSYSTEM (ADCS) FOR AFIT'S 6U STANDARD BUS

THESIS

Erin R. Dannemeyer, Second Lieutenant, USAF

AFIT-ENY-14-M-14

DEPARTMENT OF THE AIR FORCE
AIR UNIVERSITY

AIR FORCE INSTITUTE OF TECHNOLOGY

Wright-Patterson Air Force Base, Ohio

AFIT-ENY-14-M-14

DESIGN AND ANALYSIS OF AN ATTITUDE DETERMINATION AND CONTROL SUBSYSTEM (ADCS) FOR AFIT'S 6U STANDARD BUS

THESIS

Presented to the Faculty

Department of Aeronautical and Astronautical Engineering

Graduate School of Engineering and Management

Air Force Institute of Technology

Air University

Air Education and Training Command

in Partial Fulfillment of the Requirements for the

Degree of Master of Science in Astronautical Engineering

Erin R. Dannemeyer, B.S.A.E.

Second Lieutenant, USAF

March 2014

AFIT-ENY-14-M-14

DESIGN AND ANALYSIS OF AN ATTITUDE DETERMINATION AND CONTROL SUBSYSTEM (ADCS) FOR AFIT'S 6U STANDARD BUS

Erin R. Dannemeyer, B.S.A.E.
Second Lieutenant, USAF

Approved:

//signed//	7 March 2014
Richard G. Cobb, PhD (Chairman)	Date
//signed//	7 March 2014
Bradley J. Ayres, PhD (Member)	Date
//signed//	7 March 2014
Eric D. Swenson, PhD (Member)	Date

AFIT-ENY-14-M-14

Abstract

The design and testing of Air Force Institute of Technology (AFIT)'s 6U Attitude Determination and Control Subsystem (ADCS) are explored to establish 3-axis attitude control. The development of AFIT's 6U CubeSat standard bus is an on-going research effort designed to create in-house CubeSat bus components and software. The 6U chassis measures approximately 11 x 24 x 37 cm^3 and can have a mass up to 12 kg. The larger bus size (as compared to the more common 3U CubeSat) allows for increased power capabilities and potential to host multiple or larger payloads. Individual ADCS hardware components were either commercially purchased or built in-house and include an Inertial Measurement Unit (IMU), external magnetometer, 4-wheel reaction wheel assembly, and three torque coils. The ADCS software developed as part of this research includes the Quaternion Estimator (QUEST) attitude determination algorithm, B-dot de-tumbling algorithm, and Proportional-Derivative (PD) control algorithm with momentum dumping capability. To facilitate ADCS testing, an air bearing assembly was designed and set up in AFIT's existing Helmholtz cage. The air bearing provides a near-frictionless environment with 360° rotation about one axis and limited (35°) rotations about the other two axes. The Helmholtz cage consists of three orthogonal magnetic coil pairs that can create a uniform ±2 Gauss magnetic field within the cage. This comprehensive ADCS testing environment was used to test a ground-based 6U CubeSat complete with ADCS, Command and Data Handling (CDH), and Electrical Power Subsystem (EPS) components. The custom-built torque coils demonstrated torquing abilities on the spacecraft and yield a 0.66 A-m^2 magnetic moment. In addition, single-axis attitude control was achieved using the reaction wheel assembly. Recommendations for further developments and testing are included to achieve the desired 3-axis control.

To my future husband who endured many lonely nights while I was working and my family who understood missed phone calls and sleepy visits

Acknowledgments

First and foremost, this thesis was a team effort. I would nowhere without the guidance and help of my mechanical and software teams. From the mechanical side, thank you to Philip Smith and the personnel at the machine shop for making this project a reality. Philip Smith is a CAD genius and can perfectly model what I have drawn out in my head. The personnel at the machine shop, in particular Brian and Chris, did not stop until the air bearing was the best it could be. I cannot tell you how grateful I am that you stuck with the idea of a hand-crank lift. From the software side, huge shout-out to Matt Lippert for being my software right-hand man. We would not have achieved control without you.

Thank you to my advisor, Dr. Cobb. Despite the schedule slips and government shutdown, you continued to push me to do my best. Thank you for your guidance and help along the way. And to Dr. Swenson, every tidbit of advice is like a golden nugget falling into my hand. Thank you for your excitement in this project and for making sure I was doing the right thing.

The team effort all started during the summer with ASYS 632. Thank you Warren Grunwald and Evelyn Abbate for starting this research with me. Your dedication and commitment was invaluable in getting the project where it is today. Thank you to the entire "army of interns" who developed the MATLAB ground station, C&DH, and EPS boards. There are no words to express how convenient it was to command the spacecraft and collect data once I was ready for ADCS testing.

Finally, thank you to my classmates in ENY-3. The camaraderie we built together trumps the dynamics in any other section at AFIT. Thank you for your continued support, especially late into the nights and early in the mornings.

Erin R. Dannemeyer

Table of Contents

List of Figures

List of Tables

List of Symbols

Symbol   Definition

v	3 x 1 vector
R^{ba}	Direction Cosine Matrix
$\hat{b}$	body frame unit vector
$\hat{i}$	inertial frame unit vector
θ_{ab}	angle between two vectors (a and b)
a	3 x 1 Euler axis vector
Φ	Euler angle (rad)
q	4 x 1 quaternion array ($q_4^2 = q_1^2 + q_2^2 + q_3^2$)
J	Wahba's loss function
w_k	measurement weight
g	gain function
λ	eigenvalue
K	eigenvector matrix (QUEST)
B	QUEST sub-matrix
S	QUEST sub-matrix
Z	QUEST sub-matrix
σ	trace of QUEST sub-matrix
p	3 x 1 Rodriguez parameters vector
I	identity matrix
ω	3 x 1 spacecraft angular velocity vector (rad/s)
M	3 x 1 external torque vector (N-m)
H	3 x 1 angular momentum vector (N-m-s)
I	3 x 3 moment of inertia tensor (kg-m^2)

Symbol	Definition
$\boldsymbol{B}$	3 x 1 magnetic field vector (mG)
N	number of turns
I	current (A)
a	radius of a magnetic coil (m)
$\boldsymbol{T}$	3 x 1 torque vector (N-m)
$\boldsymbol{M}$	3 x 1 magnetic dipole moment vector (A-m^2)
A	cross-sectional area of solenoid (m^2)
$\boldsymbol{D}$	3 x 1 wheel moment of inertia array (kg-m^2)
$\boldsymbol{\psi}$	3 x 1 wheel angular velocity vector (rad/s)
k	control gain
$\boldsymbol{M}_O$	3 x 1 maximum magnetic dipole vector (A-m^2)
$\boldsymbol{q}_E$	4 x 1 quaternion error array

Subscripts

p	proportional gain
d	derivative gain

Superscripts

b	body reference frame
i	inertial reference frame

List of Acronyms

Acronym	Definition
ADCS	Attitude Determination and Control Subsystem
AFIT	Air Force Institute of Technology
API	Advanced Photonix, Inc.
AWG	American Wire Gauge
AWSS	Autonomous Wireless Sun Sensor
CAD	Computer-Aided Design
CDH	Command and Data Handling
COM	Center of Mass
COTS	Commercial Off-the-Shelf
CSRA	Center for Space Research and Assurance
DAC	Digital-to-Analog Converter
DCM	Direction Cosine Matrix
DOF	degrees of freedom
ECEF	Earth-Centered Earth-Fixed
ECI	Earth-Centered Inertial
EDU	Engineering Development Unit
EKF	Extended Kalman Filter
EPS	Electrical Power Subsystem
FDI	Fault Detection and Isolation
GUI	Graphical User Interface
IGRF	International Geomagnetic Reference Field
IMU	Inertial Measurement Unit
IR	infrared

Acronym	Definition
IVR	Inertial Value Reset
LEO	Low Earth Orbit
LTP	Local Tangent Plane
MATLAB	Matrix Laboratory
MEDA	Macintyre Electronic Design Associates
MEMS	Microelectromechanical System
MIT	Massachusetts Institute of Technology
MOI	moment of inertia
NED	North-East-Down
NPS	Naval Postgraduate School
NTNU	Norwegian University of Science and Technology
NUTS	NTNU Test Satellite
PD	Proportional-Derivative
PWM	Pulse Width Modulation
QUEST	Quaternion Estimator
RAX	Radio Aurora Explorer
RPM	revolutions per minute
RPY	Roll-Pitch-Yaw
RWA	Reaction Wheel Assembly
SEET	Space Environment and Effects Tool
SNU	Seoul National University
STK	Systems Tool Kit
SWAP	Size, Weight, and Power
TFSC	Thin Film Solar Cells
TLE	Two Line Elements

Acronym	Definition
TRIAD	Tri-Axial Attitude Determination System
TU Delft	Delft University of Technology
U-M	University of Michigan
UNAM	National Autonomous University of Mexico
WMM	World Magnetic Model

DESIGN AND ANALYSIS OF AN ATTITUDE DETERMINATION AND CONTROL SUBSYSTEM (ADCS) FOR AFIT'S 6U STANDARD BUS

I. Introduction

1.1 Background

The AFIT's Center for Space Research and Assurance (CSRA) hosts a number of on-going, defense-related research projects. One class of projects is the development and utilization of a 6U CubeSat. A CubeSat is a nanosatellite (of various sizes and typically < 10 kg) intended for low-cost experimental research. CubeSats are primarily built by university programs over the course of 1-2 years (and sometimes longer) [50]. CubeSats are appealing to sponsors due to their low-cost experiment life cycle. Oftentimes, CubeSats have little to no redundancy. Because of this, the cost of a CubeSat program is kept low by accepting mission risk. In addition, CubeSat missions rarely have to deal with significant launch costs because they are secondary payloads. As long as the launch vehicle is outfitted with a CubeSat dispenser, there are opportunities of finding a ride to orbit.

The size of CubeSats are often identified by the number of "U"s. A CubeSat "U" refers to a volumetric unit that holds one liter. A standard 1U CubeSat is 10 x 10 x 10 cm^3 with a mass no greater than 1.33 kg [50]. Most CubeSats are either 1U or 3U, but larger CubeSats are becoming commonplace. Recently, AFIT's research focuses on 6U CubeSats. 6U CubeSats have increased payload capabilities and can support larger solar arrays, which is useful when more power is required to operate the payload (or potentially multiple payloads). In total, the 6U CubeSat can weigh no more than 12 kg. Figure 1.1 shows AFIT's aluminum 6U chassis, which weighs approximately 2 kg. The 6U chassis

accommodates a number of "stack" configurations, where a "stack" refers to a 1U unit that houses one or many components (i.e. batteries and an EPS board in one stack). Each stack can fit within a 1U space in 24 different configurations.
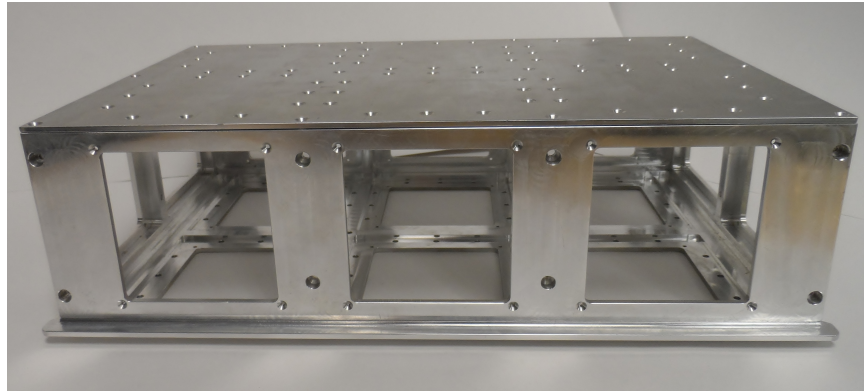
Figure 1.1: 2013 AFIT 6U Chassis

Every academic year since 2008, the Center for Space Research and Assurance offers a space vehicle design sequence for Master's and PhD students at AFIT. The sequence contains three classes that build upon each other. The first class, ASYS 531, focuses on systems engineering and the initial design phase of a satellite program. Students are divided into teams and given a conceptual mission from a sponsor (with the constraint of using a 6U CubeSat). Throughout the 10-week quarter, students develop the mission to about the System Definition Review level, as defined by the NASA Systems Engineering Handbook [35]. By the end of the quarter, each team presents their initial solution to a group of instructors and industry leaders. From there, students transition to ASYS 631 while keeping their same project teams. ASYS 631 focuses on subsystem analysis and design. At course completion, the students' design is intended to be between the Preliminary Design Review and Critical Design Review levels (given the same 10-week time constraint). Same as before, each team presents their solution to a group of

instructors and industry leaders, gaining invaluable feedback for the next stage of development.

The last course in the space vehicle design sequence is ASYS 632. ASYS 632 shifts focus from paper design and analysis to hardware building and testing. The goal of the course is to design, build, and test an Engineering Development Unit (EDU), a 6U CubeSat prototype that is capable of meeting some of its mission goals. The students gain invaluable experience in hardware design, software development, and spacecraft integration. They take their initial mission and turn it into a functioning prototype satellite in a matter of only 10 weeks.

The over-arching goal of the space vehicle design sequence is to achieve a high standard of development and design that enables a smooth transition from an EDU to a flight-ready satellite. By establishing an inventory of custom built, in-house standard bus components along with the spacecraft chassis, it is envisioned that students can integrate the sponsor's payload with relative ease and allow a more thorough development of the payload (vice the bus). By the end of the sequence, the sponsor can choose for AFIT to continue with their particular CubeSat mission, potentially bringing the mission all the way through launch and into satellite operations.

1.2   Problem Statement

The Attitude Determination and Control Subsystem (ADCS) needs to be designed, built, and tested as part of the overall goal of developing in-house CubeSat bus components. The ADCS for AFIT's 6U CubeSat should be able to accommodate a variety of missions that can work in Low Earth Orbit (LEO). Although a number of stabilization and control techniques are used on satellites, the AFIT CubeSat ADCS research will focus specifically on a 3-axis ADCS.

A handful of Commercial Off-the-Shelf (COTS) ADCS packages are available on the market today. As a point of comparison and a requirement specified by the AFIT faculty,

3

the AFIT-built ADCS will be capabilities-matched against the COTS MAI-400 from Maryland Aerospace [6]. The goal is to produce a system that is just as capable, if not more, than the systems available today at a significantly reduced cost by leveraging AFIT's in-house design, manufacture, and assembly capabilities.

1.3   ADCS Requirements

This research will produce and test a complete ADCS for any 3U CubeSat or larger developed by the Center for Space Research and Assurance, with a focus on ADCS performance in the 6U CubeSat form. Although 3-axis CubeSat attitude control systems have been designed and tested before at other institutions, this is not a trivial task and will take a few years to complete. Several requirements need to be met in order for AFIT's ADCS to serve as a replacement for any COTS ADCS package. The requirements that will be focused on for this specific thesis are marked with an asterisk and described in more detail in the next section. The ADCS requirements include [29]:

Functional

1. Inertially sense spacecraft attitude using at least magnetometers, Sun sensors, and Earth sensors*

2. Be capable of dumping momentum through the use of external torquers (preferably without propulsion)*

3. Demonstrate ability to de-tumble spacecraft*

4. Test sun-pointing control mode

5. Demonstrate nadir-pointing control mode

6. Test inertial and body vector alignment

Performance and Size, Weight, and Power (SWAP)

7. Filter measurement noise to establish attitude knowledge within 0.1° (3-σ)

8. Test reaction wheels control of the spacecraft to within 1° (3-σ)

9. Have total ADCS power requirement no greater than 5 W*

10. Have total ADCS mass requirement no greater than 1.5 kg*

11. Fit reaction wheel assembly and ADCS circuit board within 1U*

Interface

12. Integrate ADCS with AFIT 6U CDH and EPS*

13. Demonstrate ADCS components can survive launch environment

1.4 Research Focus

The primary objective of this thesis is to continue the development of ADCS components and demonstrate at least 1-axis control of AFIT's 6U CubeSat including momentum dumping capabilities. The marked requirements in the previous section provide research direction, but will not necessarily be 100% complete by the end of the thesis period. Spacecraft attitude will be determined through the use of magnetometers with the intent of integrating Sun and Earth sensors in future work. Torque coils will be built, providing necessary capabilities for momentum dumping and spacecraft de-tumbling. Previous research developed a four-wheel reaction wheel assembly capable of producing an estimated 15 mN-m torque in each axis. The reaction wheels will be tested to assess pointing accuracy and the current capabilities of AFIT's 6U CubeSat. To facilitate some of the performance requirements, the research will include a spacecraft simulation environment using Simulink and the development of a comprehensive ADCS test environment. This thesis will also focus on designing the ADCS within SWAP

constraints. ADCS development and design will integrate with the 6U CDH and EPS as much as possible by utilizing previously developed CDH and EPS components along with a MATLAB ground station. The ADCS components developed and tested during this thesis are intended for ground use only and do not include space-rated hardware.

1.5 Methodology

To test the 6U CubeSat ADCS's pointing accuracy, an air bearing will be used. The air bearing provides minimal friction, full range of movement in one axis, and limited movement in the other two axes. The air bearing will support the ADCS testbed, which includes all ADCS components in a 6U chassis along with CDH and EPS components. The air bearing will be placed inside a Helmholtz cage [9]. The Helmholtz cage produces a nearly uniform magnetic field in the center of the cage and can be used to simulate the magnetic field the satellite would experience on-orbit. This ensures performance with flight-representative measurements from the magnetometers for attitude determination. The test results will be compared with simulated results and ultimately judged against the MAI-400 ADCS capabilities.

1.6 Assumptions and Limitations

Many assumptions, and consequently some corresponding limitations, are taken in order to develop the ADCS as much as possible given the research time constraint. First of all, the reaction wheel assembly is assumed to be in good, working order in terms of on-the-ground functionality. No mechanical design changes will be made to the existing reaction wheel assembly, and all work with the reaction wheels will focus on obtaining a desired level of control. However, it is known that the current design for the reaction wheel assembly is not capable of surviving random vibration testing. In the long term, the reaction wheel assembly will need to be mechanically redesigned in order to survive the launch environment. Second, it is assumed that different attitude sensors will be

incorporated with the satellite for the final product. For this research, attitude determination will be estimated by combining an IMU and external magnetometer measurements only in order to focus on other aspects of the ADCS design. The Helmholtz cage is assumed to have orthogonal magnetic coil pairs that produce a uniform magnetic field in the center (test section area) of the cage, although the uniformity of the cage has not been tested since its relocation from another lab within AFIT. Also, the air bearing is assumed to operate as a frictionless surface that is not subject to minute external torques from the test equipment environment (i.e. air blowing into the room, vibrations from the ground or walls, etc.). It is assumed that CDH and EPS components and software provide the necessary transmit/receive functions and power to the ADCS board. No further work on the CDH and EPS boards will be done as part of this research effort.

1.7   Preview

This chapter provided the motivation and overview of the research along with research assumptions and limitations. Chapter II details the background necessary to design an ADCS. This includes a mathematical and theoretical review of ADCS concepts along with a related research review of ADCS design and test equipment developed by other universities and research institutions. Chapter III describes the methodology behind designing and testing the ADCS for AFIT's 6U CubeSat. The chapter will focus on sensor and actuator design, the ADCS algorithms coded on-board the spacecraft, a Simulink model used to analyze spacecraft behavior, and the air bearing design. The chapter also describes the CubeSat used for testing and gives an overview of ADCS experimental tests. Chapter IV presents and analyzes the experimental test results for both attitude determination and attitude control. In addition, Chapter IV compares the current capabilities of AFIT's ADCS with the specifications of the MAI-400. Lastly, Chapter V summarizes the findings of this research and offers recommendations for future work to take the ADCS towards its next stages of development.

II. Background

Chapter II describes the background of attitude determination and control. This includes spacecraft coordinate frames, attitude representations, attitude determination algorithms, and satellite dynamics. In addition, the chapter focuses on related ADCS research efforts performed within the past few years. In particular, the related research section explores ADCS computer models, magnetic-field producing Helmholtz cages, and spherical air bearings.

2.1   Attitude Determination and Control Background

The following section discusses the general theory and mathematics behind attitude determination and control. First, various spacecraft coordinate frames are described in addition to the representation of a spacecraft's attitude. Second, the QUEST algorithm shows how to use sensor measurements to determine the spacecraft's attitude. Then, an overview of satellite dynamics is described, along with a brief discussion on magnetic field models.

2.1.1   Coordinate Frames.

When dealing with objects moving within a moving reference (i.e. a moving satellite rotating about the Earth), it is simplest to comprehend and analyze the object's movement through the use of coordinate frames. Coordinate frames provide a means to easily define an object's orientation with respect to some inertial frame of reference (the object's *attitude*). Coordinate frames are essential for successful attitude determination and control. The following frames are discussed in detail - ECI, ECEF, NED, orbital, and body-fixed. Each coordinate frame consists of three orthogonal unit vectors that are fixed to some frame of reference and are either inertial or non-inertial.

Earth-Centered Inertial (ECI)

The ECI coordinate frame is an inertial frame with its origin at the center of the Earth. Shown in Figure 2.1, the x-axis points in the direction of the vernal equinox, the z-axis points in the direction of true North, and the y-axis completes the right-handed orthogonal system [22]. The ECI frame is most commonly used for orbit analysis and inertial motion [50].
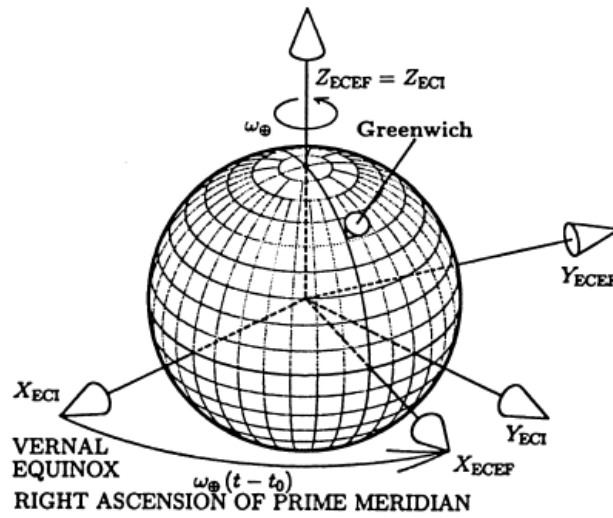
Figure 2.1: ECI and ECEF Coordinate Frames [22]

Earth-Centered Earth-Fixed (ECEF)

The ECEF coordinate frame is a non-inertial frame with its origin at the center of the Earth. The ECEF frame moves with the rotation of the Earth about its z-axis, as shown in Figure 2.1. The x-axis points in the direction of the Prime Meridian, the z-axis points in the direction of true North, and the y-axis completes the right-handed orthogonal system [22]. The ECEF frame is most commonly used for geolocation and apparent satellite motion [50].

The NED coordinate frame is a Local Tangent Plane (LTP) frame with its origin at a point on or above the Earth's surface (usually fixed to a vehicle). LTP coordinates refer to a set of local reference directions assuming a first-order, flat model of Earth [22]. As shown in Figure 2.2, the x-axis points in the direction of geodetic North, the y-axis points in the direction of geodetic East, and the z-axis completes the right-handed orthogonal system [11].
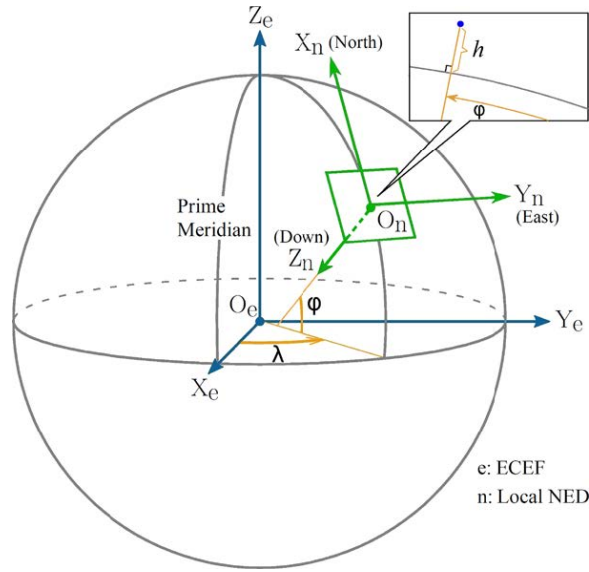
Figure 2.2: North-East-Down Coordinate Frame [11]

Orbital Frame

The orbital coordinate frame, also referred to as the Roll-Pitch-Yaw (RPY) frame, is centered on the spacecraft and changes as the satellite moves about its orbit. As shown in Figure 2.3, the z-axis (yaw) points in the direction of nadir, the y-axis (pitch) points in the direction of the negative orbit normal, and the x-axis (roll) completes the right-handed orthogonal system. When the orbit is circular, the x-axis points in the direction of the spacecraft velocity vector [50].
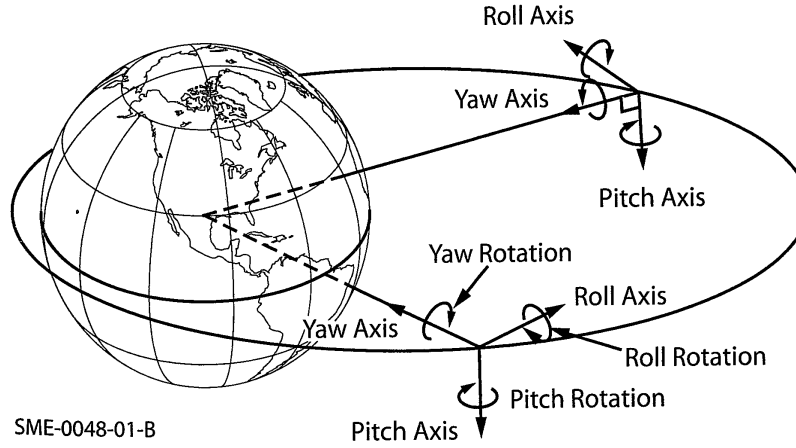
Figure 2.3: Orbital (RPY) Coordinate Frame [50]

Spacecraft-Fixed Frame

The spacecraft-fixed, or body, frame of any vehicle is a user-defined coordinate frame. The body frame's origin is often defined at the Center of Mass (COM) of the spacecraft with its axes pointing in the direction of the principal axes [43]. However, any direction can be chosen, as long as the frame is right-handed orthogonal. In addition, many objects on the spacecraft have their own body-fixed coordinate system. For example, an IMU has its own coordinate frame as defined by how the sensor hardware was put together.

2.1.2 Attitude Representations.

An object's attitude is the orientation of the object with respect to some inertial frame. The relationship between the object (body) and the inertial frame is represented by a rotation matrix. A rotation matrix transforms a vector between coordinate frames. For example, a 3 x 1 vector is known in the inertial frame (v_i), but it is desired to know the vector in the body frame (v_b). The rotation matrix R^{bi} gives the relationship between the

11

three orthogonal axes in the inertial frame and the three orthogonal axes in the body frame (forming a 3 x 3 matrix).

$$v_b = \boldsymbol{R}^{bi} v_i \tag{2.1}$$

A rotation matrix is synonymous with a Direction Cosine Matrix (DCM). Looking at Eq. 2.1, in order to isolate and find $\boldsymbol{R}^{bi}$, the transpose of v_i must by post-multiplied on both sides of the equation. In Eq. 2.2, by just looking at the directions $(\hat{i}, \hat{b})$ of the two vectors (and not the magnitudes), the rotation matrix simply becomes the dot product between the two direction vectors.

$$\boldsymbol{R}^{bi} = \begin{bmatrix} \hat{b}_1 \\ \hat{b}_2 \\ \hat{b}_3 \end{bmatrix} \cdot \begin{bmatrix} \hat{i}_1 & \hat{i}_2 & \hat{i}_3 \end{bmatrix} \tag{2.2}$$

The dot product is defined as $a \cdot b = |a| \, |b| \cos \theta_{ab}$, where θ_{ab} is the angle between the two vectors. Since the magnitude of $\hat{b}$ and $\hat{i}$ are both one (unit vectors), then the rotation matrix is simply the cosine between each direction [43]. The complete DCM is defined in Eq. 2.3 below.

$$\boldsymbol{R}^{bi} = \begin{bmatrix} \cos \theta_{b_1 i_1} & \cos \theta_{b_1 i_2} & \cos \theta_{b_1 i_3} \\ \cos \theta_{b_2 i_1} & \cos \theta_{b_2 i_2} & \cos \theta_{b_2 i_3} \\ \cos \theta_{b_3 i_1} & \cos \theta_{b_3 i_2} & \cos \theta_{b_3 i_3} \end{bmatrix} \tag{2.3}$$

As shown in Eq. 2.4, since DCMs consist of orthonormal vectors, the inverse of a DCM is the same as its transpose. In addition, the rotation between two frames that seem mutually exclusive can be found by knowing the rotations with an intermediary frame, as in Eq. 2.5.

$$\left(\boldsymbol{R}^{ba} \right)^{-1} = \left(\boldsymbol{R}^{ba} \right)^{T} = \boldsymbol{R}^{ab} \tag{2.4}$$

$$\boldsymbol{R}^{ca} = \mathbf{R}^{cb} \boldsymbol{R}^{ba} \tag{2.5}$$

There exist a number of ways to represent a spacecraft's rotation with respect to an inertial frame. Three representations in particular are described in the following paragraphs and summarized in Table 2.1.

Euler angles consist of a sequence of three simple rotations to describe the spacecraft's attitude [42]. A simple rotation consists of a rotation about a single axis. As Table 2.1 describes, rotations about the 1, 2, and 3 axes keep the respective axis stationary while the other two axes rotate about that axis. For example, Figure 2.4 shows a 3-1-3 Euler angle sequence, where x, y, and z correspond with 1, 2, and 3. The first rotation
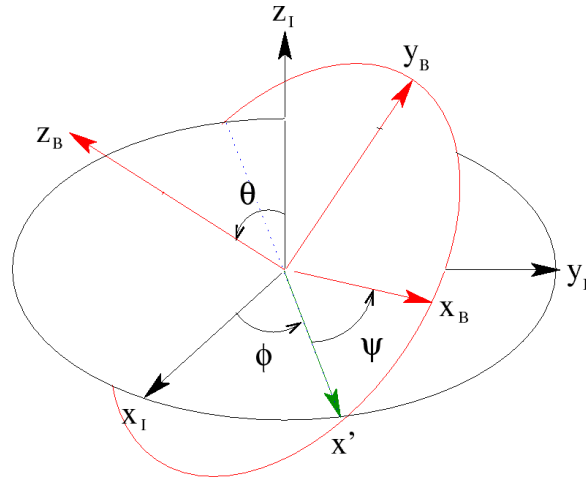
Figure 2.4: Example Euler Angle Rotation Sequence (3-1-3) [8]

rotates x_I and y_I about the z_I (3) axis ϕ degrees. The new, intermediary axis rotates about the x' (1) axis θ degrees. The third rotation rotates about the z_B (3) axis ψ degrees so that the final frame is the orthogonal x_B, y_B, and z_B frame. The mathematical notation for this Euler angle is defined in Eq. 2.6:

$$\begin{bmatrix} x_B \\ y_B \\ z_B \end{bmatrix} = R_3(\psi)R_1(\theta)R_3(\phi) \begin{bmatrix} x_I \\ y_I \\ z_I \end{bmatrix} \tag{2.6}$$

13

Since each rotation is spatially-based, the order of rotations makes a difference. $R_3(\phi)R_1(\theta)R_3(\psi)$ is not the same as $R_3(\psi)R_1(\theta)R_3(\phi)$, unless ψ and ϕ are the same angle.

Even though Euler angles are rather intuitive, the process is subject to singularities. An Euler angle singularity can occur when finding the rotation angle from the DCM. The DCM to Euler angle process requires knowledge of the sequence used to produce the DCM in the first place. Looking at the example above, when multiplied out, a 3-1-3 Euler angle sequence becomes:

$$R^{BI} = \begin{bmatrix} c\psi c\phi - s\psi c\theta s\phi & s\psi c\phi + c\psi c\theta s\phi & s\theta s\phi \\ -c\psi s\phi - s\psi c\theta c\phi & -s\psi s\phi + c\psi c\theta c\phi & s\theta c\phi \\ s\psi s\theta & -c\psi c\theta & c\theta \end{bmatrix} \tag{2.7}$$

The simplest way to find ϕ, θ, and ψ from Eq. 2.7 is to compute the following equations:

$$\theta = \cos^{-1}(R_{33}) \tag{2.8}$$

$$\phi = \tan^{-1}\left(\frac{R_{13}}{R_{23}}\right) \tag{2.9}$$

$$\psi = \tan^{-1}\left(-\frac{R_{31}}{R_{32}}\right) \tag{2.10}$$

When $R_{33} = 1$, θ can be either $0°$ or $180°$, and when $R_{33} = 0$, θ can be either $90°$ or $270°$, therefore creating a singularity. For sequences that are symmetric (i.e. 3-1-3), a singularity occurs when the middle angle is either $0°$ or $180°$. For asymmetric sequences (i.e. 1-2-3), a singularity occurs when the middle angle is $90°$ [42].

Another attitude representation is Euler axis, or Eigenaxis, rotations. An Euler axis is a fixed, single axis, *a*, by which the object rotates about by the principal Euler angle, Φ. The Euler axis goes through the origin of both the inertial and body frames. Figure 2.5 demonstrates a type of Euler axis rotation.

The Euler axis is an eigenvector of the rotation matrix because the Euler axis is the same for the inertial and body frames. *a* and Φ are used to define the inertial-to-body rotation matrix as described in Table 2.1. The table also describes how to extract the Euler

14
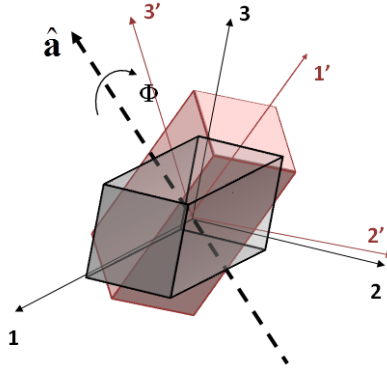
Figure 2.5: Eigenaxis Rotation about Φ

axis and principal Euler angle from the DCM. The Euler axis approach has four parameters, but only three of these are independent. Therefore, the unit vector constraint listed in Table 2.1 is necessary to fully define the Euler parameters [42].

Euler axis rotations provide simpler means of solving for the rotation matrix than Euler angles because less variables are involved. Nonetheless, Euler axis rotations are also subject to singularities. The Euler axis becomes undefined when $\sin \Phi = 0$. Although the Euler axis approach is a good attitude representation, there is a better approach described next which does not involve singularities [42].

A third attitude representation method is quaternions, or Euler parameters. Quaternions create a 4x1 vector defined by Euler axis parameters, as defined in Table 2.1. Quaternions fully describe the rotation of an object while at the same time avoiding singularities. Similar to the Euler axis representation, quaternions also have the unit vector constraint because there are four parameters with only three independent parameters. Therefore, each quaternion value is bounded within ±1 [42]. The primary disadvantage of quaternions is their lack of rotation visualization/intuitiveness. Oftentimes, users will work with quaternions to determine the rotation matrix and then convert to Euler angles to easily understand how the object is oriented.

Table 2.1: Attitude Representations

Representation	Variables	Variables to DCM	DCM to Variables	Singularities & Constraints
Euler Angles	$R_i(\theta_3)R_j(\theta_2)R_k(\theta_1)$ $i, j, k = 1, 2,$ or 3	$R_1(\theta) = \begin{bmatrix} 1 & 0 & 0 \\ 0 & c\theta & s\theta \\ 0 & -s\theta & c\theta \end{bmatrix}$ $R_2(\theta) = \begin{bmatrix} c\theta & 0 & -s\theta \\ 0 & 1 & 0 \\ s\theta & 0 & c\theta \end{bmatrix}$ $R_3(\theta) = \begin{bmatrix} c\theta & s\theta & 0 \\ -s\theta & c\theta & 0 \\ 0 & 0 & 1 \end{bmatrix}$	Solve for isolated angle in DCM, then solve for the other two angles using the first angle. Do not forget to perform a quadrant check.	Singularity: • If sequence is symmetric (i.e. 3-1-3), $\theta_2 = 0°$, 180° • If sequence is asymmetric (i.e. 3-2-1), $\theta_2 = 90°$ No constraints
Euler Axis	a – 3 x 1 eigenaxis vector Φ – principal Euler angle	$R^{bi} = \cos\Phi\, \mathbf{1} + (1 - \cos\Phi)aa^T - \sin\Phi\, a^\times$	$\Phi = \cos^{-1}\left[\frac{1}{2}(trace(R) - 1)\right]$ $a^\times = \frac{1}{2\sin\Phi}(R^T - R)$	Singularity: $\sin\Phi = 0$ Constraint: $a^T a = 1$
Quaternion	$q = [\vec{q} \quad q_4]$ $\vec{q} = a\sin\left(\frac{\Phi}{2}\right)$ $q_4 = \cos\left(\frac{\Phi}{2}\right)$	$R^{bi} = (q_4^2 - \vec{q}^T\vec{q})\mathbf{1} + 2\vec{q}\vec{q}^T - 2q_4 q^\times$	$q_4 = \pm\frac{1}{2}\sqrt{1 + trace(R)}$ $\vec{q} = \frac{1}{4q_4}\begin{bmatrix} R_{23} - R_{32} \\ R_{31} - R_{13} \\ R_{12} - R_{21} \end{bmatrix}$	No singularity: When $q_4 = 0$, $q_n = \pm\sqrt{\dfrac{R_{nn} + 1}{2}}$ $n = 1, 2,$ or 3 (Note sign ambiguity) Constraint: $q^T q = 1$

$$a^\times = \begin{bmatrix} 0 & -a_3 & a_2 \\ a_3 & 0 & -a_1 \\ -a_2 & a_1 & 0 \end{bmatrix}$$

2.1.3   QUEST Algorithm.

Two types of attitude determination algorithms exist - deterministic and statistical (state estimation) attitude determination. Deterministic attitude determination uses the same number of observations as variables to determine a discrete attitude solution [49]. A common deterministic algorithm is the Tri-Axial Attitude Determination System (TRIAD) algorithm. The TRIAD algorithm utilizes two distinct attitude measurements and their corresponding inertial vectors to find the inertial-to-body DCM ($\boldsymbol{R}^{bi}$) [24]. The TRIAD algorithm treats one attitude measurement as the "truth" (most exact) measurement, which could cause discrepancies in the attitude solution if the other measurement is more representative of the truth (after all, the absolute truth is never really known). In addition, deterministic methods do not handle bias models, time-varying attitude parameters, or large quantities of data well. Deterministic methods are not based on statistical optimization, and the addition of multiple sensors is difficult to implement. Nonetheless, deterministic methods only require a rough a priori attitude estimate and are relatively easy to implement [49].

Statistical, or state estimation, attitude determination often provides a better attitude solution than deterministic attitude determination because it uses all measurement information available (as opposed to only two for the TRIAD algorithm). Statistical attitude determination does not treat one measurement as the "truth", but rather finds an optimal solution based off of a desired least-squares estimation technique (i.e. batch estimation, Kalman filters, sequential estimation, etc.). Although statistical attitude determination accounts for attitude parameters better than deterministic methods when uncertainty exists, statistical methods are often more computationally intensive and require a better knowledge of the a priori attitude [49].

One specific statistical attitude determination algorithm is the QUEST algorithm. Developed in 1981 by M.D. Shuster, the QUEST algorithm approximates an optimal

solution for the rotation matrix ($\boldsymbol{R}^{bi}$) using as many measurements as are available [39]. The batch estimation technique minimizes a form of Wahba's loss function J in Eq. 2.11 [24]. :

$$J = \sum_{k=1}^{N} w_k \left(1 - \boldsymbol{v}_{kb}^T \boldsymbol{R}^{bi} \boldsymbol{v}_{ki} \right) \tag{2.11}$$

where w_k is the measurement weight, $\boldsymbol{v}_{kb}$ is the measurement vector in the body frame, and $\boldsymbol{v}_{ki}$ is the inertial reference vector. Eq. 2.11 can be rearranged and put in terms of maximizing the scalar gain function g:

$$g = \sum_{k=1}^{N} w_k \boldsymbol{v}_{kb}^T \boldsymbol{R}^{bi} \boldsymbol{v}_{ki} \tag{2.12}$$

$$g = \lambda_{opt} \tag{2.13}$$

where λ_{opt} represents the optimal eigenvalue of the quaternion estimate, as shown in Eq. 2.14. The $\boldsymbol{K}$ matrix contains the eigenvector associated with the optimal eigenvalue.

$$\boldsymbol{K}\boldsymbol{q} = \lambda_{opt}\boldsymbol{q} \tag{2.14}$$

The $\boldsymbol{K}$ matrix in Eq. 2.14 is formed out of the vector measurements and measurement weights.

$$\boldsymbol{K} = \begin{bmatrix} \boldsymbol{S} - \sigma\boldsymbol{I} & \boldsymbol{Z} \\ \boldsymbol{Z}^T & \sigma \end{bmatrix} \tag{2.15}$$

$$\boldsymbol{B} = \sum_{k=1}^{N} w_k \left(\boldsymbol{v}_{kb}\boldsymbol{v}_{ki}^T \right) \tag{2.16}$$

$$\boldsymbol{S} = \boldsymbol{B} + \boldsymbol{B}^T \tag{2.17}$$

$$\boldsymbol{Z} = \begin{bmatrix} B_{23} - B_{32} & B_{31} - B_{13} & B_{12} - B_{21} \end{bmatrix}^T \tag{2.18}$$

$$\sigma = trace(\boldsymbol{B}) \tag{2.19}$$

Going back to the optimal eigenvalue, the QUEST algorithm assumes that a good approximation for λ_{opt} which maximizes the gain function (Eq. 2.13) is the sum of the N

18

measurement weights.

$$\lambda_{opt} \approx \sum_{k=1}^{N} w_k \tag{2.20}$$

By making this approximation, computationally expensive eigenvalue and eigenvector math does not have to be used. Instead, the quaternion can be solved for via Rodriguez parameters [24]. Rodriguez parameters (p) are another way to describe the attitude of a spacecraft and is defined in terms of quaternions and the Euler axis rotations in Eq. 2.21.

$$p = \frac{q}{q_4} = a \tan \frac{\Phi}{2} \tag{2.21}$$

where q, a, and Φ were previously defined in Section 2.1.2. When rearranged, the eigen problem becomes

$$p = \left[\left(\lambda_{opt} + \sigma \right) I - S \right]^{-1} Z \tag{2.22}$$

Although a matrix inverse is required to solve for the Rodriguez parameters, the computational expense for finding a matrix inverse is still much less than it is for finding an eigenvalue and eigenvector. Finally, the estimated quaternion vector is found in Eq. 2.23 using the Rodriguez parameters:

$$q = \frac{1}{\sqrt{1 + p^T p}} \begin{bmatrix} p \\ 1 \end{bmatrix} \tag{2.23}$$

2.1.4 Satellite Dynamics.

Satellite dynamics refer to the rigid body kinematic and kinetic equations which describe the motion of a spacecraft. The kinematic equation is a first-order time-differential equation that describes the orientation between the body and inertial frames [51]. Kinematic equations exist for all attitude representations (as described in Section 2.1.2), and the quaternion representation is defined in Eq. 2.24:

$$\dot{q} = \begin{bmatrix} \dot{q}_1 \\ \dot{q}_2 \\ \dot{q}_3 \\ \dot{q}_4 \end{bmatrix} = \frac{1}{2} \begin{bmatrix} q_4 & -q_3 & q_2 \\ q_3 & q_4 & -q_1 \\ -q_2 & q_1 & q_4 \\ -q_1 & -q_2 & -q_3 \end{bmatrix} \begin{bmatrix} \omega_1 \\ \omega_2 \\ \omega_3 \end{bmatrix} \tag{2.24}$$

where ω is the angular velocity of the spacecraft in the body frame with respect to the inertial frame about all three axes.

The kinetic equation, also referred to as Euler's Rotational Equation of Motion, describes the motion of a spacecraft about its center of mass. The torque experienced by the spacecraft is related to the change in angular momentum, as shown in Eq. 2.25.

$$M = \dot{H} \tag{2.25}$$

The angular momentum of a spacecraft is simply the moment of inertia matrix times the angular velocity of the spacecraft.

$$H = I\omega \tag{2.26}$$

The inertial time differential of Eq. 2.26 yields the general kinetic equation [51]:

$$M = I\dot{\omega} + \omega \times I\omega \tag{2.27}$$

This equation is used for ADCS modeling by isolating $\dot{\omega}$ and integrating to determine the expected angular velocity of the spacecraft. The external torques (M) include environmental disturbance torques and external actuator torques, such as magnetic torquers or thrusters.

2.1.5   *Magnetic Field Models.*

The use of magnetometers (body reference) for attitude determination requires an inertial reference of the magnetic field. Two primary magnetic field models exist - International Geomagnetic Reference Field (IGRF) and World Magnetic Model (WMM). The 11th Generation IGRF "is a series of mathematical models of the Earth's main field and its annual rate of change (secular variation)" [13]. The IGRF is voluntarily produced by magnetic field modelers and institutions associated with the International Association of Geomagnetism and Aeronomy. The IGRF is valid between 1900.0-2015.0 [12]. The IGRF is primarily used by the scientific community, whereas the WMM is primarily used by defense organizations. Produced by US and UK geospatial agencies, the WMM is "the

standard model used by the US Department of Defense, the UK Ministry of Defense, the North Atlantic Treaty Organization, and the International Hydrographic Organization" [14]. The WMM also measures the Earth's main field and its secular variations. However, it is a predictive model and is only valid for a few years at a time (currently 2010.0-2015.0) [12]. Although each model produces several components of the magnetic field given a certain date, latitude, longitude, and altitude, the only components used for an inertial magnetic field reference are the x-, y-, and z-components. These components are output in the local North-East-Down frame, respectively, as described in Section 2.1.1 [14].

2.2   Related Research

This section provides an overview of on-going ADCS research efforts at other universities and organizations. The section starts with a description of various satellite dynamic computer models used for ADCS analysis. After that, the section details two types of equipment employed for ADCS testing - a Helmholtz cage and an air bearing. The open-source information for all of these related research efforts is current as of December 2013.

2.2.1   ADCS Models.

A key component of successful ADCS design is an accurate spacecraft attitude computer model. An ADCS computer model describes the expected motion of the satellite when subject to disturbance torques, control algorithms, instrument noise, etc. ADCS computer models serve as the basis for integrating ADCS software with the hardware in addition to providing a validation reference for ADCS testing. Many university satellite programs have developed ADCS models. The following paragraphs briefly describe the ADCS models developed by the Naval Postgraduate School (NPS), Norwegian University of Science and Technology (NTNU), and Seoul National University (SNU).

2.2.1.1 NPS Satellite Model.

The Naval Postgraduate School developed a comprehensive ADCS model in support of their TINYSCOPE CubeSat mission [45]. The mission requires high accuracy attitude knowledge and utilizes an Extended Kalman Filter (EKF). The model, developed in 2009, runs in the MATLAB and Simulink environments. An overview of the Simulink model is shown in Figure 2.6. The model can utilize up to four sensors for attitude determination - a gyroscope, magnetometer, sun sensor, and star tracker - complete with noise characteristics to simulate actual hardware. In addition to the sensors and necessary spacecraft dynamics, the model takes into account environmental disturbance torques and orbit propagation. The model produced valuable results for the EKF's performance, but does not include attitude control algorithms [45].
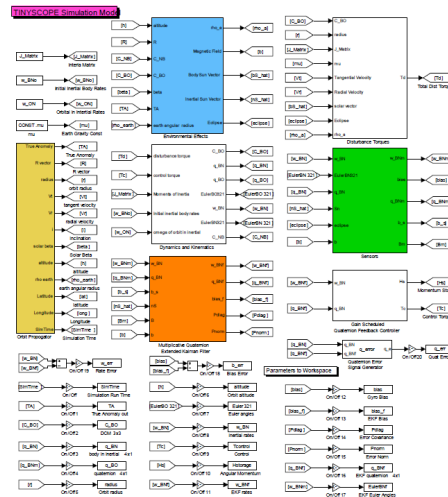
Figure 2.6: NPS TINYSCOPE Simulink Model Overview [45]

2.2.1.2 NTNU Satellite Model.

NTNU developed a MATLAB and Simulink model in support of their NTNU Test Satellite (NUTS) CubeSat mission [7]. NUTS is a 2U CubeSat scheduled to launch in 2014 into a sun-synchronous orbit. The NUTS mission involves analyzing Earth's gravity

through the use of an infrared camera pointing towards the Earth. Therefore, attitude control is necessary for NUTS to successfully complete its mission. The Simulink model, pictured in Figure 2.7, switches between two control algorithms - PD control and magnetic detumbling control - based off of the orbital angular velocity. In addition, the model uses an external magnetometer and IMU for attitude determination. Both control algorithms stabilized the spacecraft model, but were unable to correct the spacecraft's attitude with the addition of aerodynamic drag torques [7].
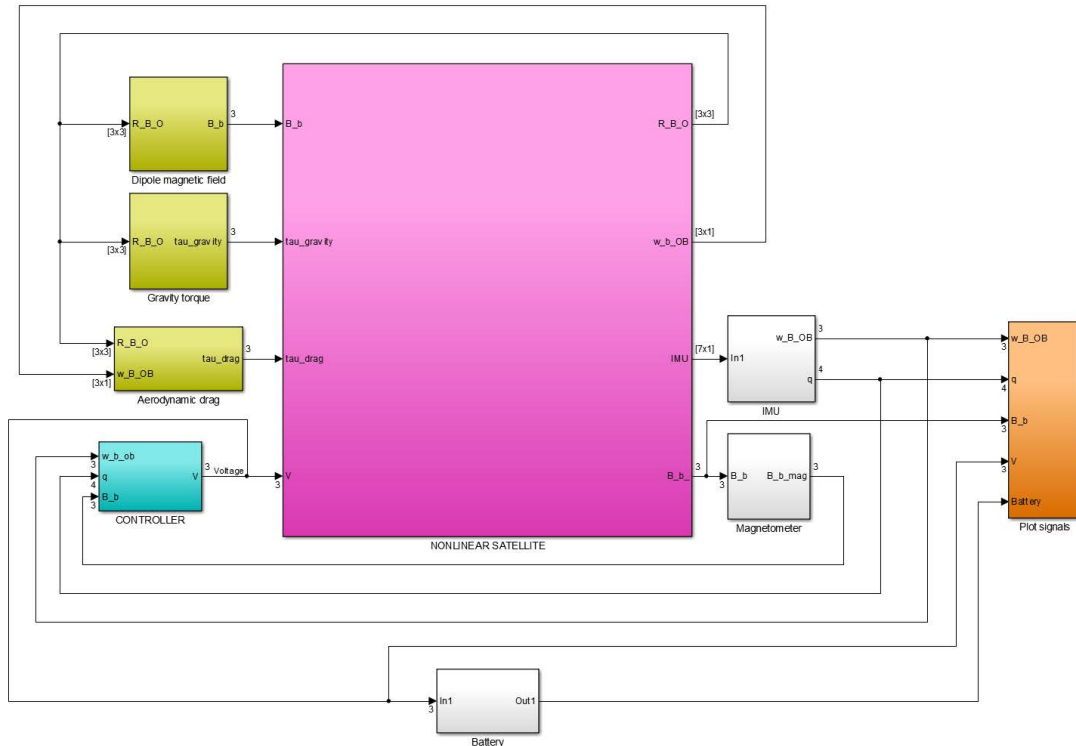
Figure 2.7: NUTS Satellite Simulink Model Overview [7]

2.2.1.3 SNU Satellite Model.

Lastly, students at SNU developed an ADCS satellite model with Fault Detection and Isolation (FDI) capabilities [31]. The Simulink model, as shown in Figure 2.8, uses the 6DoF ECEF Quaternion block from MathWork's Aerospace Toolbox, which incorporates

spacecraft dynamics in addition to other useful information such as DCMs, relative velocities, and external forces and moments. Thruster, GPS, and IMU blocks simulated the attitude control and determination, respectively. FDI capabilities included checking thruster packs for failures, implementing an outlier detection and elimination method, and detecting inertial sensor faults using the parity space approach. The model produced desired results for attitude control and FDI [31].
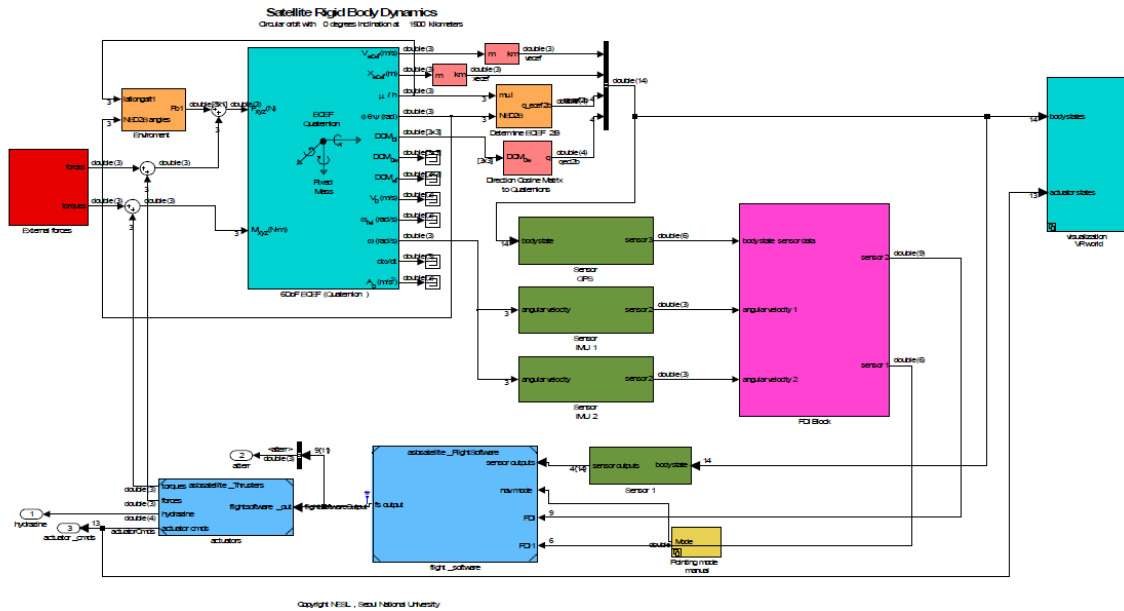
Figure 2.8: SNU ADCS with FDI Simulink Model Overview [31]

2.2.2 *Helmholtz Cages.*

A Helmholtz cage refers to three pairs of Helmholtz coils orthogonal to each other. A pair of Helmholtz coils, named after German scientist Hermann von Helmholtz in the 19th century, consists of conducting wire capable of producing a magnetic field, as shown in Figure 2.9. The magnetic field in the mid-plane between the two circular coils is found using the following equation:

$$B = \frac{32\pi NI}{5\sqrt{5}a} \text{ x } 10^{-7} \tag{2.28}$$

24

where B is the magnetic field, N is the number of wire turns, I is the current through the wire, and a is the radius of the coils and the distance between each coil. The space between the two coils (a) that yields the most uniform magnetic field occurs when the radius of the coils is equal to the distance between the coils ($d = a$ in Figure 2.9). If the coil spacing is too close or too far, then the magnetic field uniformity becomes either distorted or shortened, respectively [46].
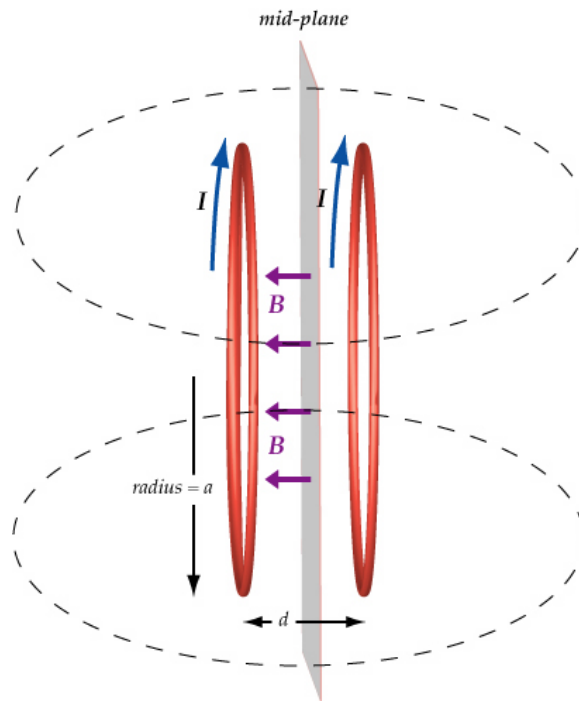
Figure 2.9: Magnetic Field Induced by Two Helmholtz Coils [46]

Oftentimes, three pairs of Helmholtz coils are constructed orthogonal to each other to form a "cage". The center of the cage provides a uniform magnetic field in all three directions (x, y, and z). A Helmholtz cage is particularly useful in space applications because it is capable of producing variations in the magnetic field as experienced by a satellite in orbit. The Helmholtz cage enables useful testing for satellites equipped with magnetic components, such as magnetometers and torque rods/coils.

The strength of the magnetic field produced from Helmholtz coils is determined from the users design. The user chooses the number of coil turns, the size of the coils, and the current supplied to the coils (of all of the parameters, the supplied current is the most limiting due to availability and expense of commercial power supplies). The majority of Helmholtz cages use square Helmholtz coils, as opposed to circular coils, due to the ease of manufacture and assembly. However, the ideal spacing between square coils is slightly larger than the spacing between circular coils. To optimize the uniformity of the magnetic field, the spacing between square coils needs to be 0.5445 times the length of the coil (as compared to 0.5 times the diameter of the circular coil) [20].

A number of universities have developed their own Helmholtz cages for CubeSat testing. These include, but are not limited to, the University of Michigan (U-M) and the Delft University of Technology (TU Delft). Their designs will be discussed in the following paragraphs. In addition, the commercially available Helmholtz cage from Macintyre Electronic Design Associates (MEDA), Inc. will be discussed. Other uniformly magnetic field cages exist, besides the Helmholtz cage, that use different design configurations of Helmholtz coils to enhance the size of the uniform field [27]. Those designs will not be discussed in this paper, but a recent implementation example is found at the Massachusetts Institute of Technology (MIT) [38].

2.2.2.1 U-M Helmholtz Cage.

In 2009, the University of Michigan built a 2 m *x* 2 m *x* 2 m Helmholtz cage to support their testing of the Radio Aurora Explorer (RAX) CubeSat (Figure 2.10a). RAX is a 3U CubeSat designed to "study the formation of magnetic field-aligned plasma irregularities (FAI) in the lower polar ionosphere (80-400 km altitudes)"[28]. Since the payload is magnetic-field related, extensive testing is necessary to ensure proper magnetic field readings on orbit. The Helmholtz cage structure is made out of aluminum T-slotted framing. Each coil consists of four parallel wires with 90 loops per wire, made out of 24

American Wire Gauge (AWG). Although no current literature has been published in regards to the full performance of the cage, U-M intends to produce ±2 Gauss in each axis with, along with mapping the magnetic field throughout the entire cage.
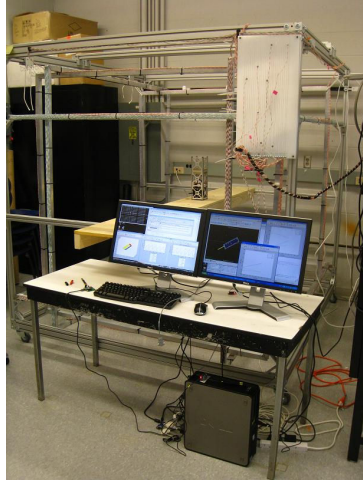
(a) University of Michigan [28]   (b) Delft University of Technology [36]
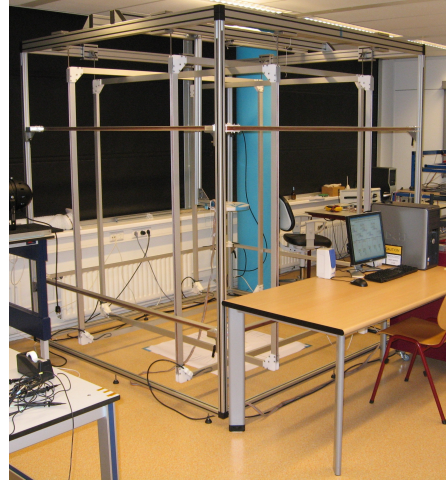
Figure 2.10: Existing Helmholtz Cages

U-M controls its Helmholtz cage through a MATLAB and STK interface. The interface control performs two primary functions - orbit simulation and automatic calibration. MATLAB receives inertial position and local vertical, local horizontal (LVLH) attitude states from STK. The magnetic field is then calculated in STK using the IGRF model. From there, the magnetic field strength is transformed into power supply voltages, which in turn produces the desired magnetic field in the Helmholtz cage. The auto-calibration function in MATLAB enhances the accuracy of the magnetometer data by identifying rotational discrepancies from the cage. Each power supply goes through a range of voltages while the other two power supplies are off. If any magnetic field changes are seen in the "off" power supplies, then a rotation is needed to account for the discrepancy (all axes should be orthogonal to each other). Each experiment runs the

auto-calibration code before collecting data; the entire process only takes about 2-3 minutes [28].

2.2.2.2 TU Delft Helmholtz Cage.

The Delft University of Technology built and tested a Helmholtz cage in 2006 to support their Delfi-C^3 CubeSat project (Figure 2.10b). The 3U Delfi-C^3's mission is to test two newly developed hardware components. The first component is the Thin Film Solar Cells (TFSC), which has a higher power to mass ratio than conventional solar cells and will be run on-orbit to characterize the component's current-voltage curve. The second component is the Autonomous Wireless Sun Sensor (AWSS), a digital sun sensor equipped with a small solar cell for power and wireless communication. To properly test the payloads on the ground, the Delfi-C^3 team required a gentle rotation of the satellite about all three axes. The satellite utilizes permanent magnets and hysteresis rods for passive attitude control (the magnets naturally align themselves with the magnetic field on orbit). A Helmholtz cage provides invaluable data about the characterization of the magnets and hysteresis rods and the behavior of the Delfi-C^3 satellite [36].

The Delft University Helmholtz cage's coil pairs are 2.05, 1.95, and 1.85 meters long in the x-, y-, and z-directions, respectively. The cage is designed to move the coil pairs within the cage structure to accommodate different types of testing. Coils spaced near the frame structure provide a larger test volume (up to 4 m^3), but sacrifice some field homogeneity. The closest spacing that still allows for a uniform field is 1 m^3. The cage is controlled via six power supplies commanded from a LabView interface. Each coil pair is capable of achieving up to 750 μT (7.5 G), although some variations within the cage exists due to magnetic field influence external to the cage (such as reinforced concrete in the building's structure) [36].

2.2.2.3 MEDA Helmholtz Cage.

In addition to the university-built Helmholtz cages, there is a commercial Helmholtz cage available for purchase from MEDA, Inc (Figure 2.11). The company specializes in the manufacture of precision magnetometers and magnetic field sources. As of 2005, they can build cages that are either 1, 2, or 4 meters in length. Unlike U-M and TU Delft, the coil structure stands on its own and does not require a supporting aluminum structure frame. The consumer can choose a closed-loop or open-loop system architecture. The closed-loop architecture uses an external magnetometer and power supplies to automatically null the magnetic field within the cage, whereas the open-loop architecture uses fixed currents to more coarsely null the magnetic field. The 2 m-long cage produces a magnetic field strength of up to $\pm 200,000$ nT (± 2 G). MEDA intends for their cages to be used for biological research, but their cages can easily be outfitted for space research [32].

Figure 2.11: MEDA, Inc. Helmholtz Cage [32]

2.2.3   Air Bearings.

ADCS hardware is difficult to test due to the environment on Earth's surface. This difficulty can be mitigated through the use of an air bearing. An air bearing provides a near frictionless surface, which allows for high fidelity testing. CubeSats are more prone to movement from environmental disturbance torques than larger satellites because of the smaller satellite moment of inertia. The fidelity of an air bearing shows the potential effects of minute disturbance torques on a CubeSat, which is informational in regards to a CubeSat's attitude determination and control performance.

Air bearings are "pneumatic devices which form a lubricating film of air between the load and floor surface." [3]. Conceptually, an air bearing follows Newton's Second and Third Laws (where force p̄ressure x area). The pressure exerted by the layer of air over the surface area of the load counteracts the force of gravity so that the load "floats" and is free to move. An air hockey table is a common example of a planar air bearing. Air bearings do not have to deal with heat-induced friction, unlike ball bearings. In addition, air is clean and contaminant free. By nature of the need for an extremely small gap between the load and floor surface in order to operate an air bearing properly ($10 \ \mu m$), air bearings provide highly accurate use. Coupled with the extremely small gap is the need to have near flawless geometry on the load surface. The smallest imperfection, such as a scratch, uneven holes, lack of straightness, etc., will result in degraded performance and accuracy [1].

Although many air bearing configurations exist, the most applicable air bearing configuration for this research is a spherical air bearing. As seen in Figure 2.12, a hemispherical air bearing provides full rotational motion about one axis and limited rotational motion about the other two axes (limited by the floor surface). Spherical air bearings do not accommodate linear motion. However, the majority of CubeSat satellite research and development will not require translational testing (an exception might be

30

formation flying). Primary testing includes slewing the spacecraft to a desired inertial vector, demonstrating spacecraft de-tumbling, and characterizing spacecraft movement based off of small disturbance torques.
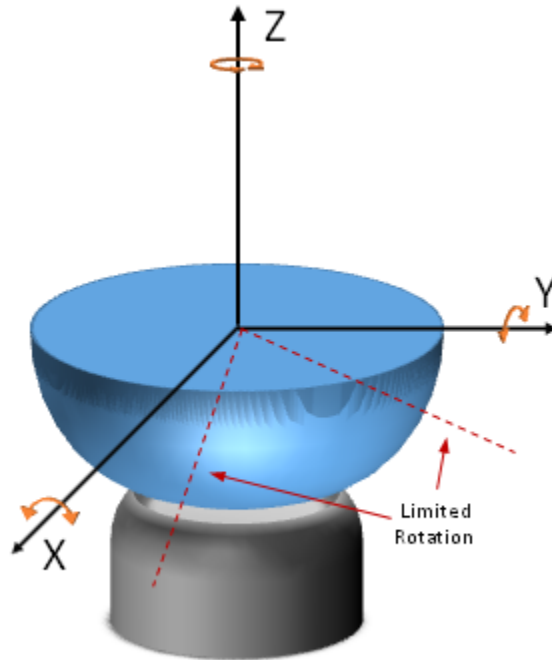
Figure 2.12: Spherical Air Bearing with 3 Rotational Degrees of Freedom

The most difficult challenge of testing hardware on a spherical air bearing is balancing the load surface. The load surface for a spherical air bearing is typically a flat tabletop with ADCS components mounted on top. Due to their accuracy and low-friction environment, air bearings are subject to minute, yet noticeable dynamic and static disturbance torques (10^{-4} N-m). Environmental disturbance torques, such as air ventilation, magnetic fields, and radiation pressure, affect the motion of the air bearing. In addition, component wiring, flexible structures, and structure deformation can create undesired torques during testing [26]. These dynamic disturbance torques are extremely

difficult to model and often require an automatic mass balancing system to achieve the desired air bearing accuracy. Manual mass balancing attempts to minimize static gravitational disturbance torques caused by the misalignment of the load surface's center of gravity and the air bearing's center of rotation. The goal of accurate balancing is to create as close to a torque-free environment as possible. The air bearing and load surface system is similar to a pendulum. The fulcrum of the pendulum is the air bearing's center of rotation, and the weight at the end of the pendulum is the center of gravity of the load surface. If the center of gravity is above the center of rotation, then the system is unstable. If the center of gravity is below the center of rotation, then static stable pendulum motion will exist based off of the distance between the center of rotation and the center of gravity. The system is dynamically stable if the center of gravity is coincident with the center of rotation. A dynamically stable system eliminates pendulum motion so that the load surface stays in any orientation as desired.

There exists a number of air bearings at universities and other research institutions. The following paragraphs will explore three air bearing systems in particular at the National Autonomous University of Mexico (UNAM), MIT, and York University, respectively. All of these air bearings provide invaluable hardware-in-the-loop testing.

2.2.3.1   UNAM Air Bearing.

In 2005, UNAM built and tested a spacecraft simulator designed to "carry out tests of sensors, actuators, and algorithms in the experimental framework" [37]. The simulator, Figure 2.13, consists of a tabletop surface mounted on top of a spherical air bearing (together making the load surface). The tabletop houses sensors, actuators, a bi-directional radio link, a balancing system, and an on-board computer. UNAM custom-built the air bearing hemisphere and cup through which the air flows. The 99.93 mm diameter hemisphere is made out of phosphor bronze and can hold up to 80 kg. The sensors mounted to the tabletop include an IMU, a three-axis magnetometer, Sun sensors, and

Earth sensors. The actuators include reaction/momentum wheels (depending on the desired operation of the wheels) and magnetic coils, with one of each on the x-, y-, and z-axes. The bronze wheels have a maximum speed limit around 4,200 RPM with a nominal momentum wheel speed between 1,400 and 2,200 RPM. The magnetic coils are long torque rods with a ferromagnetic core that yield a nominal 12 A-m^2 magnetic moment. The bi-directional radio link enables attitude telemetry to be passed wirelessly to the ground station computer. The on-board computer handles all attitude determination and control algorithms and controls the components mounted to the tabletop. The computer has a 16-bit RISC microcontroller with 64 KB of ROM and 1.28 MB of SRAM. Basic control algorithms were tested on the spacecraft simulator showing that the reaction wheels and magnetic coils work as desired [37].

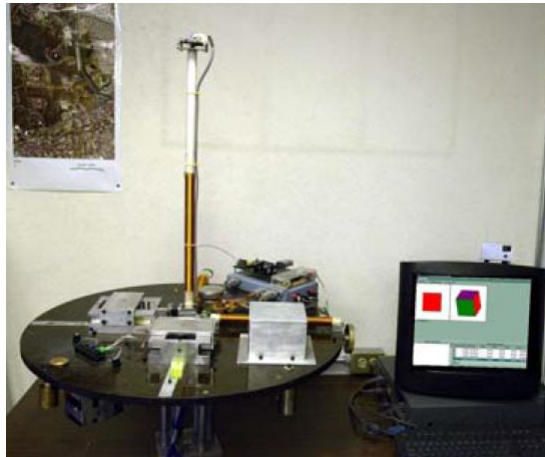Figure 2.13: UNAM Spacecraft Simulator with Automatic Mass-Balancing System [37]

UNAM designed and implemented two automatic mass-balancing systems for the air bearing. Both systems use sliding masses to achieve the desired balanced position. A stepper motor moves the 0.615 kg mass along a threaded rod at 0.005 mm increments, with a maximum displacement of 5 cm. Special care was taken to mount the tabletop's

33

components as symmetrically as possible in order to achieve an acceptable level of manual balancing. The first automatic mass-balancing system dynamically estimates the load surface's moment of inertia (MOI) and center of mass using angular velocity and acceleration sensors. The on-board computer solves a set of Euler's equations for a rigid body. The computer continually commands three sliding masses (one on each axis) until the threshold limit between the center of mass and center of rotation is reached (0.025 mm). The second automatic mass-balancing system aims to perfectly position the load surface horizontally (static equilibrium). Two horizontal sliding masses (x- and y-axes) are controlled based off of feedback using two inclinometers (as part of the three-axis magnetometer) until the threshold limit is reached (±0.25 arc deg). The first balancing technique produces a final residual torque of 0.0049 N-m (50 gr-cm), whereas the second balancing technique produces 0.002 N-m (20 gr-cm) of residual torque. The first balancing technique is more computationally expensive and adds mass to the system (three sliding masses instead of two). Therefore, the desired automatic mass-balancing system is statically balancing the load surface so that it is as horizontal as possible [37].

2.2.3.2   *MIT Air Bearing.*

MIT student Corey Crowell developed and tested a spherical air bearing testbed and ADCS MATLAB simulation in 2011 [18]. The air bearing is designed to test ADCS components for small satellites, which includes satellites up to 180 kg (ESPA-class). Similar to UNAM's spacecraft simulator, the MIT simulator mounts individual ADCS components on the testbed, as shown in Figure 2.14. An IMU and a three-axis magnetometer comprise the attitude sensors. Reaction wheels are the only actuators used for attitude control. There are four reaction wheels mounted on the testbed, with each motor capable of producing 0.295 N-m of torque. As seen in Figure 2.14b, three wheels are mounted orthogonal to each other at an off angle from the horizontal tabletop, and one wheel is mounted in the middle of the tabletop to provide redundancy. The reaction

wheels are larger than usual for a small satellite, but are necessary given the larger disturbance torques experienced by the air bearing. The testbed does not have an automatic mass-balancing system, but has multiple means of adjusting the mass manually. The battery packs (blue rectangular boxes in Figure 2.14b can be moved up and down along the threaded rod. In addition, six small trim masses located on the support structure above the center reaction wheel finely adjust the center of mass [18].
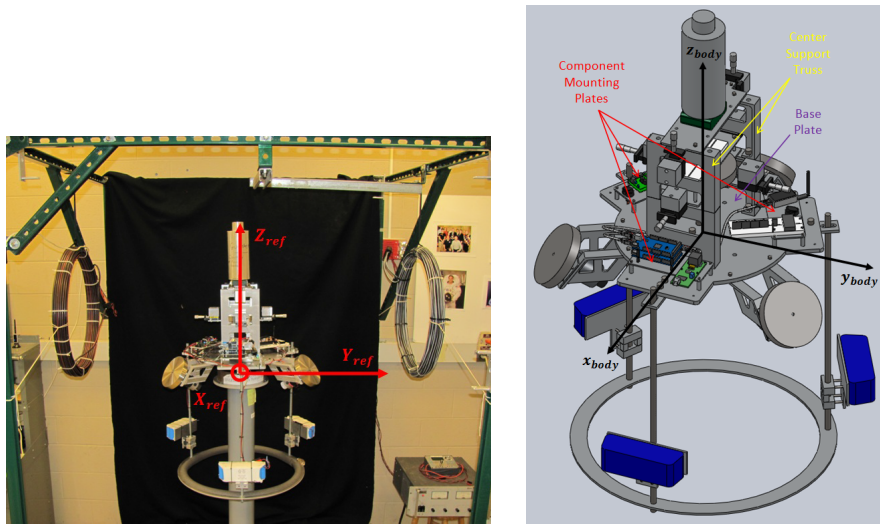
(a) Air Bearing Assembly with Surrounding Magnetic Coils

(b) Air Bearing Solidworks Model

Figure 2.14: MIT Spherical Air Bearing [18]

The MATLAB Simulink simulation models the behavior of the testbed in the air bearing (near frictionless "space") environment. The simulation accommodates changes to the testbed configuration in terms of both hardware and software. This proves useful because the simulation can determine whether or not it is safe/feasible to physically make the desired changes to the testbed. The Simulink model estimates the position and angular rates of the testbed along with commanding the reaction wheels to respond according to

35

the chosen control scheme. The model provides a point of comparison between simulated and actual data.

Crowell validated the testbed by running a series of component characterization tests and air bearing integrations tests. The tests characterized each component in terms of noise levels, biases, torque capabilities, etc. Other tests measured the disturbance torques acting on the load surface, including the effect of manual mass balancing and multiple configuration testing to create a baseline for expected external disturbance torques. Lastly, an integration test was performed to simulate the anticipated behavior of one of MIT's continuing research efforts - the MicroMAS 3U CubeSat. As shown in Figure 2.14a, coils surrounding the air bearing create a magnetic field in one direction [18]. Since the completion of the air bearing, students at MIT have built a Merritt 4-coil cage (similar to a Helmholtz cage) around the air bearing to produce a magnetic fields in all three directions [38].

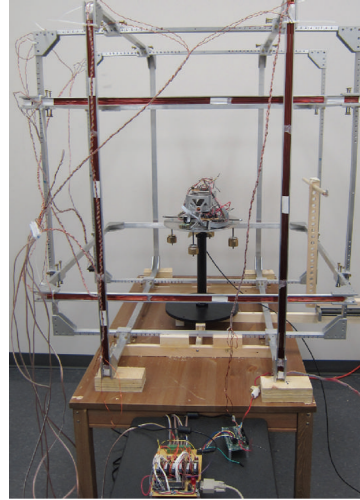### *2.2.3.3 York University Air Bearing.*

York University tested custom-built actuators on an air bearing assembly in 2013. The actuators, which all fit within 1U, include three reaction wheels and three torque rods. The 0.214 kg reaction wheels are controlled by Faulhaber brushless flat micromotors, capable of producing 6.0×10^{-4} N-m of torque. The torque rods fit within the walls of a 1U stack and have a maximum magnetic moment of 0.37 A-m^2. As shown in Figure 2.15a, the tabletop load surface holds the 1U stack with the actuators, a manual balancing system, on-board computer, wireless transceiver, reference IMU, power distribution board, and batteries [30]. The manual balancing system caused some undesired gravitational torques evident in the test data. Nonetheless, two software algorithms were successfully tested on the air bearing using the in-house actuators. Currently, York University is completing integration of the air bearing assembly in the Helmholtz cage (Figure 2.15b) in order to fully develop their ADCS CubeSat testing [30].
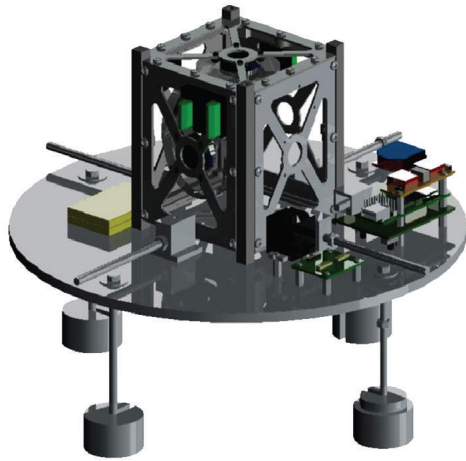
(a) Air Bearing Model for
1U CubeSat Testing

(b) Air Bearing Assembly in
Helmholtz Cage

Figure 2.15: York University Spherical Air Bearing [30]

2.3 AFIT 6U CubeSat

AFIT's 6U CubeSat chassis is a robust, modular design. As mentioned in the previous chapter, each unit within the chassis is precisely measured to fit a "stack" in 24 different configurations. An example of a stack and some of its different configurations is shown in Figure 2.16. In order to strengthen the structural integrity of the chassis, support braces can be mounted at all cross sections inside the chassis in a number of configurations. This proves useful when trying to thermally isolate some sections of the CubeSat from other sections in addition to magnetically isolating some components from others (such as the external magnetometer from the IMU). The 6U chassis yields to the constraints of the Planetary Systems Corporation Canisterized Satellite Dispenser (PSC-CSD), which is a CubeSat dispenser for secondary payloads. Although the 6U PSC-CSD has not been flight proven, the 3U PSC-CSD successfully deployed the POPACS payload on-board a Falcon 9 in September 2013 [17, 47].
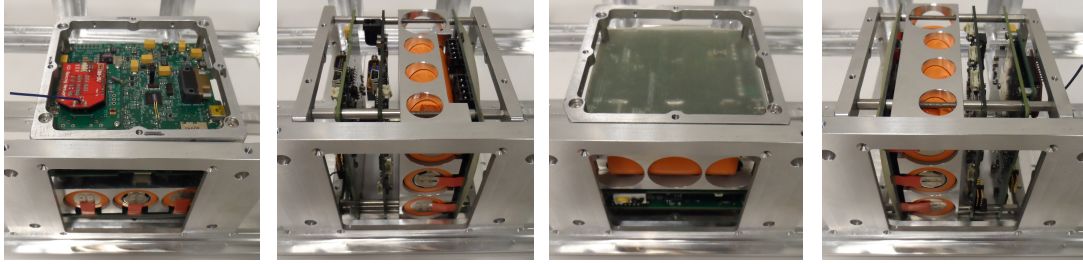
Figure 2.16: Four Stack Orientations

2.4 Chapter Summary

Chapter II covered ADCS background information and related research projects. The chapter defined five coordinate frames - ECI, ECEF, NED, orbital (RPY), and body frames. Next, the mathematics behind coordinate transformations and Direction Cosine Matrices were described along with an illustration of several attitude representations. The three discussed attitude representations - Euler angles, Euler axis, and quaternions - were summarized in Table 2.1. The chapter continued with a step through of the QUEST attitude determination algorithm. The QUEST algorithm attempts to minimize Wahba's loss function and makes an important approximation which eliminates the need for solving an eigenvector/eigenvalue problem in computer code. The chapter then briefly discussed satellite kinematics and kinetics, which describe the motion of the satellite with respect to an inertial frame. The background section concluded with a comparison of two magnetic field models. The magnetic field models are necessary for providing an inertial reference model when using magnetometers for attitude determination.

The second part of the chapter included a state-of-the-art description of ADCS research efforts. Three MATLAB/Simulink models from NPS, NTNU, and SNU were briefly reviewed. The models lend themselves as useful analysis tools to verify the expected motion of a spacecraft given its ADCS components and control algorithms. Next, the chapter detailed two ADCS test equipments - a Helmholtz cage and a spherical

air bearing. The Helmholtz cage produces a uniform magnetic field, which can be manipulated to simulate the magnetic field as experienced on orbit. The U-M, TU Delft, and MEDA, Inc. Helmholtz cages yielded about ±2 Gauss in each axis. From there, the chapter outlined three spherical air bearings from UNAM, MIT, and York University. Air bearings provide a near frictionless environment with one full rotational degree of freedom and two partial rotational degrees of freedom. The chapter finished with an overview of AFIT's 6U CubeSat chassis and stack configurations. The specific components and testing of AFIT's 6U ADCS will be discussed in the following chapters.

III. ADCS Development and Test Methodology

The following chapter describes the work completed throughout this research effort. In particular, the first part of the chapter details the hardware and software development of AFIT's current ADCS components. This also includes a description of the Simulink model used to verify experimental results. After the component design section, the chapter focuses on the design of the spherical air bearing that is used inside the Helmholtz cage. The latter part of the chapter outlines the experiments for testing ADCS components and the integrated satellite.

The design and development work completed in this research was a team effort led by the author. In addition to the work completed by students in previous years, current students 2Lt Evelyn Abbate and 2Lt Warren Grunwald contributed to ADCS development during ASYS 632 in Summer 2013. Also during that summer, various interns developed CDH and EPS hardware and software along with the MATLAB ground station. Philip Smith and the AFIT machine shop supplied necessary mechanical help, such as CAD drawings and parts manufacturing. Matthew Lippert provided the primary software development for the ADCS. Without the contributions of these individuals, the final product of this thesis would not be possible.

3.1 ADCS Starting Point

As mentioned in Chapter I, each AFIT class of students who takes the space vehicle design sequence build upon the work done in the previous year. The level of design established by AFIT's 2012 space vehicle design class is described in order to give context to this thesis research.

The most significant hardware ADCS contribution from the 2012 space vehicle design class is the design and development of a four-wheel Reaction Wheel Assembly (RWA), as shown in Figure 3.1.
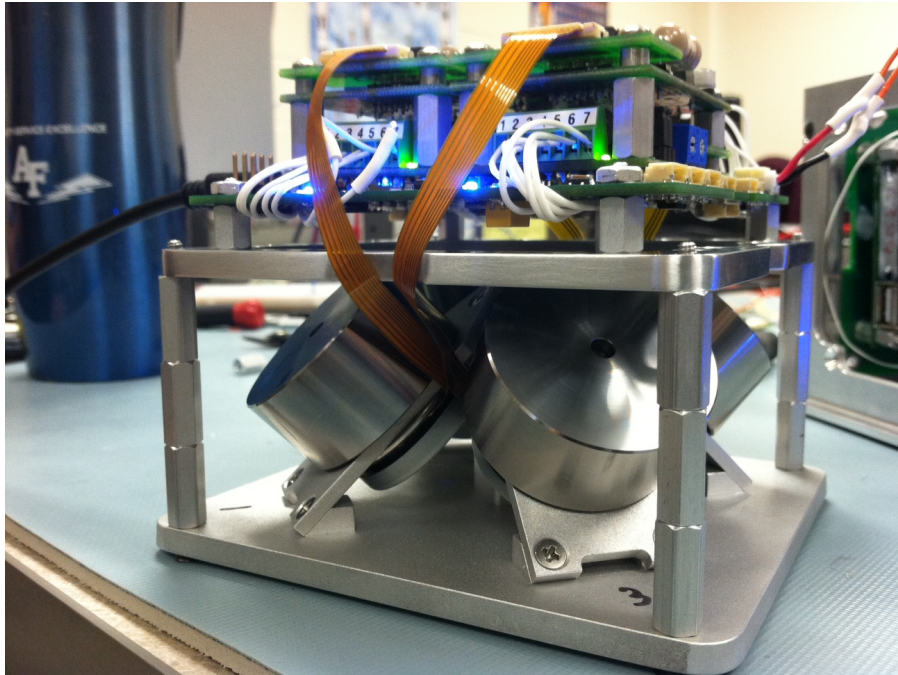
Figure 3.1: 2012 Reaction Wheel Assembly

The class performed detailed analysis on the desired position and sizing of the reaction wheels. The desired position of the reaction wheels in terms of assembly and performance was determined to be 45° from both the horizontal and vertical planes. Each reaction wheel has a MOI of approximately 2.6 x10^{-5} kg-m^2. Four EC 32 flat Maxon motors drive the reaction wheels (Part 339259), and a pair of motors was controlled by a Digital EC Controller (Maxon 249630). The software ramped the reaction wheels up and down by varying motor input voltages from digital to analog converters, but no control was demonstrated by the end of the course. In addition, the motors became dysfunctional after vibration testing with the integrated spacecraft. Therefore, the design could only be used

for on-the-ground testing, but requires significant structural changes to eventually survive the launch environment (which is currently in progress by another group of students).

In regards to sensor development, the 2012 class built and tested sun sensors and a magnetometer, as shown in Figure 3.2. Six sun sensors were used on each face of a 6U CubeSat (SparkFun TEMT 6000 with Vishay Ambient Light Sensor). The sun sensor mounts were custom-built to fit on the inside of the CubeSat facing outwards. Calibration and testing yielded an accuracy of about 1.2° for all six sensors. The magnetometer used for the 2012 6U CubeSat was part of a 9 degrees of freedom (DOF) IMU consisting of a 3-axis accelerometer, magnetometer, and gyroscope (SparkFun 9DOF Sensor Stick 10321). Out of the three available sensors on the IMU, only the magnetometer was used for attitude determination. The SparkFun 9DOF IMU was mounted to the ADCS circuit board. After calibration and testing, the magnetometer yielded an accuracy of about 5.0°, which is outside of the specification-claimed 1-2° accuracy.
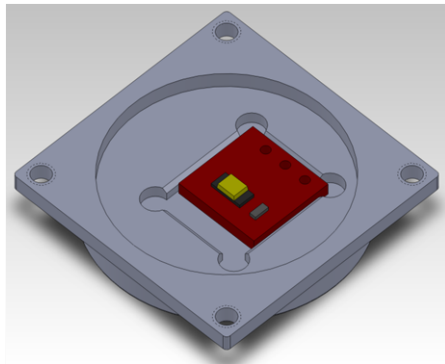
(a) SparkFun Light Sensor and Mount [15]   (b) SparkFun Inertial Measurement Unit [15]

Figure 3.2: 2012 Attitude Determination Sensors

Preliminary designs existed for a star tracker and torque coils. However, due to time constraints, the designs did not make it past the drawing board. Overall, the ADCS components and software successfully determined the spacecraft's attitude, but could not control the spacecraft by the end of the 10-week course.

A few months prior to the 2012 students' CubeSat development course, an AFIT Master's graduate completed the building and testing of AFIT's Helmholtz cage [9]. The cage, Figure 3.3, consists of three square orthogonal nylon coils measuring 92", 89", and 86" from outer edge to outer edge in the y-, z-, and x-frames, respectively. Three power supplies capable of 0-60 V and 0-10 A at 200 W produce a current through each coil. The specific power levels are commanded through a Systems Tool Kit (STK) (with the Space Environment and Effects Tool (SEET) package) and Matrix Laboratory (MATLAB) interface in order to simulate the magnetic field expected on orbit. In addition, the coils are connected to relay switches to readily switch the direction of the magnetic field as desired. Each coil pair is capable of producing ±2 Gauss, as determined by a high-fidelity ("truth") magnetometer placed in the center of the cage [9].

The Helmholtz cage was relocated before this research effort due to facility changes. The uniformity of the cage has not been retested. However, it is assumed that the desired uniformity exists, possibly better than it was before, because previously the cage was influenced by the reinforced support beam that caused y-axis discrepancies [9]. In addition, the MATLAB and STK software were updated for software version compatibility.

At the start of this research, AFIT purchased a second spherical air bearing and pedestal specifically for 6U CubeSat ADCS testing (AFIT also owns a larger spherical air bearing used on a larger satellite simulator called SimSat, but it is not directly related to this research effort). No previous work had been accomplished in regards to developing the air bearing's operational capabilities.
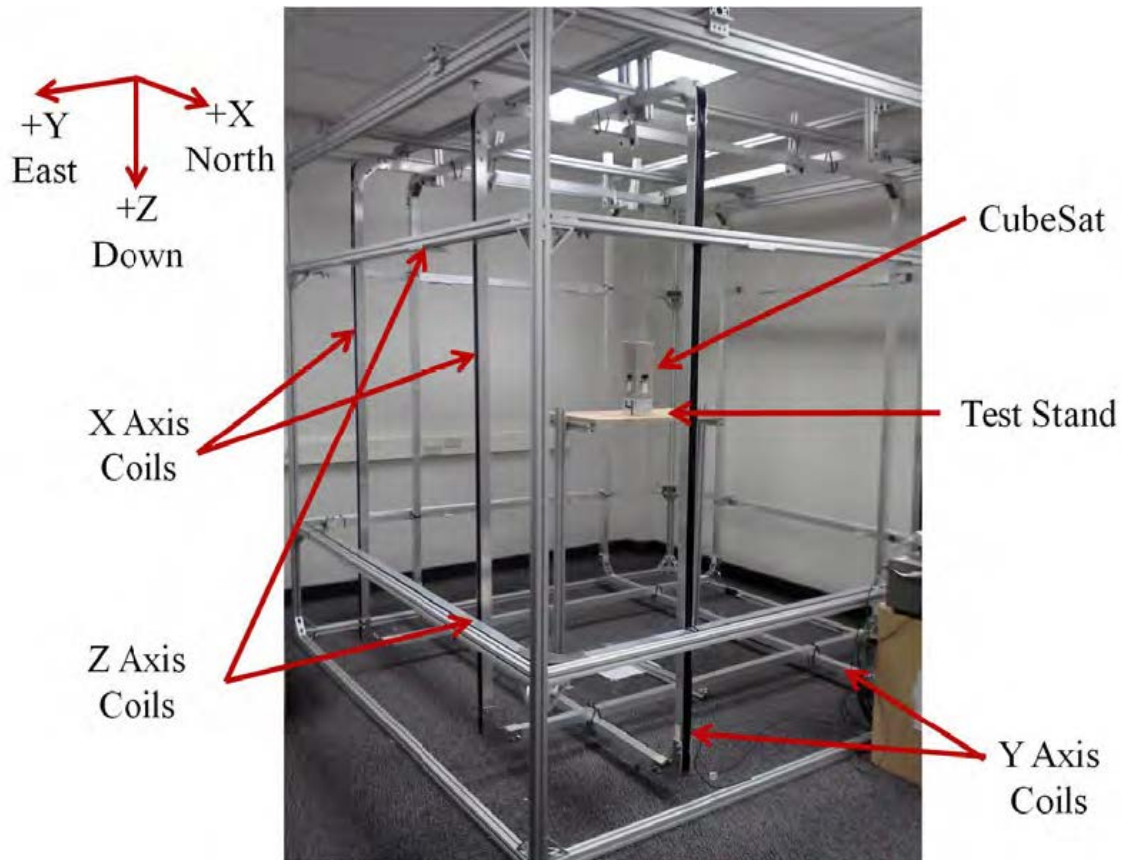
Figure 3.3: AFIT Helmholtz Cage [9]

3.2 ADCS Component Design

The following section describes the specific hardware designs of AFIT's ADCS sensors and actuators. The components include Sun sensors, Earth sensors, an IMU, an external magnetometer, torque coils, and a 4-wheel reaction wheel array. The components are either commercially purchased or custom built.

3.2.1 Sensors.

Sun sensors, Earth sensors, an IMU, and an external magnetometer comprises the sensor suite for AFIT's ADCS. Although some COTS packages also include a star tracker, the complexity and cost deem it unnecessary as part of the standard sensor suite.

Nevertheless, a star tracker can always be added later in the design process (especially for a 6U CubeSat since there will probably be sufficient volume).

For this research, the IMU and external magnetometer were the only working attitude sensors. The additional Sun and Earth sensors are briefly discussed to illustrate how they are designed and how they will be incorporated in the future.

3.2.1.1 Sun Sensors.

Nearly all spacecraft use Sun sensors because of their simplicity and requirement to obtain power from the Sun. Sun sensors are relatively simple devices that detect either visible light or infrared. They are the most logical device used to point the solar panels on a spacecraft towards the Sun for solar power. Nonetheless, Sun sensor information is limited due to a spacecraft flying in and out of eclipse. Typical Sun sensors have an accuracy of 0.005-3 degrees and have low mass (0.1-2 kg) and low power consumption (0-3 W) [50].

AFIT's ADCS uses the Advanced Photonix, Inc. (API) Red Enhanced Quad Cell Silicon Photodiode (SD 085-23-21-021) (Figure 3.4a). The quad cell design is necessary to provide a unit Sun vector. Attitude control algorithms use the calculated Sun vector as a reference to point the spacecraft as desired. For a detailed description on how to calculate the unit Sun vector based off of outputs from the quad cell photodiode, see Hall's text on attitude determination [24]. The Sun sensors are designed to mount to a 1U plate on the inside of the CubeSat chassis pointing outwards, as shown in Figure 3.4b. The thin plate does not interfere with any 1U stacks. The API photodiode has an 86° viewing angle, but the baffle around the photodiode shrinks the viewing angle to 60° [5]. A 60° viewing angle gives the desired field of view for accurate Sun sensor measurements. In addition, an aperture plate is mounted on top of the photodiode to focus the light at the desired field of view [4].

(a) Sun Sensor Photo Diode [16]

(b) Sun Sensor Mount
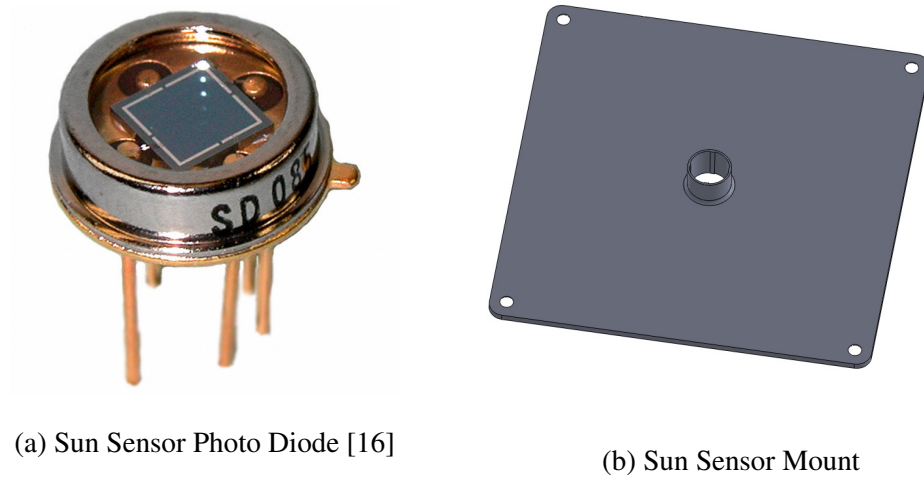
Figure 3.4: Sun Sensor Design

3.2.1.2 Earth Sensors.

Earth sensors are infrared (IR) sensors that detect the difference between the cold of space and Earth's atmospheric temperatures. Earth sensors are particularly useful for Earth-observing spacecraft because the sensor measurements can simplify on-board processing [50]. AFIT's ADCS uses five Melexis Infrared Thermometers (MLX90615), Figure 3.5a, in an array. The array design, as shown in Figure 3.5b, provides means for pointing the spacecraft in the nadir direction. Modeled after the PSSCT-2 CubeSat's Earth sensor array from the Aerospace Corporation, the center IR sensor is used to see the full Earth, while the surrounding four, canted sensors are used to detect the temperature difference between Earth and space [4],[25]. The Earth sensor array mounts to the outside wall of a 1U space.

3.2.1.3 IMU.

An IMU at a minimum consists of gyroscopes and accelerometers, but usually also includes magnetometers. As the name implies, the sensors in the IMU take the inertial measurements about the sensor unit. Gyroscopes (colloquially referred as gyros) provide
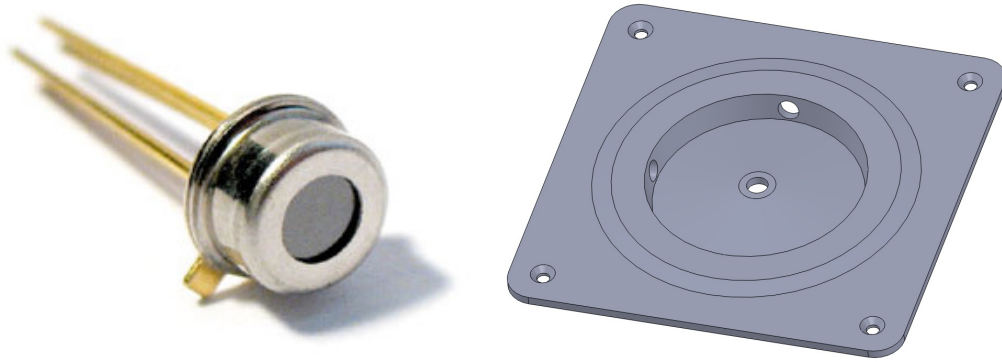
(a) Melexis IR Sensor [33]   (b) Earth Sensor Array

Figure 3.5: Earth Sensor Design

angular velocity measurements, which is especially useful for attitude control purposes. Gyroscopes can also be augmented for high precision attitude determination by filling in the gaps between sensor measurements. In addition to common sensor bias, gyroscopes also experience bias drift, which is "an additional, false rate the sensor effectively adds to all rate measurements"[50]. The drift bias could cause attitude control issues over the lifetime of a spacecraft, depending on the mission requirements and sensitivity of the IMU. However, drift bias measurements can be calculated and removed by using an external reference such as a star tracker [10]. Accelerometers measure the acceleration along a given axis. When stationary, accelerometers output the direction and magnitude of Earth's gravity vector. Magnetometers provide magnetic field measurements. Magnetometers are especially useful for attitude determination at low altitude orbits because the magnetic field of the Earth is greater than at higher altitude orbits.

AFIT's ADCS uses the Analog Devices High Precision Tri-Axis IMU. The ADIS16405 model provides a range of ±75°/sec for the gyroscopes, ±18g's for the accelerometers, and ±2.5 Gauss for the magnetometers. The device is set up for either manual or automatic gyroscope calibration, if desired. The device also includes a

temperature sensor and auxiliary Digital-to-Analog Converter (DAC). The Microelectromechanical System (MEMS) device measures 23 mm x 23 mm x 23 mm with a small connector device and is shown in Figure 3.6 [19].

Figure 3.6: ADIS1604 Three-Axis IMU

3.2.1.4 External Magnetometer.

In addition to the IMU magnetometer, the AFIT ADCS sensor suite includes an external magnetometer. The disadvantage of using a magnetometer in a CubeSat is its proximity to other components. The magnetic field created by torque coils render magnetometer readings useless. The motor operation of the reaction wheels also produce a magnetic field that could undesirably alter magnetometer readings. Even the electromagnetic field produced from the integration of all CubeSat components yield a magnetic field change. Currently, the IMU is placed directly above the reaction wheel array. An external magnetometer, located as far away from the reaction wheels as possible, may not be as susceptible to changes in the magnetic field and could provide a better attitude estimate during reaction wheel operation. The external magnetometer implemented for testing is the same magnetometer used in the previous year group's work - the SparkFun 9DOF IMU (as described in Section 3.1). Only the magnetometer functionality of the IMU will be used.

3.2.2 Actuators.

AFIT's ADCS actuators consist of custom built torque coils and reaction wheels. The general theory and design for each type of actuator is described below.

3.2.2.1 Torque Coils.

Magnetic torquers, also referred to as magnetorquers, serve as actuation devices on board the spacecraft. Three orthogonal magnetorquers can be used for three-axis spacecraft control. A magnetorquer interacts with the Earth's magnetic field experienced in orbit (B) by producing a magnetic dipole moment (M)[50]. The magnetic dipole moment produces an external torque (T) on the spacecraft when not aligned with the changing magnetic field in the orbit, as shown in Eq. 3.1.

$$T = M \times B \tag{3.1}$$

Since the torque is externally applied to the spacecraft (similar to thrusters), magnetorquers are commonly used to desaturate momentum exchange devices (such as reaction wheels). This desaturation, commonly referred to as "momentum dump", is vital to nearly every 3-axis stabilized spacecraft.

The two most common forms of magnetorquers are a torque rod and a torque coil. Torque rods are generally made out of a conducting wire (such as copper) wound tightly around a cylindrical ferromagnetic core, as shown in Figure 3.7a. In addition to their compactness, torque rods consume little power [49]. Torque rods can come in a variety of sizes. CubeSat-sized torque rods are commercially available, but can be undesirably expensive. The CubeTorquer, which is capable of producing a $0.2\ A-m^2$ magnetic dipole, is approximately $\$1,000$ US dollars [2].

The primary disadvantage of torque rods is their residual magnetic field, which causes nonlinearity and hysteresis [49]. Torque coils follow the same concept as torque rods, but are "wrapped" around air, causing the magnetic field lines to collapse almost

(a) Torque Rod Example [2]   (b) AFIT's Torque Coil
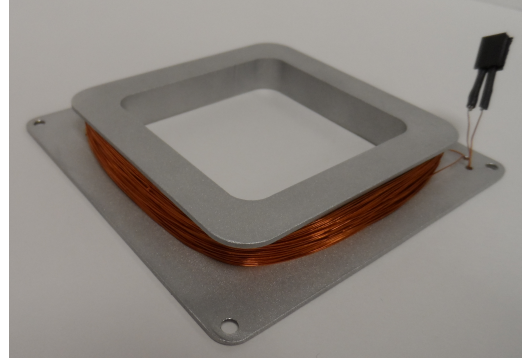
Figure 3.7: Types of Magnetic Torquers

instantaneously. With similar use of conductive wires, torque coils are wrapped around a

specific structure, such as a square or hexagon. Torque coils have two primary mechanical

advantages over torque rods. Torque coils can conform to any structure as desired,

whereas torque rods are more rigid and less modular. In addition, most torque coils are

custom built, which in the end is less expensive than a commercially built torque rod.

However, torque coils are typically less capable than torque rods in terms of available

magnetic dipole moment. Torque coils produce a magnetic dipole moment governed by

the equation of a solenoid in Eq. 3.2 [49].

$$M = nIA \qquad (3.2)$$

where n is the number of turns of the wire, I is the current going through the wire, and A is

the cross-sectional area of the coil. Torque coils can be placed in all three principal axes to

create the magnetic moment vector described in Eq. 3.1.

   The driving design consideration for AFIT's torque coils was the location of each

coil. The final design, Figure 3.7b, utilizes the wall space of the 6U side plates so that the

torque coil does not interfere with the adjacent 1U stack. The side-mounted torque coils

do not interfere with any stacks, but the bottom-mounted torque coil is limited in its

acceptable location depending on the design of the stacks. The three torque coils can be mounted in any available location, as long as they are mounted orthogonal to each other. Each coil consists of 400 turns of coated 30 AWG copper wire. The average area of the torque coil mount is 0.0036 m^2 and 500 mA of current are supplied to each coil, yielding a maximum magnetic dipole of 0.72 A-m^2. The magnetic dipole is comparable to other custom built CubeSat torque coils and will be compared in more detail in Section 4.8.

3.2.2.2   Reaction Wheels.

Reaction wheels provide a common means of attitude control in 3-axis stabilized spacecraft. They produce more torque than magnetorquers and are not as complicated as control moment gyros. Reaction wheels are simply flywheels attached to a motor. The motor can spin the flywheel in either direction at varying speeds to induce a torque on the spacecraft. The addition of reaction wheels changes the satellite's dynamics (Eq. 2.27) because the angular momentum vector has an additional term (although the total angular momentum stays the same). As shown in Eq. 3.3, reaction wheels are a momentum exchange system, meaning that the angular momentum of the wheels ($\boldsymbol{H}_{rotor}$) are exchanged with the angular momentum of the spacecraft ($\boldsymbol{H}_{body}$) [44].

$$\boldsymbol{H}_{s/c} = \boldsymbol{H}_{body} + \boldsymbol{H}_{rotor} \tag{3.3}$$

$\boldsymbol{H}_{rotor}$ is the moment of inertia of the reaction wheel (D) times the wheel's spin rate (ψ). Substituting Eq. 3.3 into the time differential momentum equation (Eq. 2.25) yields the kinetic equation with reaction wheels in Eq. 3.4.

$$\boldsymbol{M} = \boldsymbol{I}\dot{\omega} + \boldsymbol{D}\dot{\psi} + \omega \times (\boldsymbol{I}\omega + \boldsymbol{D}\psi) \tag{3.4}$$

where $\boldsymbol{M}$ is the external torque vector, $\boldsymbol{I}$ is the moment of inertia tensor, $\boldsymbol{D}$ is the reaction wheel's moment of inertia array, and ω is the angular velocity of the spacecraft. Eq. 3.4 is in the body frame with respect to the inertial frame, where the principal axes (x, y, and z) are aligned with the body frame.

The 2013 design of AFIT's RWA, Figure 3.8, is nearly identical to the assembly designed in 2012. The only modification was the base plate configuration, which had to accommodate the smaller base plate size of the 2013 6U CubeSat chassis. Otherwise, the wheels ($I_{wheel} = 2.6$ x 10^{-5} kg-m^2) and motors (Maxon 339259) are the same. The four-wheel design adds redundancy into the system. If one of the wheels stops working, the assembly is still fully capable of 3-axis attitude control the spacecraft.
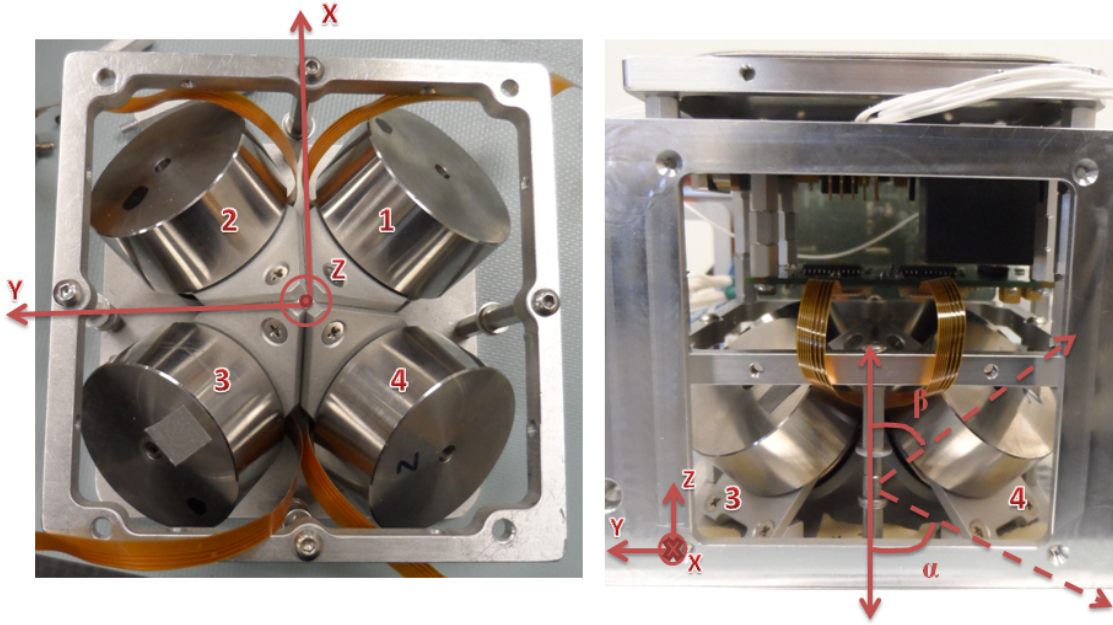
Figure 3.8: Reaction Wheel Assembly Coordinate System

Since the RWA is a four-wheel array, a transformation matrix between the four-wheel assembly and three orthogonal axes is required. The axis system in Figure 3.8 is defined by the user, but oftentimes the frame is coincident with the spacecraft's body frame. For this thesis, the RWA-body axes shown in Figure 3.8 is aligned with the spacecraft body axes, which is also coincident with the spacecraft principal axes. The configuration of AFIT's RWA yields the following transformation matrix (R^{4to3}) from four wheels to a

three-axis system.

$$R^{4to3} = \begin{bmatrix} -\cos\alpha\cos\beta & \sin\alpha\cos\beta & \cos\alpha\cos\beta & -\sin\alpha\cos\beta \\ -\sin\alpha\cos\beta & -\cos\alpha\cos\beta & \sin\alpha\cos\beta & \cos\alpha\cos\beta \\ \sin\beta & \sin\beta & \sin\beta & \sin\beta \end{bmatrix} \quad (3.5)$$

where α and β are defined in Figure 3.8. Given Eq. 3.5 and the specification of the motors, the nominal and maximum torque of the reaction wheels in the principal axes are estimated [48]. The predicted nominal and maximum torques in the x- and y-axes are 15.02 and 31.0 mN-m, respectively; the predicted nominal and maximum torque in the z-axis are 21.24 and 43.84 mN-m, respectively.

3.3   ADCS Algorithms

ADCS algorithms implement sensor measurements and satellite dynamics models to control the spacecraft as desired. Three specific ADCS algorithms will be used on board the spacecraft. The first algorithm is the QUEST algorithm for attitude determination. The two attitude control algorithms include the B-dot bang-bang controller and reaction wheel proportional-derivative control with momentum dumping capability. More algorithms can (and probably should be) implemented on the spacecraft, especially as more sensors are integrated into the ADCS suite.

3.3.1   *Attitude Determination Algorithm.*

The attitude determination algorithm used on the ADCS circuit board is the QUEST algorithm described in Section 2.1.3. The QUEST algorithm can utilize measurements from the IMU magnetometer, IMU accelerometer, and external magnetometer in any combination and weights as desired to output the estimated quaternions. As mentioned in Section 2.1.2, Rodriguez parameters encounter a singularity when the Euler axis rotation is 180°. There is a way to avoid this singularity using the method of sequential rotations [34]. However, that method has not been implemented on board the spacecraft due to time constraints in developing the ADCS software.

3.3.2 B-dot Bang-Bang Control.

Although not capable of producing as much torque as the reaction wheels, the torque coils can fully control the spacecraft if need be. In fact, given the small MOI of CubeSats, some CubeSats' attitudes are exclusively controlled magnetically [23]. Torque coils/rods alone do not provide as much pointing accuracy as reaction wheels. Nonetheless, torque coils serve as a fault protection measure in the event that the reaction wheels do not work.

One of the primary uses for torque coils/rods is de-tumbling the spacecraft. Upon ejection from the launch vehicle canister, satellites often experience large spin rates (around 6 rad/s). A simple way to stabilize the attitude of the spacecraft is to implement a B-dot controller, where B represents the magnetic field as measured on-board the spacecraft. A B-dot controller only requires a magnetometer and a magnetic actuator (torque coil or rod). The control algorithm seeks to minimize the rate of change of the magnetic field ($d\boldsymbol{B}/dt = \dot{\boldsymbol{B}}$). There are two types of B-dot control – proportional and bang-bang [21]. Proportional B-dot control commands a certain magnetic dipole ($\boldsymbol{M}$) based off of the current magnetic field change and a positive gain constant (k):

$$\boldsymbol{M} = -k\dot{\boldsymbol{B}} \tag{3.6}$$

The varying magnetic dipole corresponds to varying the current supplied to the magnetic actuator. In the event that the current to the magnetic actuator cannot be varied, a bang-bang B-dot controller is used. The bang-bang B-dot controller simply turns the magnetic actuators on and off to de-spin the spacecraft. This gives the maximum magnetic dipole ($\boldsymbol{M}_o$) whenever the actuators are on. The bang-bang controller provides the correct sign that corresponds to minimizing B-dot [21]:

$$\boldsymbol{M} = \begin{cases} -\boldsymbol{M}_o & \dot{\boldsymbol{B}} > 0 \\ \boldsymbol{M}_o & \dot{\boldsymbol{B}} < 0 \end{cases} \tag{3.7}$$

Both types of B-dot control are limited by the available torque in each axis. Since the torque produced from the torque coils acts perpendicular to the magnetic field (Eq. 3.1),

the actuators cannot produce a torque about the Earth's magnetic field vector. Nonetheless, as the spacecraft moves about its orbit and the magnetic field changes, all three axes can be controlled [50].

3.3.3 Reaction Wheel Control with Momentum Dumping.

Many control laws exist to point the spacecraft as desired [50]. The control laws are primarily feedback control laws in which the algorithm minimizes the error between the spacecraft's estimated attitude and its desired attitude. The control law employed on AFIT's 6U CubeSat, Eq. 3.8-3.10, followed the quaternion error vector control law described in Sidi's Spacecraft Dynamics and Control textbook [40].

$$T_{cx} = 2K_x q_{1E} q_{4E} + K_{xd} \omega_x \tag{3.8}$$

$$T_{cy} = 2K_y q_{2E} q_{4E} + K_{yd} \omega_y \tag{3.9}$$

$$T_{cz} = 2K_z q_{3E} q_{4E} + K_{zd} \omega_z \tag{3.10}$$

where $\boldsymbol{T}_c$ is the torque about the principal axes, $\boldsymbol{K}$ is the vector of proportional gains, $\boldsymbol{K}_d$ is the vector of derivative gains, $\boldsymbol{q}_E$ is the quaternion error array, and ω_x, ω_y, ω_z are the principal axis spacecraft angular rotation rates. The quaternion error vector, Eq. 3.11, computes the error between the current attitude direction ($\boldsymbol{q}_C$) and the target attitude quaternion ($\boldsymbol{q}_T$).

$$\boldsymbol{q}_E = \boldsymbol{q}_c^{-1} \boldsymbol{q}_T = \begin{bmatrix} q_{T4} & q_{T3} & -q_{T2} & q_{T1} \\ -q_{T3} & q_{T4} & q_{T1} & q_{T2} \\ q_{T2} & -q_{T1} & q_{T4} & q_{T3} \\ -q_{T1} & -q_{T2} & -q_{T3} & q_{T4} \end{bmatrix} \begin{bmatrix} -q_{C1} \\ -q_{C2} \\ -q_{C3} \\ q_{C4} \end{bmatrix} \tag{3.11}$$

The reaction wheel control law also utilizes the torque coils for momentum dumping. The strategy used for determining when to turn on the torque coils includes keeping track of the difference between the angular momentum of each wheel and the nominal angular momentum of each wheel (the nominal value is based off of the motor specification) ($|h_{wheel} - h_{nominal}|$), in addition to knowing the maximum angular momentum of each wheel

(h_{max}). When any one of the wheels have exceeded the maximum angular momentum, all three torque coils turn on. The torque coils continue to stay on until $|h_{wheel} - h_{nominal}|$ approaches zero. The results of this implementation are presented in Section 4.1 along with a more detailed description of the control algorithm in the next section.

3.4   Simulink Model

A satellite Simulink model was created to analyze the attitude of the satellite based off of the reaction wheel control law with momentum dumping. An overview of the Simulink model, built in MATLAB 2012b, is shown in Figure 3.9.
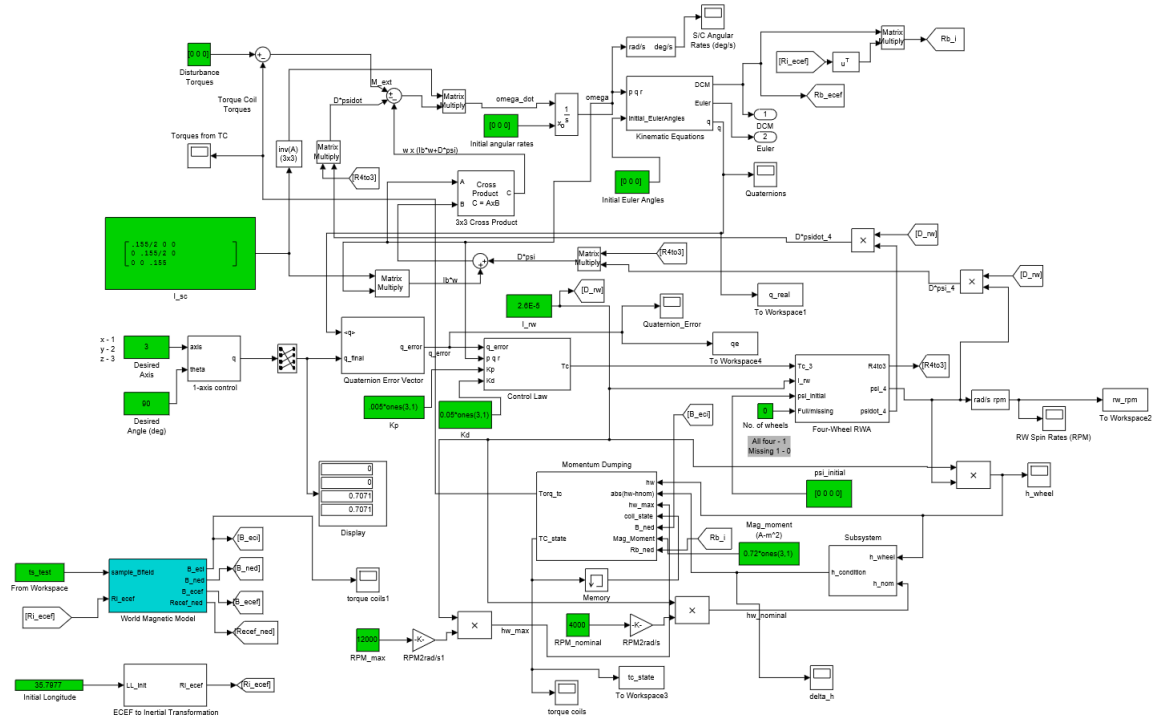

Figure 3.9: AFIT Simulink Model

Using a one second fixed-step time with the ode4 (Runge-Kutta) solver, the Simulink model integrates the satellite dynamics equation (Eq. 3.4) to solve for the angular velocity of the spacecraft. The model inputs (green boxes in Figure 3.9) include external

disturbance torques (currently zero); the MOI of the spacecraft and the reaction wheels; the proportional and derivative gains; the nominal and maximum RPM values of each wheel; the magnetic moment of a torque coil; sample altitude, latitude, and longitude information of an orbit; the initial angles and angular rates of the spacecraft and the wheels; and the desired axis and rotation about that axis. The sample orbital information came from a basic STK simulation of a satellite in LEO orbit. The orbital information was transcribed from an Excel file to a MATLAB .mat file. The first longitude value of the .mat file is the initial longitude of the ECEF to Inertial transformation block in the bottom left corner of the block diagram. In addition, the sample orbital information is used to calculate the expected magnetic field in orbit so that the torque coils could behave properly. The World Magnetic Model Simulink block from the Aerospace Toolbox was used to calculate the magnetic field in the NED coordinate frame.

The control law is currently only set up for one-axis control because the hardware testing will only involve one-axis control (to be discussed in further detail in Section 3.6.1). This is easy to change in the future to full 3-axis control, if desired. The control law first computes the quaternion error vector, from which a commanded torque is calculated and sent to the reaction wheels based off of the output of Eq. 3.8-3.10.

The reaction wheel subsystem Simulink block is shown in Figure 3.10. First, the commanded torques are translated to all four wheels by taking the pseudo-inverse of the reaction wheel transformation matrix (Eq. 3.5). The commanded torque (T_c) is equal to the moment of inertia of the reaction wheel (I_{wheel}) times its angular acceleration ($\dot{\psi}$). Integrating the commanded torque yields the commanded angular velocity of the reaction wheels, which are used to rotate the spacecraft. The model is also set up to calculate the effect of having one reaction wheel missing. The Boolean switch between all four wheels on and wheel #3 off is an input to the reaction wheel subsystem block.
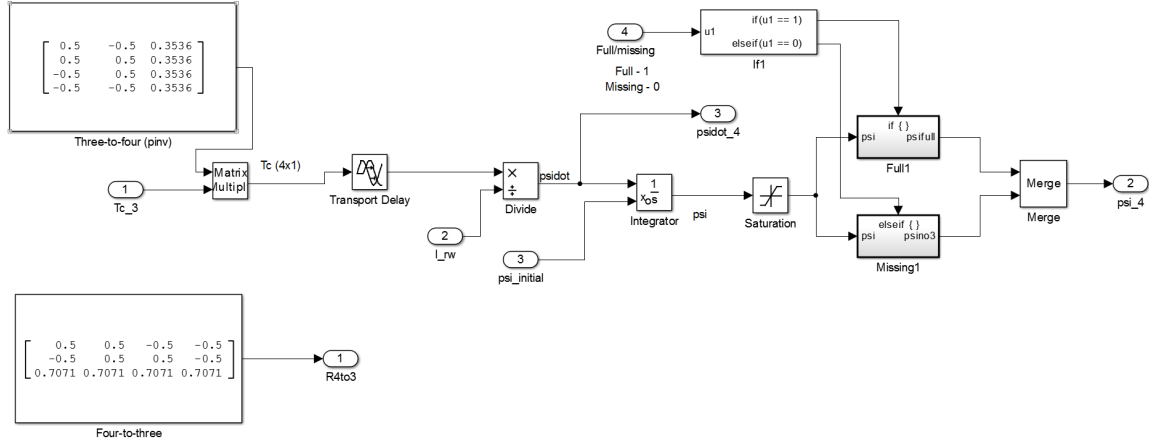
Figure 3.10: Reaction Wheel Array Simulink Model

The momentum dumping block in Figure 3.11 goes through the logic of when to turn on the torque coils in order to dump momentum from the reaction wheels. The first condition checks if any of the reaction wheels' angular momentums are above the maximum allowable angular momentum for each wheel (in both directions). If this is true, the torque coils "turn on" ($TC_{state} = 1$) and produce a torque from the cross product of the magnetic moment and the magnetic field (Eq. 3.1). The torque coils will continue to stay on if the absolute value of the difference between the current angular momentum and the nominal angular momentum (based off of the nominal wheel speed) for all wheels is above zero. Otherwise, the torque coils will turn "off".

This model demonstrates minimal functionality compared to previous models discussed (Section 2.2.1) because it does not incorporate component noises or external disturbance torques. However, the essential elements of the control law and the satellite dynamics exist in the model (and other elements can be added later). The AFIT Simulink models yields desirable results, as will be discussed in Section 4.1.
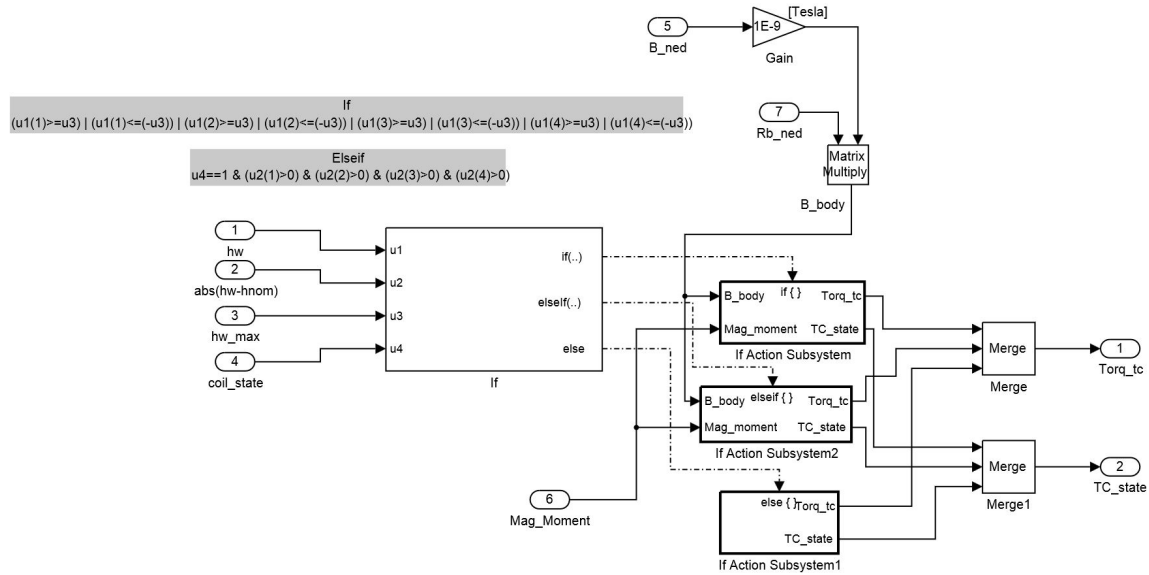
58

Figure 3.11: Momentum Dumping Using Torque Coils Simulink Model

3.5   Air Bearing Design

AFIT's spherical air bearing is a custom Nelson Air Corporation air bearing designed to minimize the bearing's moment of inertia while still being large enough to support a 6U CubeSat. Air, supplied by a "noiseless" air compressor (SIL-AIR 50D), flows through jewel nozzles on the concave part below the semisphere. The nozzles create a thin layer of air between the platform and the semisphere. The semisphere is hollow, which lowers the moment of inertia, and can hold up to 80 kg. The semisphere allows 360° motion in the z-axis and up to 35° motion in the x- and y-axes. The air bearing and platform is shown in Figure 3.12.

Originally, the test platform was designed similar to MIT's spherical air bearing (Section 2.2.3.2). A stop ring would hang below the test platform so that the test platform would not tip over. This design lowers the center of mass of the semisphere and test platform. However, the hollowness of the semisphere coupled with the final design of the test platform did not require lowering of the center of mass. When modeled with the 6U
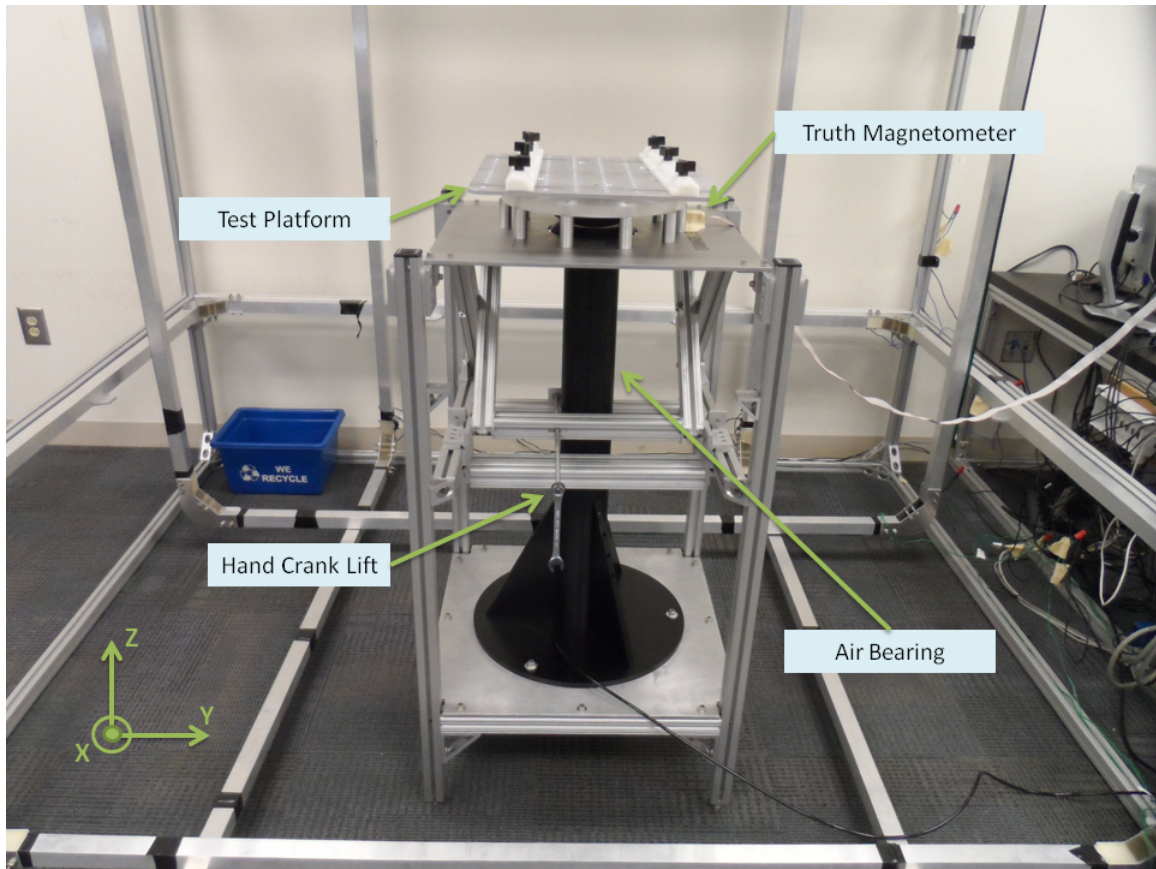
Figure 3.12: Air Bearing Platform

CubeSat on top of the test platform, the overall center of mass is still below the center of rotation (which is necessary for stability). Additionally, the stop ring design still required a means of easily removing the test platform without the semisphere resting on the air bearing cup. The semisphere should not rest on the air bearing cup so as not to scratch the semisphere surface, which could lead to a loss in the frictionless nature of the air bearing [1]. Therefore, the hand crank lift design served as the best design for the purposes of the air bearing's intended use.

The air bearing structure facilitates an easy method for one person to raise and lower the test platform through the use of a hand crank lift. The hand crank lift "parks" the test platform above the air bearing when not in use, that way the semisphere does not stay in

contact with the air bearing cup. In addition, the lift serves as a rotational stop for the off axes. The test platform comes in contact with the ring attached to the lift so that the platform does not fall over nor the semisphere come in contact with the air bearing. The ring also centers the test platform over the air bearing cup. The structure was constructed out of 15 series 80/20 aluminum with all stainless steel parts (all parts had to be non-magnetic because of its location in the Helmholtz cage).

The test platform in Figure 3.12 holds the CubeSat in position through the use of white, Delrin clamps. The clamps utilize the design of the 6U base plate, which has protruding edges that enable the CubeSat to be positioned in the PSC-CSD launch canister dispenser (see Figure 1.1). The CubeSat can move laterally within the clamps and are tightened down by the center screws. The clamps also allow horizontal movement about the test platform and are tightened in place by the four outer screws. These freedoms of movement facilitate stability of the test platform by easily positioning the CubeSat's center of mass about the center of rotation of the semisphere.

3.6   Experimental Test Setup

The following section details the CubeSat configuration for testing and its testing procedures. The final hardware and software configuration includes the necessary components to power and communicate with the test CubeSat wirelessly in addition to configuring the ADCS hardware components discussed previously. The section and chapter concludes with an overview of each test's setup and procedure, leading into the results and analysis in Chapter IV.

3.6.1   Hardware Configuration.

The CubeSat used for testing houses the primary bus components necessary for ADCS data collection and operation. This includes the CDH circuit board, the EPS circuit board, batteries (16 V), WiFly (wireless) antenna, all ADCS components, and the wiring used to connect everything. There are no payload components nor any solar panels. Even

61

though the test CubeSat is not a "complete" CubeSat, the behavior of the CubeSat will still provide valuable information about its ADCS performance. The test CubeSat configuration is pictured in Figure 3.13.
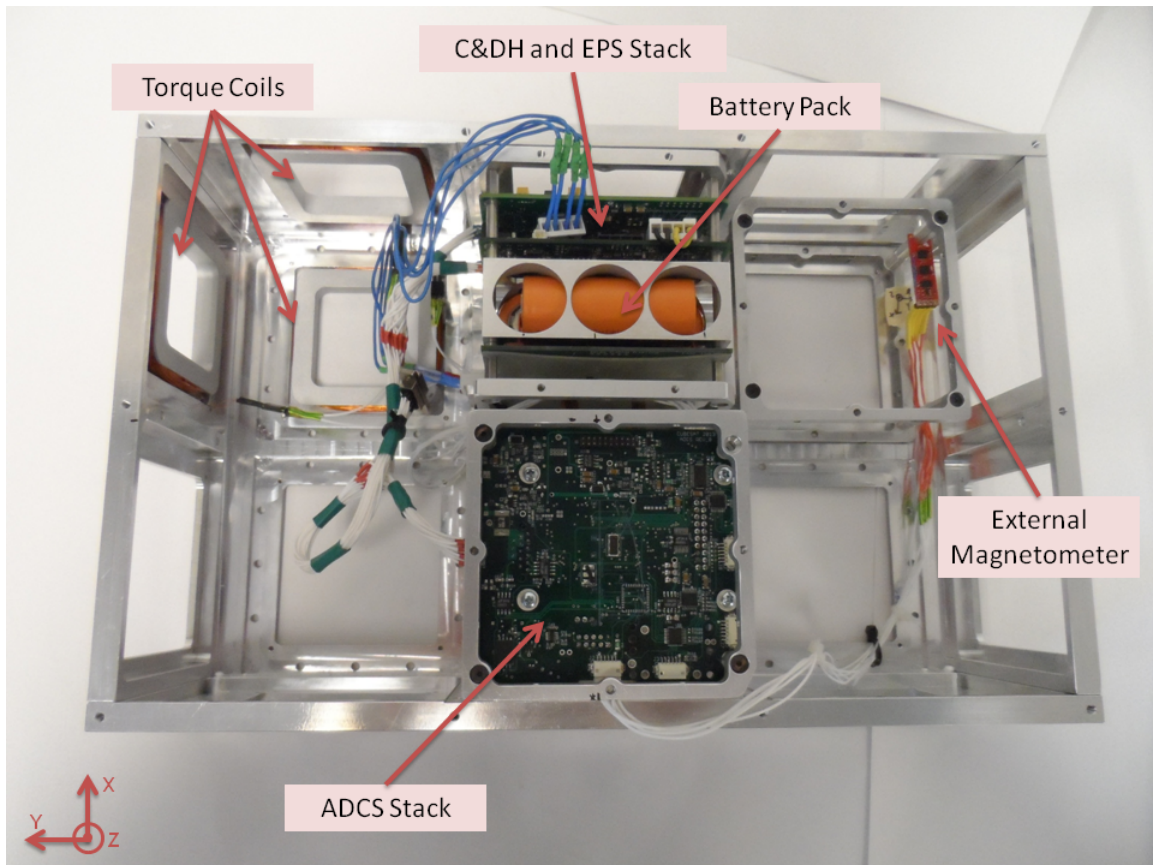

Figure 3.13: Test CubeSat with CDH and EPS Bus Components

In order for the CubeSat to be properly modeled in Simulink and balanced on the test platform, the CubeSat's center of mass and MOI needs to be measured. Acceptable center of mass and MOI values can be achieved through a highly accurate Computer-Aided Design (CAD) model. However, empirically obtained values are preferred, especially with the difficulty in modeling the wiring on the spacecraft. The COM is measured using two scales and the distance in between them (D), as pictured in Figure 3.14.
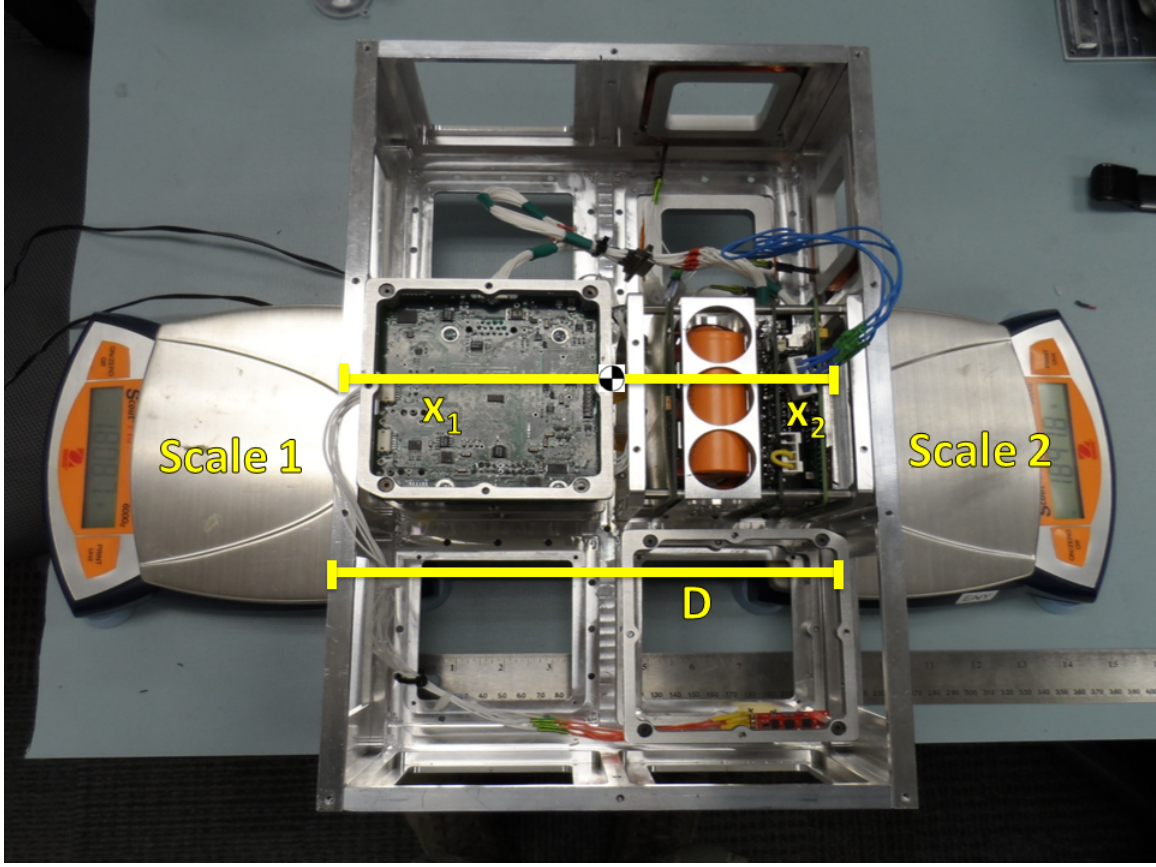
Figure 3.14: X-Axis Center of Mass Measurement Setup

The center of mass is found using the following equation:

$$x_1 = \frac{F_2 D}{F_1 + F_2} \tag{3.12}$$

where x_1 is the distance from Scale 1 to the center of mass, F_1 is the force exerted on Scale 1, and F_2 is the force exerted on Scale 2. F_1 and F_2 are based off of the mass measurements from the scale times the acceleration of gravity. The distance D is defined by the user. This method is used to find the center of mass in both the x- and y-axes.

The moment of inertia is measured using the MOI measurement device shown in Figure 3.15. The MOI measurement device oscillates during data collection and calculates the MOI based off of the period of oscillations. Initially, MOI data is collected without the

63

measured object on the oscillator to determine the MOI tare. The shortest oscillation period corresponds to the measured object's center of mass aligned with the MOI oscillator's vertical axis of rotation. Therefore, multiple tests are run by making slight adjustments to the object's position on the oscillator in order to find the shortest oscillation period. The measurement software analyzes the data and outputs a single MOI value about the chosen axis.
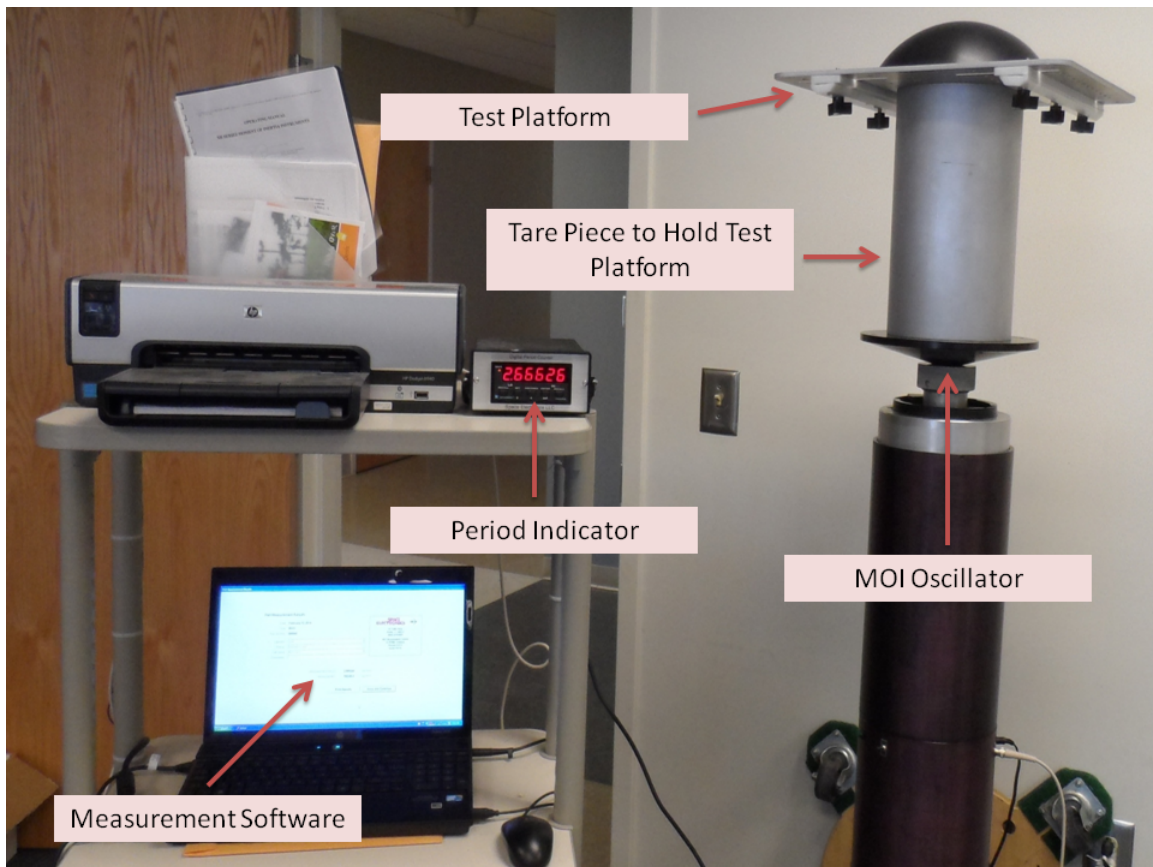

Figure 3.15: Moment of Inertia Measurement Setup

Due to time constraints, the center of mass of the test CubeSat was only determined in the x- and y-axes, and the moment of inertia was only determined in the z-axis. Because of these limitations, the test CubeSat is only statically stabilized on the air

bearing test platform, as opposed to dynamically stabilized (discussed in Section 2.2.3). Static stability is sufficient for one-axis control testing. Nonetheless, the efforts required to achieve dynamic stability are discussed in Section 5.3.5.

Using the methods discussed previously, the test CubeSat and test platform have the following mechanical properties in Table 3.1:

Table 3.1: Test CubeSat Properties

	Test CubeSat	Test Platform	Total Load Surface
Mass (kg)	3.70	4.78	8.48
Z-Axis MOI (kg-m^2)	0.0462	0.1088	0.155
X-Axis COM (m)	0.116 (from side with C&DH stack)	0.203	CubeSat aligned
Y-Axis COM (m)	0.169 (from side with torque coils)	0.203	with platform COM

The center of mass of the test CubeSat is aligned with the center of mass of the test platform to ensure air bearing stability. It is assumed that the center of mass of the test platform is in the geometric center because the test platform is symmetric. Once the two center of masses are aligned and the stability has been visually checked with the air bearing on, then the test CubeSat is clamped down and ready for air bearing testing.

The total load surface MOI is comparable to a hypothetical maximum MOI of the spacecraft. The hypothetical maximum MOI of a 6U CubeSat consists of six ADCS stacks with the RWA mounted to the base plate and no other components besides the CubeSat chassis. The ADCS stack weighs 1.24 kg. The MOI in this configuration is 0.115 kg-m^2, which is smaller than the total load surface MOI. The actuators' ability to rotate the spacecraft on the test platform will prove that the spacecraft can be rotated in space since the load surface MOI is larger than the maximum expected MOI. However, it may prove useful to consider making the test platform out of a less dense material so that the total MOI is more representative of the test CubeSat.
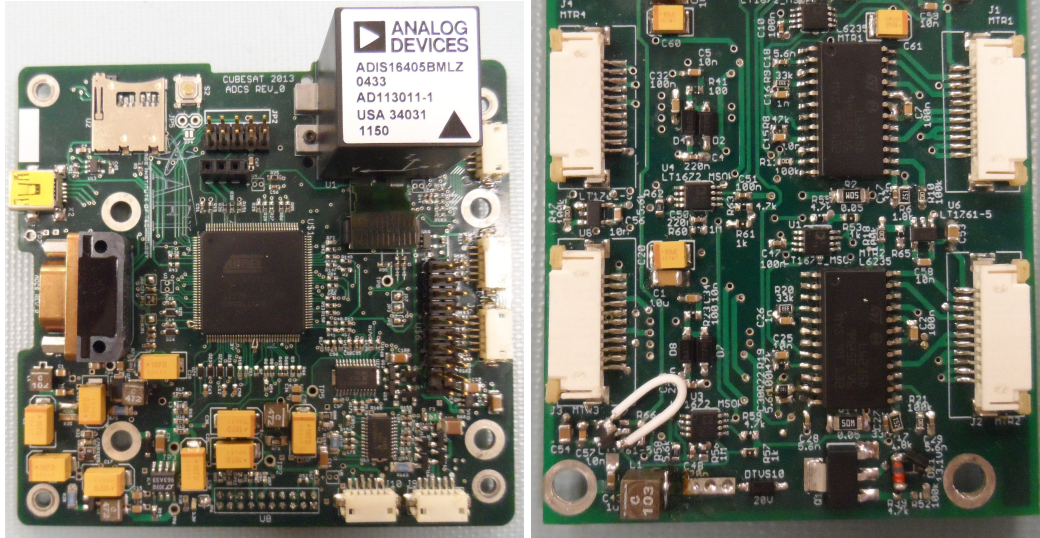
3.6.2   Software Configuration.

The ADCS uses a custom designed circuit board (Figure 3.16a) that interfaces with all ADCS components and runs the ADCS algorithms. There is also a daughter board (Figure 3.16b) for the reaction wheel motors which connects to the primary ADCS circuit board. The ADCS board has a 32-bit microcontroller (AT32UC3C 0512C) written with compiled C code in Atmel Studio 6.0. An AVR Dragon is also used for programming and debugging the microcontroller. The ADCS board regulates 12 V to 3.3 VDC. The microcontroller runs at 16 MHz, has 512 kb of boot memory RAM, has 64 kb of data memory, and uses its built-in floating-point processing unit for many of the ADCS calculations. FreeRTOS facilitates the tasking on the ADCS board. The components and tasks update at the following rates:

- IMU - 2 Hz

- External Magnetometer - 1 Hz

- Torque Coils - 5 Hz

- Reaction Wheels - 2 Hz

- QUEST Algorithm - 1 Hz

- B-dot Control Algorithm - 5 Hz

- Reaction Wheel Control Algorithm - 1 Hz

These rates are lower than desired and will be discussed in more detail in Section 4.2.

An important function for ADCS ground testing is the Inertial Value Reset (IVR) command. When the IVR command is sent, the satellite takes the current sensor measurements and sets those as the inertial values. From there, quaternion data can be collected. This is helpful in ground testing because the user can set the inertial values

66

(a) ADCS Circuit Board   (b) Motor Controller Daughter Board

Figure 3.16: ADCS Circuit Board Configurations

when the satellite is visually known to be sitting still. However, this will not work on orbit. Subsequent software development will need to include inertial reference models based off of the spacecraft's orbital position, such as a magnetic field model discussed in Section 2.1.5.

The satellite uses a custom developed MATLAB Graphical User Interface (GUI) ground station in conjunction with the on-board WiFly radio (RN-171) for command and data handling. The ground station collects all desired telemetry data in hexadecimal format, which can be reformatted and saved in a MATLAB .mat structure file for simplified analysis.

The ADCS control software was derived from a simplified model of the overall Simulink model discussed in Section 3.4. The simplified model in Figure 3.17 includes

67

the calculation of the quaternion error vector, commanded torque from the control law, and commanded angular velocity and direction for each reaction wheel. The control code programmed on the ADCS does not include momentum dumping capabilities because it was desired to first establish attitude control before adding momentum dumping code to the software. The Simulink model was converted into C code using MATLAB's automatic code generation tool. Slight modifications were made to the generated code in order to send the quaternion estimate and gyroscope outputs as inputs into the control algorithm and to send the commanded RPM output to the reaction wheel code. In addition, the initial reaction wheel spin rates ($\psi_{initial}$) were changed from zero at each time step to the last commanded RPM output at each time step. Lastly, the desired Euler angles constant block in Figure 3.17 was modified to receive a desired Euler angle input from the user through the MATLAB ground station GUI interface.
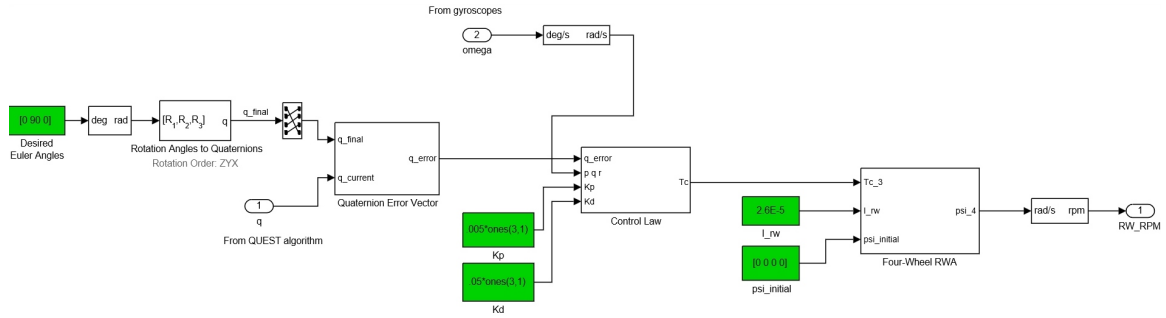

Figure 3.17: Simulink Model for Hardware Integration

3.6.3 Testing Procedures.

The following section describes the ADCS test procedures. First, the magnetometers need to be calibrated before quaternion estimation testing. Then, the reaction wheel motors can be characterized based off of the output of the motor tachometer. Once those tests are complete, the attitude control functionality and capability of the CubeSat is tested by slewing the spacecraft using the reaction wheels and torque coils, respectively.

The B-dot bang-bang control algorithm will not be tested due to a lack of model verification and time constraints. A valid model which simulates the rotation of the magnetometer in the body frame has not been developed. This research effort focused first on achieving attitude control through the use of the reaction wheel assembly.

3.6.3.1 Magnetometer Calibration.

Each magnetometer (IMU and external) needs to be calibrated in order to accurately measure the magnetic field and track the magnetic field as the satellite is moving. Inaccurate calibrations will result in undesirable attitude determination. To calibrate the magnetometers, a truth magnetometer will be used inside the zeroed-out Helmholtz cage, as defined below. The truth magnetometer is a 3-axis mG sensor from AlphaLab, Inc. [9]. The truth magnetometer is the magnetometer used for all Helmholtz cage testing and has been used in years past. The truth magnetometer will be placed on top of each CubeSat magnetometer without interfering with other electronics (a cover on top of a 1U stack provides a good mounting place). The test CubeSat will be placed in the middle of the Helmholtz cage. Using the power supplies and switch relays, the cage will be zeroed out according to the truth magnetometer. The calibration bias is then determined by simply taking the readings of the CubeSat magnetometers and then uploading those biases into the component software.

3.6.3.2 Quaternion Testing.

To validate the attitude knowledge requirement in Section 1.3 (0.1°, 3-σ), the quaternion estimation accuracy must be tested. In order to do this, the measured quaternions are compared against known reference directions. The difference between the measured and known values is an attitude knowledge accuracy in terms of degrees. The difference will never be zero because of sensor and measurement noise inherent in the system. The 3-σ value in the attitude knowledge requirement represents the acceptable standard deviation according to a Gaussian (normal) distribution (99.7% for 3-σ).

The test CubeSat will be manually rotated about a polar plot taped to a table, as shown in Figure 3.18. The CubeSat will stop and data will be recorded at 10° intervals from -90° to 90° about all three axes. The accuracy for each interval is within ±1°. The tabletop method is preferred over the use of a rotational sensor because a rotational sensor has undesired magnetic properties that affect sensor measurements, even though the accuracy is ±0.1°. In addition, a rotational sensor is often not designed to hold as much weight as the test CubeSat. This makes balancing difficult and could lead to discrepancies in assuming a single-axis rotation.

For this experiment, quaternion telemetry will be collected for about 30 seconds before manually rotating to the next rotation angle. The average value during each 30 second interval will be calculated. The quaternions will be transformed to a rotation matrix, and then the rotation matrix will be used to solve for the rotation angle based off of a single-axis rotation (using the equations in Table 2.1).
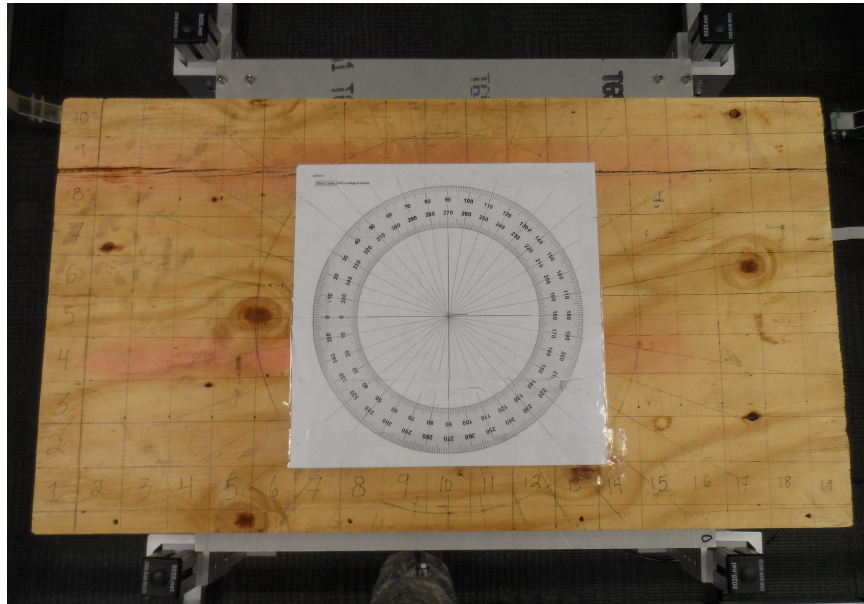

Figure 3.18: Tabletop with Compass Rose

3.6.3.3 Reaction Wheel Assembly Magnetic Effects on Magnetometer Data.

It is suspected that the inherent magnetic field induced by the reaction wheel motors alter the magnetometer measurements. The reaction wheels, coupled with other EM fields from adjacent, integrated components, could cause discrepancies in quaternion estimates using the magnetometers. Therefore, the quaternion test described above will also be run with all wheels spinning at their maximum allowable speed. These results will be compared with the results of no reaction wheel operation during quaternion testing.

3.6.3.4 Tachometer Reading Testing.

Throughout the software development process, it was determined to control the reaction wheel motor speeds and direction through Pulse Width Modulation (PWM) instead of voltage control, which was used in the previous year group's RWA development. Using PWM provides more accurate and smoother motor speed control than does voltage control. The motor speeds and direction are controlled via duty cycle counts. The PWM duty cycle counts range from 0-2000, where 1000-2000 corresponds to an increase in RPM in the forward (counter-clockwise) direction and 0-1000 corresponds to a decrease in RPM in the reverse (clockwise) direction (1000 is zero RPM; 0 is maximum RPM). The relationship between duty cycle counts and the motor tachometer readings needs to be found in order to successfully control the motors via RPM commands. The Maxon motors provide a tachometer output based off of Hall sensors next to the motor bearing. Each motor will undergo two tests - one ramping the duty cycle from 1000 to 2000 and the other test ramping the duty cycle from 1000 to 0. The tachometer readings and duty cycle counts will be recorded and analyzed to find a relationship between the two, which can then be used to program into the control software.

3.6.3.5 Attitude Control Testing.

The pointing accuracy of the CubeSat can be determined by slewing the spacecraft on top of the air bearing to a desired Euler angle. The controller will keep the CubeSat at

the desired rotation angle with minimal error about that angle. The pointing accuracy is the variation of the rotation angle error about zero degree error. Before slewing the spacecraft, the IVR command and then the desired Euler angle command is sent via the MATLAB ground station. Telemetry collection for approximately five minutes will provide enough data to determine the spacecraft's pointing accuracy.

3.6.3.6   *Torque Coil Verification Testing.*

The Helmholtz cage and air bearing can be used to verify the magnetic moment produced from the torque coils. A diagram of this test is depicted in Figure 3.19. In this
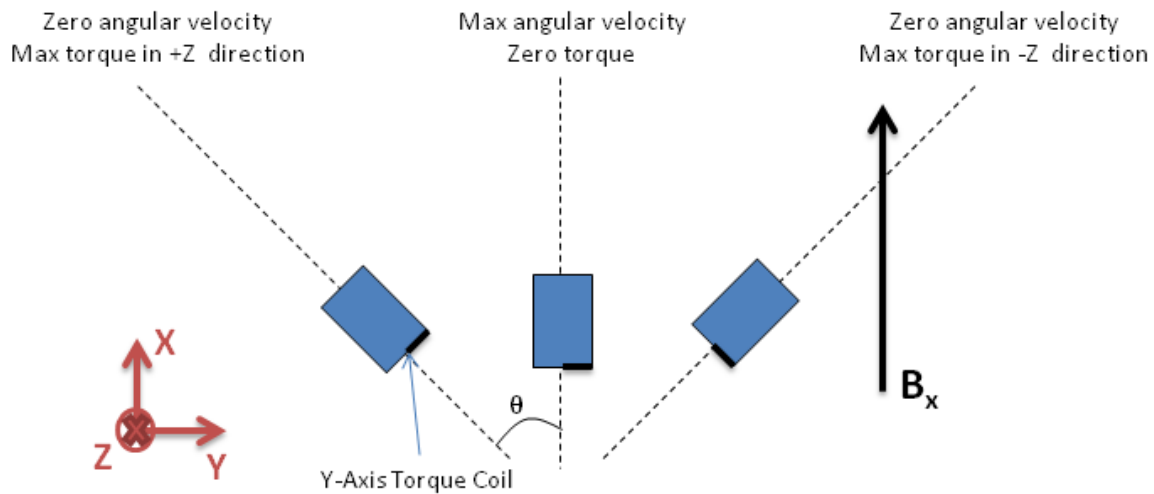

Figure 3.19: Torque Coil Verification Test Diagram

test, the magnetic field in the x-direction (B_x) is amplified to a specific level (around 2 Gauss) while the other magnetic field directions are set to zero using the power supplies for the Helmholtz cage. Only the y-axis torque coil is turned on in order to spin the spacecraft. The tests starts with the y-axis torque coil aligned with the x-axis magnetic field, as shown by the center CubeSat in Figure 3.19. At this point, there is no torque on the spacecraft because the magnetic moment produced from the torque coil is aligned with

the magnetic field (the cross product is zero). However, the spacecraft will start to spin due to disturbance torques acting on the load surface. At this point, the torque coil produces a torque on the load surface according to Eq. 3.1. The load surface stops spinning in one direction and starts spinning in the opposite direction when the torque produced from the torque coil is greater than the current angular velocity of the load surface (the torque and current angular velocity are in opposite directions). This motion continues until air drag stops the load surface, creating a sinusoidal motion about the x-axis.

The magnetic moment produced from the y-axis torque coil is calculated from the z-axis gyroscope data. By fitting a sinusoid to the gyroscope data, the angular acceleration of the spacecraft is determined from the slope of the sinusoid ($\frac{\Delta\omega}{\Delta t}$). The angular acceleration is used to calculate the magnetic moment (M) in Eq. 3.13.

$$M_y = \frac{I}{B_x} \frac{\Delta\omega}{\Delta t} \sin\theta \tag{3.13}$$

where I is the total load surface moment of inertia and θ is the observed angle between the stop position and the x-axis. θ is an approximation based off of visual observation because the quaternion estimates are not reliable during testing due to the operation of the torque coils altering the magnetometer measurements.

3.7 Chapter Summary

Chapter III detailed the design and development work done during this research effort along with setting up the ADCS test procedures. Some of the ADCS hardware was developed in previous years, especially the reaction wheel assembly. The Helmholtz cage was also developed previously and has been proven to work as intended. The IMU and external magnetometer were commercially-purchased and used to estimate the satellite's orientation from the QUEST algorithm. Sun and Earth sensor mounts were designed, but were not developed due to time constraints. Custom-built torque coils fit on the inside of the CubeSat chassis so as not to interfere with adjacent 1U stacks. Two primary attitude

control algorithms are programmed on the spacecraft. The first algorithm is B-dot bang-bang control, which uses the torque coils to de-tumble the spacecraft. The second algorithm uses reaction wheels to point the spacecraft to a desired Euler angle. In the event of reaction wheel saturation, the control algorithm will "dump" the angular momentum by turning on the torque coils. A Simulink model was developed to integrate the spacecraft equations of motion using the reaction wheel control algorithm with momentum dumping capabilities.

An air bearing hand-crank lift and test platform was designed to facilitate CubeSat air bearing testing. The hand-crank lift "parks" the CubeSat in a position above the air bearing when the air bearing is not in use. The lift also serves as protection from the CubeSat tipping over during testing. The test platform accommodates easy positioning of the satellite's center of mass with the semisphere's center of rotation so that the test platform is statically stable. The test CubeSat houses all ADCS components previously discussed in addition to a CDH circuit board, WiFly wireless antenna, EPS circuit board, and 16 Volt battery pack. The test CubeSat's center of mass and moment of inertia were measured to properly balance the CubeSat on the test platform and to accurately model the behavior of the satellite. Finally, the chapter concluded with a description of the planned test procedures, including magnetometer calibration, quaternion estimation analysis, tachometer reading analysis, pointing accuracy estimation, and torque coil verification. The results and analyses of those tests will be discussed in the next chapter.

IV.   Analysis and Results

The following chapter presents the results of the tests described in Chapter III. The results are analyzed to confirm expected or explain unexpected behaviors. Before the test results are presented, outputs of the Simulink model are described. The Simulink model outputs attempt to provide a verification reference for the hardware tests. However, as will be shown, component and software issues yield actual results different from the model predictions. Finally, the torque coil verification test is used to determine an actual magnetic moment of the torque coils.

4.1   Model Output

The Simulink model described in Section 3.4 can be used for a variety of scenarios. For this research effort, three scenarios with different control gains were analyzed. The first scenario (Test 1) had control gains that caused the reaction wheels to saturate and the torque coils to dump momentum. The second and third scenarios (Tests 2 and 3) modeled the gains used for control testing in Section 4.6. For each scenario, the spacecraft slewed 90° about the z-axis.
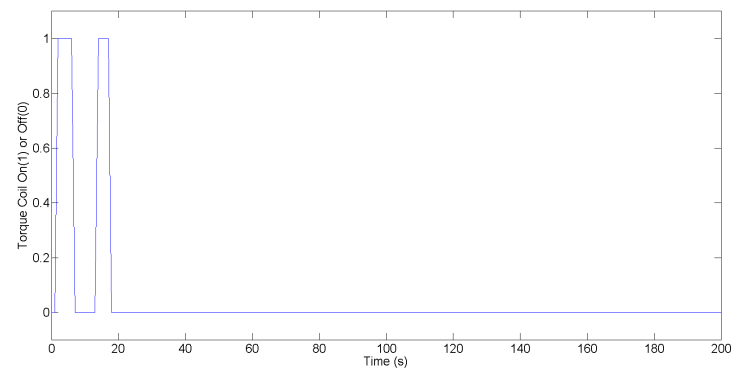
The proportional and derivative control gains for the reaction wheel saturation scenario were 0.06 and 0.01, respectively. The reaction wheels saturated at 12,000 RPM. The quaternion, reaction wheel speeds, and torque coil operations are plotted in Figure 4.1.
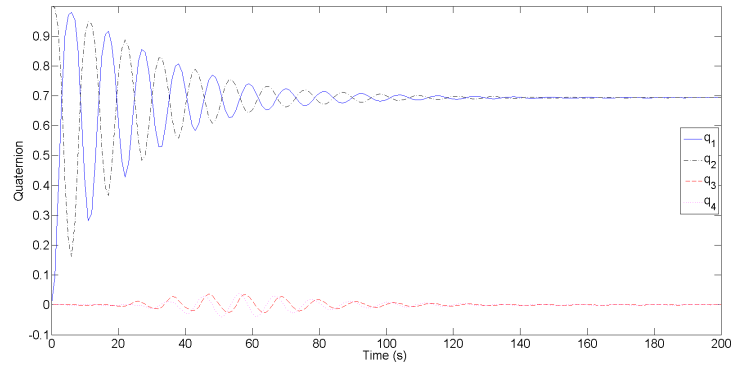
(a) Quaternion
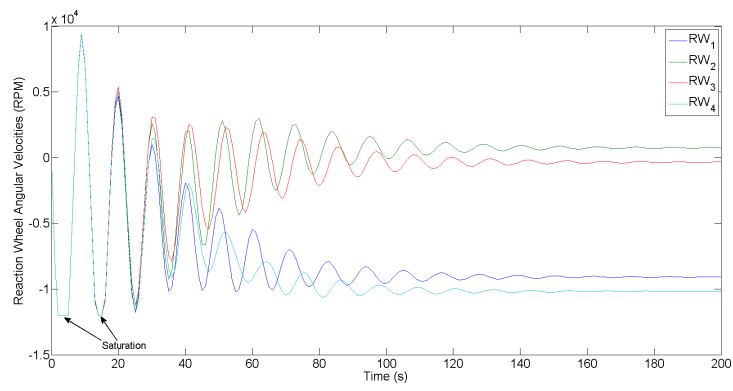
(b) Reaction Wheel Angular Velocities

(c) Torque Coil On/Off

Figure 4.1: Test 1: Reaction Wheel Saturation

As shown in Figure 4.1b, the reaction wheels saturate twice at the beginning of the scenario (around 7 and 17 seconds). When this occurs, the torque coils turn on (Figure 4.1c) until the angular momentum is below the nominal angular momentum. The quaternion plot shows that the spacecraft eventually stabilizes at the commanded 90° rotation. Although the chosen gains for this scenario are unlikely to be implemented on the spacecraft due to the slow response rate, the scenario demonstrates the ability of the torque coils to respond to reaction wheel saturation.

The second scenario uses proportional and derivative control gains of 0.005 and 0.05, respectively; the third scenario uses proportional and derivative control gains of 0.005 and 0.03, respectively. In Figure 4.2, the second scenario yields a first-order response of the rotation angle error, whereas the third scenario yields a second-order response of the rotation angle error. The smooth responses of both scenarios show that the control law and commanded torques slew the spacecraft as desired.
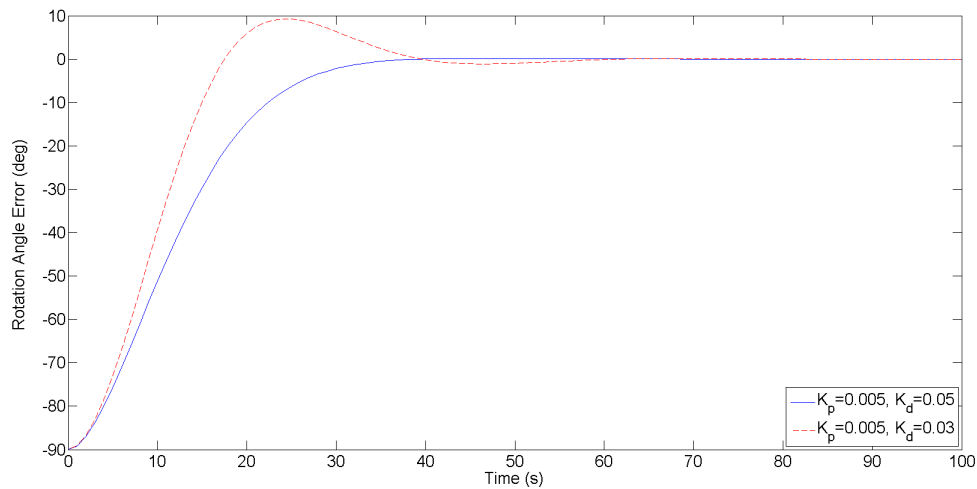

Figure 4.2: Tests 2 and 3: Rotation Angle Error using Different Derivative Gains

4.2   Software Issues

Developing the software for the ADCS components and integrated circuit board required great attention and patience. Many issues arose throughout the software development process. The external magnetometer output took longer than expected due to a faulty magnetometer board with bad I^2C communication circuit. The motor controller daughter board experienced difficulties in getting motor 3 to function properly due to an oversight in the circuit board design. Another major hurdle included controlling the reaction wheel speed and direction as desired. Initially, the reaction wheel motors were controlled using voltage through a digital to analog converter. However, the voltage control was not precise. The control was then changed to a 4-channel PWM control, which provides a relationship between the duty cycle count and the revolutions per minute (RPM) of each motor. Resistors on the circuit board needed to be changed to enable PWM control.

Towards the end of the programming process, it was determined that the circuit board was not efficient enough to update attitude determination and control tasks as desired. The update rates could not exceed 1 Hz without overflowing the memory on the circuit board. It is desired to have an attitude determination update rate of at least 10 Hz and an attitude control update rate of at least 5 Hz (based off of the update rates published in Sunde's thesis on micro-satellite attitude determination [41]). Additionally, not all components and processes have been implemented yet on the circuit board. The Sun and Earth sensors need to be added for future work. Orbit propagation models need to be computed in order to provide inertial reference models for the sensors (in particular the code for the World Magnetic Model, or similar, for magnetometer inertial reference). According to the ADCS programmer, the desired update rates are possible with the current hardware. The microcontroller processing speed needs to be increased along with eliminating unnecessary code to increase efficiency for proper memory allocation.

78

4.3   Magnetometer Calibration

The magnetometer calibration process did not follow the method described in Section 3.6.3.1. Zeroing out the magnetic field yielded a calibration bias. However, once that bias was implemented and the ADCS magnetometers were compared with the truth magnetometer outside of the Helmholtz cage, the two readings varied significantly. It appeared as if the magnetometer bias would work for one orientation of the spacecraft and then be completely different for another orientation of the spacecraft. Therefore, a new test method was used to verify what the magnetometer bias should be for all orientations of the spacecraft. The test CubeSat was placed on the flat tabletop with the taped down compass rose (Figure 3.18). The truth magnetometer was placed on top of each magnetometer (two tests were run in total). Without powering the Helmholtz cage, the CubeSat was rotated 10° for about 15 seconds each for a full 360° rotation.

The magnetometer output and measurement error results for the IMU magnetometer and the external magnetometer are shown in Figures 4.3 and 4.4. The IMU magnetometer already incorporated a bias in the software when the test was run. Nonetheless, the test showed that the y-axis bias still needed to be adjusted by at least 13°. The external magnetometer measurements matched the sinusoidal nature of the truth magnetometer. However, the initial external magnetometer axis definitions were incorrect. The x- and y-axes were flipped in the negative direction. Plotting the truth magnetometer was essential to finding this error (zeroing the magnetic field would not have caught this error). The final bias corrections added into the ADCS software are $\begin{bmatrix} -70 & -95 & 175 \end{bmatrix}$ for the IMU magnetometer and $\begin{bmatrix} 83.88 & -3.07 & -86.54 \end{bmatrix}$ for the external magnetometer.
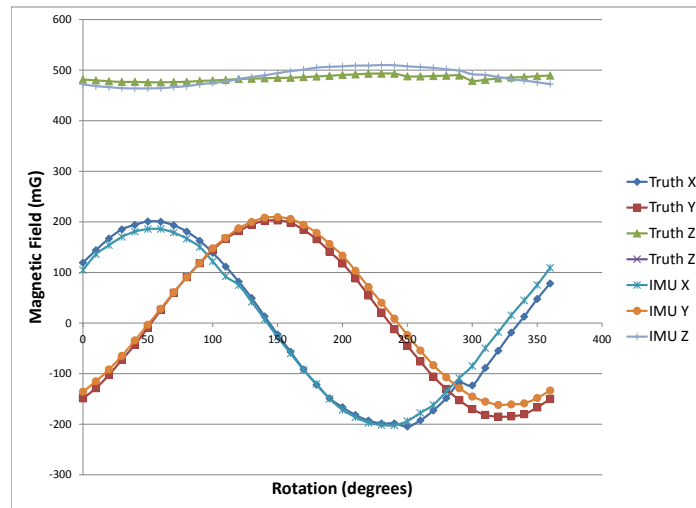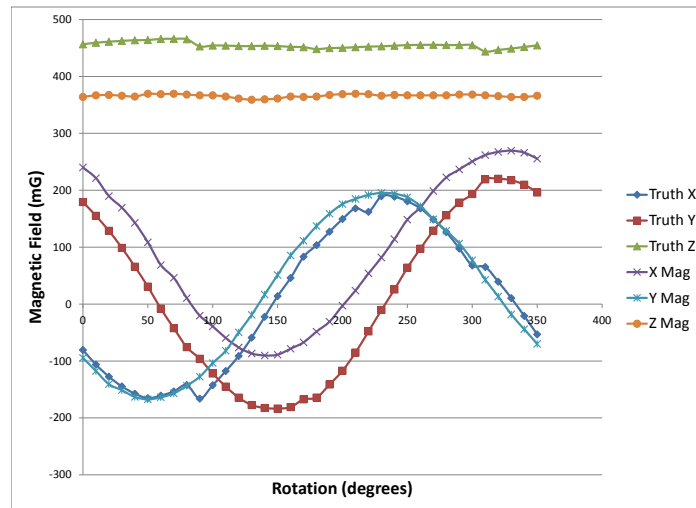
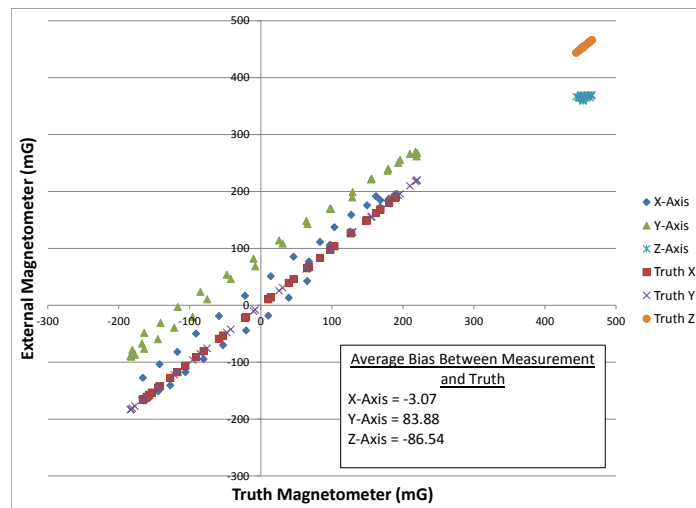(a) IMU Magnetometer and Truth Measurements
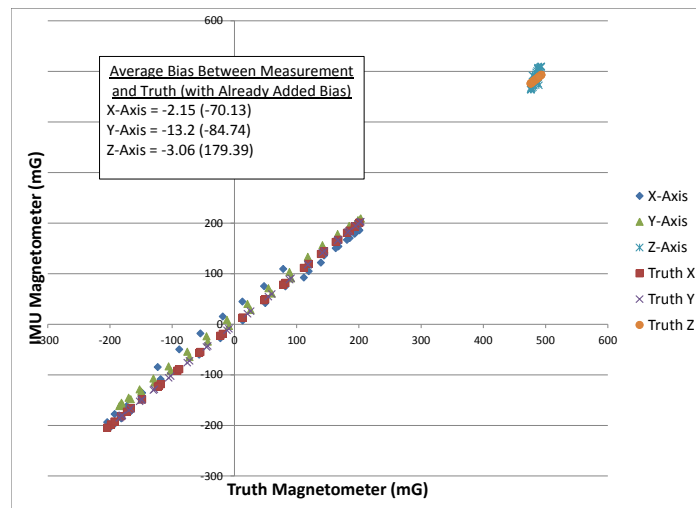
(b) IMU Magnetometer Bias Error

Figure 4.3: IMU Magnetometer Calibration

(a) External Magnetometer and Truth Measurements

(b) External Magnetometer Bias Error

Figure 4.4: External Magnetometer Calibration

4.4   Quaternion Analysis

Quaternion testing yielded valuable results, as shown in Figure 4.5. Two QUEST algorithms were used for testing. The first algorithm included the IMU magnetometer, IMU accelerometer, and external magnetometer, all with a weight of 1. The second algorithm only included the IMU magnetometer and IMU accelerometer, both with a weight of 1. The satellite was manually rotated about the compass rose board as described in the previous chapter. Measurements were taken at each degree interval for about 30 seconds. The average quaternion for each interval was determined and then used to find the rotation angle about the z-axis. The same test was accomplished with the reaction wheels spinning at 6000 RPM for both QUEST algorithms (motor 3 was not on, as will be discussed in Section 4.5). The threshold value of 6000 RPM was chosen based off of control testing at that speed. Although the wheels had a higher threshold for later testing, 6000 RPM was still sufficient to determine any negative magnetic effects on the quaternion estimation.
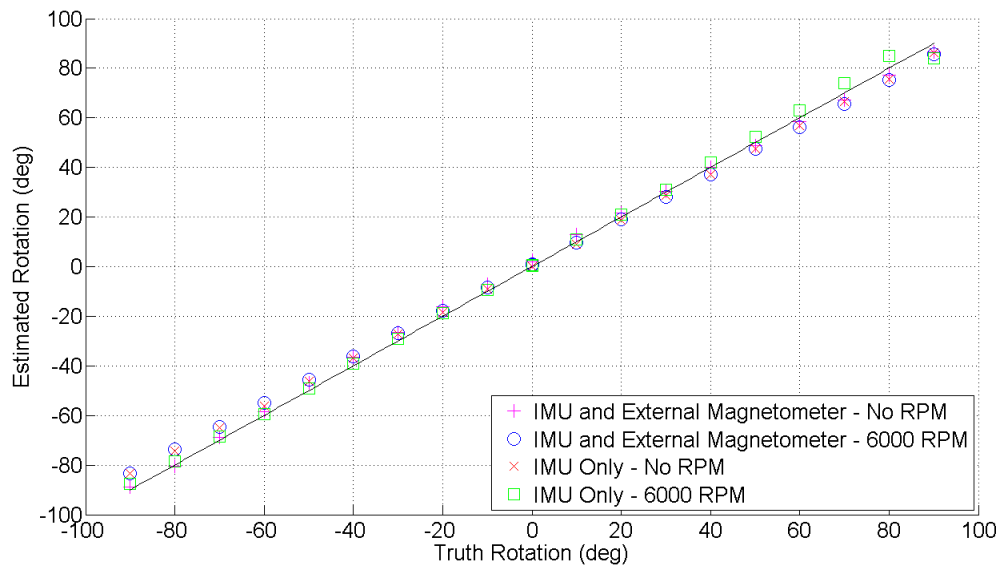

Figure 4.5: Quaternion Tracking

As the graph shows, the reaction wheels did not seem to have any negative effect on the quaternion estimate. As further proof, Table 4.1 lists the absolute angular difference from the truth and the percent error for each trial. The quaternion estimates with the IMU only and no reaction wheels spinning performed the best because it had the lowest average percent error and average degree difference. The percent error for the IMU only with reaction wheels spinning case was on par with the percent error for the IMU and external magnetometer with no reaction wheels spinning case. For all four cases, the average percent error was less than 8% and the largest degree difference was less than 7°.

Table 4.1: QUEST Accuracy Comparison

		IMU and Ext. Mag., No RPM	IMU and Ext. Mag., 6000 RPM	IMU Only No RPM	IMU Only 6000 RPM
Absolute Difference from Truth (deg)	Maximum	6.752	6.507	6.025	**3.880**
	Minimum	0.161	**0.126**	0.338	0.168
	Average	3.229	2.740	**1.773**	2.183
Percent Error	Maximum	16.372%	10.032%	**9.538%**	29.633%
	Minimum	1.607%	4.150%	0.901%	**0.420%**
	Average	7.673%	6.753%	**4.282%**	7.635%

*bolded values are minimum across all four columns

The IMU only cases performed better than the IMU and external magnetometer cases, indicating that the addition of the external magnetometer may hinder the attitude estimate. The poorer performance is most likely due to the misalignment of the external magnetometer with the spacecraft's body frame. The IMU is mounted securely on the level ADCS circuit board so that it is almost perfectly aligned with the spacecraft's body axes. However, the mount for the external magnetometer is susceptible to movement in

the x- and y-axes. Alignment is purely based off of observation, which lends itself to human error.

Current testing only includes one axis testing with the just two QUEST parameters. More testing would need to be done in order to quantify the attitude knowledge within 3-σ. In addition, testing with different QUEST parameter weights could improve or diminish the current quaternion estimation accuracy.

4.5   Tachometer Analysis

The tachometer analysis as described in Section 3.6.3.4 sought to find a relationship between duty cycle count using pulse width modulation and tachometer readings. The results in Figures 4.6 and 4.7 yielded a highly linear relationship between duty cycle count and motor tachometer output.

Two aspects of testing seemed common amongst the motors. The first aspect is the non-linear effect at high RPMs. As seen in nearly every tachometer reading plot, the RPMs increase rapidly with a small change in duty cycle count around 11,000 RPMs and higher. The maximum recorded RPM value for each motor was around 13,500 RPM. However, the maximum value according to the specification sheet is 12,000 RPMs [48]. Therefore, it is safe to say that operation beyond 12,000 RPM should not occur. In addition, a factor of safety in reaction wheel operation puts a safe maximum around 10,000 RPM. Each plot has a linear fit for the entire test data and also for RPMs from 0-10,000. The 0-10,000 RPM linear equation fit better for all motors in both directions.

The second aspect of testing that was common amongst the motors was the initial start-up value compared to the duty cycle count, often referred to as stiction. Motor 4 experienced this the least, and motors 1, 2, and 3 all shared this effect. As evident in Figure 4.6a, the RPMs did not increase until about 40 counts into the ramp up period. In Figure 4.7b, it took nearly 150 counts until the motor finally started to spin. Although the

84
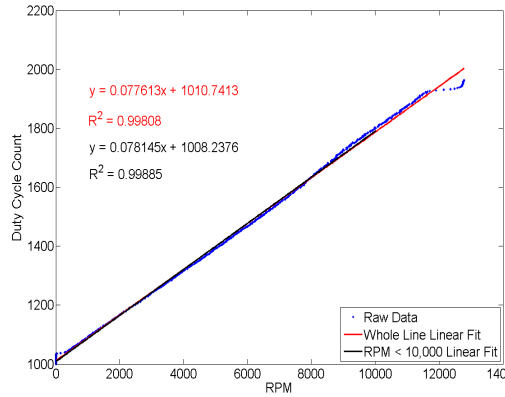
(a) Motor 1 CCW Tachometer Reading
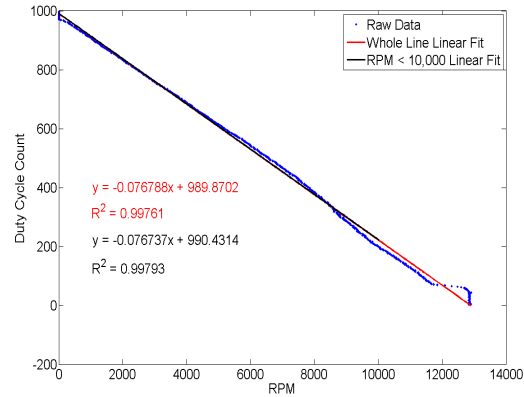
(b) Motor 1 CW Tachometer Reading
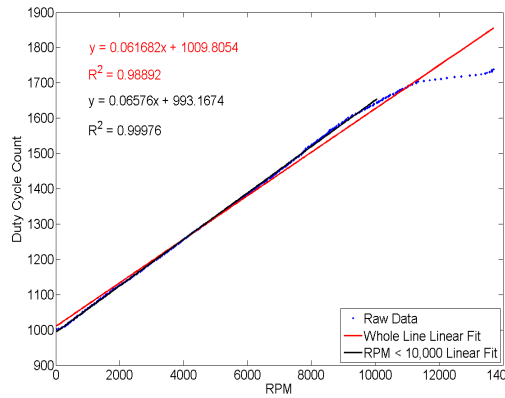
(c) Motor 2 CCW Tachometer Reading

(d) Motor 2 CW Tachometer Reading

Figure 4.6: Tachometer vs. Duty Cycle - Motors 1 and 2

linear fits have a high coefficient of determination (R^2), the duty cycles corresponding to smaller RPM values cause some implementation issues.

The linear fit equations are used in the computer software to yield a specific duty cycle given a desired RPM input. The equations worked well for most motors. However, some motors still had a short delay when starting. Also, motors 2 and 4 kept spinning when commanded to 0 RPM after already spinning at a higher RPM (most likely due to the initial delay). In order to mitigate the stiction (which can potentially grow over time),
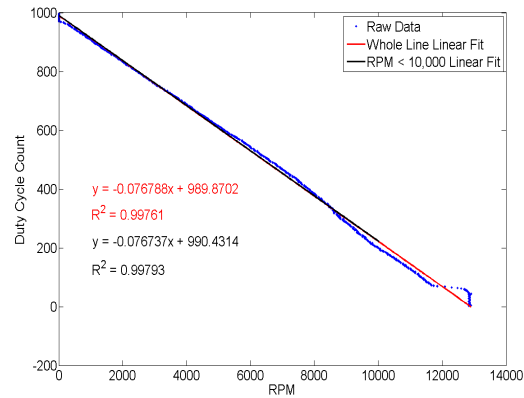
85
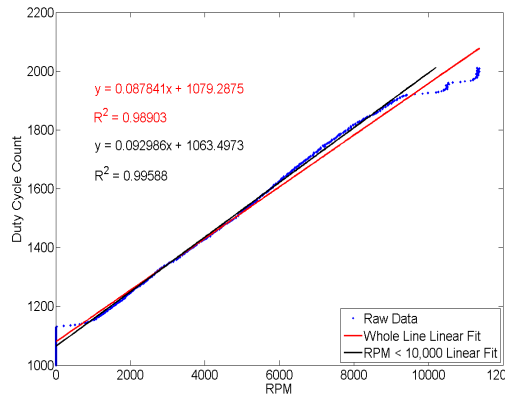
(a) Motor 3 CCW Tachometer Reading

(b) Motor 3 CW Tachometer Reading

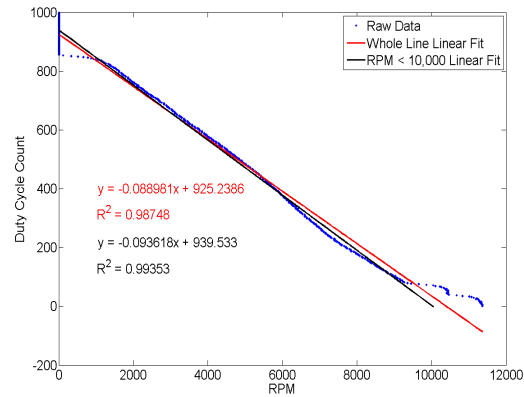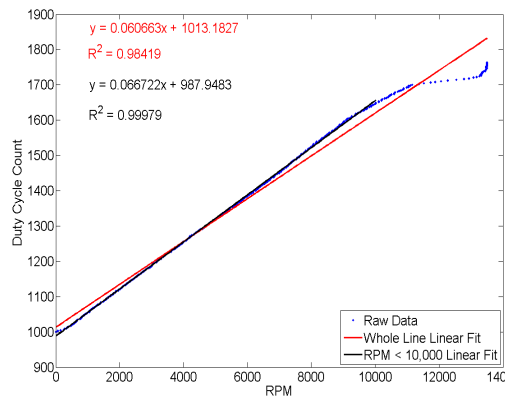(c) Motor 4 CCW Tachometer Reading
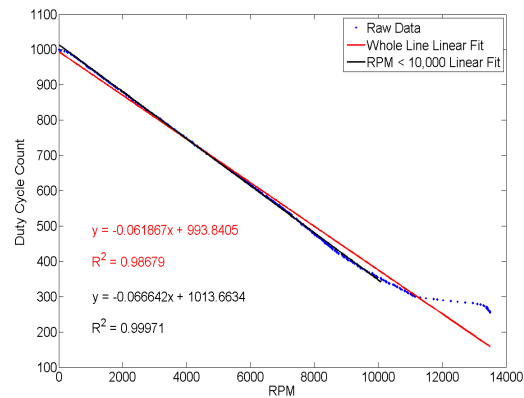
(d) Motor 4 CW Tachometer Reading

Figure 4.7: Tachometer vs. Duty Cycle - Motors 3 and 4

it is best to keep the motors spinning at a low RPM whenever possible, even if commanded to 0 RPM.

These test results and observations during motor configuration give reason to not use motor 3 for attitude control. Motor 3 still incurred the significant delay for subsequent attitude control tests that occurred during tachometer testing. On a similar note, programming motor 3 took longer than the other motors. There was a discrepancy in the pin allocation for motors 2 and 3, causing a loss in functionality of motor 3. Since there is

redundancy in the 4-wheel RWA, it is recommended that motor 3 should not be used for ADCS testing.

4.6   Tolerance and Gain Comparison

Initial tests of the control software did not work as intended. The spacecraft would move to the desired z-axis rotation angle and the reaction wheels would slow down and start spinning the other direction. However, the reaction wheels kept spinning the spacecraft the other direction without returning to the desired rotation angle. It was evident that a tolerance band (± some error off of zero) of the quaternion error vector needed to be coded into the software. Since the quaternion error vector will never truly be zero ($\boldsymbol{q}_{error} = \begin{bmatrix} 0 & 0 & 0 & 1 \end{bmatrix}$), the tolerance band enables the reaction wheels to respond accordingly when the estimated quaternion is significantly close to the desired quaternion.

The computer code for the tolerance band consisted of an if statement. If all of the quaternion errors for the first three quaternion errors were within the tolerance band (negative and positive), then the commanded torque to the reaction wheels is zero for each principal axis (which would be transformed to zero for the four reaction wheels). Three tolerance bands were tested to determine which one was the most efficient - 0.02, 0.01, and 0.005. The results of the error in rotation angle are presented in Figure 4.8. Using the air bearing, the satellite was commanded 90° about the z-axis. The reaction wheel RPM threshold was 8000 RPM. The satellite was statically stabilized, with only minimal wobbling about the x- and y-axes.

The results in Figure 4.8 show two things. First, the most efficient tolerance band is 0.01. Although the 0.005 band is closely matched with the 0.01 band, the demand on the spacecraft's computing processes is not worth the tighter tolerance. Second, the pointing accuracy of the spacecraft in this scenario is significantly and undesirably large. The 0.01 and 0.005 tolerance bands yield a pointing accuracy around 20°, whereas the 0.02
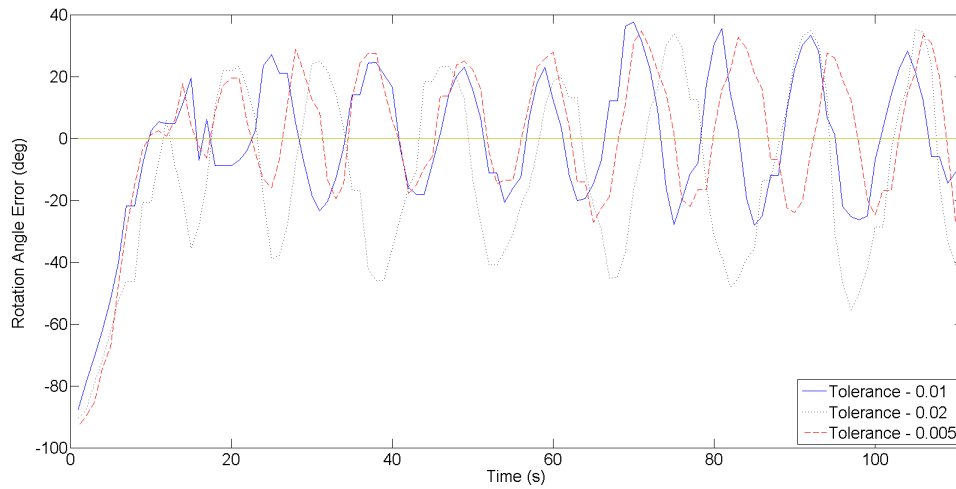
Figure 4.8: Z-Axis Rotation Error for 90° Slew Using Different Tolerance Bands

tolerance band yields a pointing accuracy around 30°. Although the pointing accuracy is always dependent on the mission, this pointing accuracy is nearly always unacceptable given pointing accuracy requirements.

The behavior of the satellite exhibits marginal stability. Given that, the natural conclusion for the cause of the marginal stability behavior is the choice in proportional and derivative control gains. The control gains were chosen from observation of the modeled response. The control gains used for the tolerance comparison were 0.005 in all three axes for the proportional gain and 0.05 in all three axes for the derivative gain. These gains produced a first-order response, as shown previously in Figure 4.2. To compare against the first-order response gains, another set of gains were chosen which produce a second-order response (also shown previously in Figure 4.2). The second-order response control gains were 0.005 in all three axes for the proportional gain and 0.03 in all three axes for the derivative gain. The results of a 90° slew about the z-axis with a 0.01 tolerance band and 8000 RPM threshold for both of these gains are shown in Figure 4.9.

88
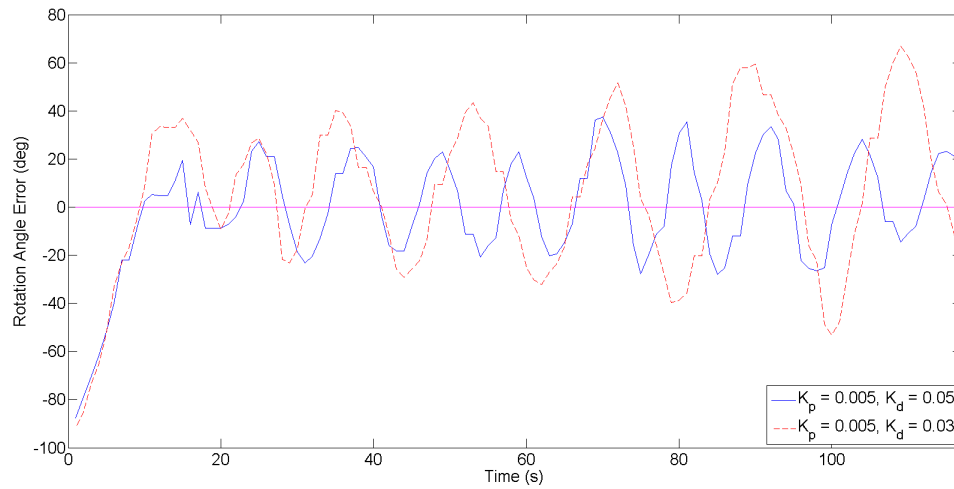
Figure 4.9: Z-Axis Rotation Error for 90° Slew Using Different Control Gains

The results in Figure 4.9 follow a first-order and second-order response, respectively. The 0.05 derivative gain settles quickly, but still exhibits a large rotation angle error. The 0.03 derivative gain overshoots initially and then seems to settle before exhibiting a similar rotation angle error. However, the rotation angle error for the second case increases over time, which indicates an unstable system. The rise times for the actual response are approximately 30 seconds faster than the rise times for the model prediction. This could be due to inadequate modeling of the reaction wheel motors in the Simulink model. Although the model does not reflect the actual hardware, it is sufficient to say that the gains for the two cases are not the cause of the large pointing accuracy because the model in Section 4.1 reflects a stable system and the actual response follows similar behavior for both cases (despite the rise time discrepancy).

The most probable cause of this undesirable accuracy is the reaction wheel and control algorithm update rates. To test this theory further, a transport delay for the commanded RPMs was added to the Simulink model. A delay as small as 2 time steps caused the system to be unstable. The Simulink model provides further evidence for the

89

undesired pointing accuracy due to the update rates. The control algorithm is only updating at 1 Hz due to limitations with the ADCS circuit board's task configuration, as discussed in Section 4.2. The powerful Maxon motors can produce a large change in RPM within 1 second. The delay between the commanded RPM and the actual RPM result in an overcompensation by the wheels and a large offshoot from the nominal quaternion.

4.7   Torque Coil Verification

The torque coil verification method described in Section 3.6.3.6 was used to measure the true magnetic moment produced from the torque coils. One test was run to determine the magnetic moment of the y-axis torque coil (it is assumed that all axes produce the same magnetic moment because they were built identically). For the test, the x-axis Helmholtz coil pairs were adjusted to 1805 mG, while the y- and z-axis pairs were adjusted to near zero mG. The y-axis torque coil was turned on in the positive direction. The torque coil induced a torque on the spacecraft when not aligned with the x-axis, causing the sinusoidal motion described in Section 3.6.3.6. The observed oscillation angle (θ) was 45°. The z-axis gyroscope data is shown in Figure 4.10.
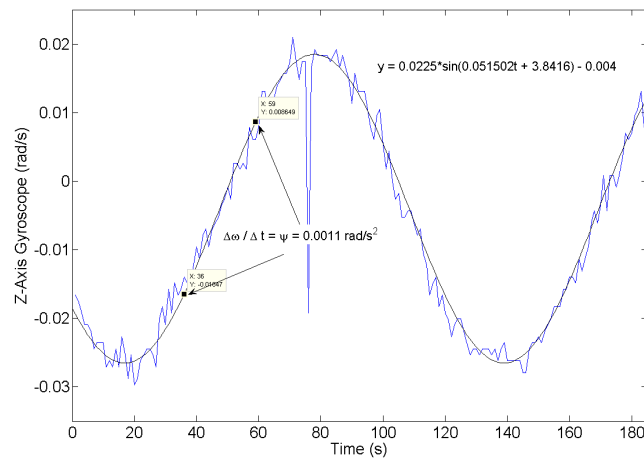

Figure 4.10: Z-Axis Gyroscope with Y-Axis Torque Coil On, B_x = 1805 mG

90

The gyroscope data is approximated by the sinusoid equation (*y*) in Figure 4.10. The slope about the two points in the figure yields the angular acceleration of the load surface. Using Eq. 3.13, the torque and magnetic moment produced from the y-axis torque coil is 1.693 x 10^{-4} N-m and 0.663 A-m^2, respectively. Compared to the predicted torque coil magnetic moment (0.72 A-m^2), the actual magnetic moment is 92.1% efficient.

4.8 Capabilities Comparison

Given the results presented and analyzed thus far, the AFIT ADCS package is compared against the COTS MAI-400 in Table 4.2. The MAI-400 is Maryland Aerospace's newest CubeSat ADCS package. The package fits within 0.5U and weighs half as much as the AFIT ADCS package. The MAI-400 uses Earth sensors and a 3-axis magnetometer for attitude determination. The reported attitude accuracy of the MAI-400 with Earth sensors is 0.2° [6]. With added sensors and measurement filtering, the AFIT attitude determination could most likely achieve this degree of accuracy. The MAI-400's actuator capabilities are smaller than AFIT's actuators capabilities primarily because of the size of their ADCS package. The MAI-400 ADCS package has all sensors and actuators in 0.5U, whereas the AFIT torque coils and external magnetometers are mounted outside of the 1U ADCS stack.

Ultimately, the decision to go with a COTS ADCS package such as the MAI-400 versus AFIT's in-house ADCS components is dependent on the mission. Each package has their advantages and disadvantages which must be assessed in the context of the mission (i.e. size, power, redundancy, etc.). Based off of its current capabilities and once it is fully developed to flight-ready status, AFIT's ADCS will serve as a viable CubeSat ADCS option.

Table 4.2: AFIT vs. COTS ADCS Package

	MAI-400 [6]	AFIT ADCS
Sensors	Earth Sensors, Magnetometer	IMU, External Magnetometer
Actuators	3 Reaction Wheels 3 Torque Rods	4-wheel RWA 3 Torque Coils
Reaction Wheel Torque	0.625 mN-m	15 mN-m (estimated)
Reaction Wheel Maximum Speed	10,000 RPM	12,000 RPM
Magnetorquer Magnetic Moment	0.15 A-m^2	0.66 A-m^2
Size	0.5U	1U
Mass	0.694 kg	1.24 kg
Power	3.2 W (steady-state)	0.46 W (steady-state without RW) 6.3 W (steady-state with RW) 20 W (peak)

4.9   Chapter Summary

Chapter IV presented the results and analysis of various attitude determination and control tests. First, three scenarios from the Simulink model with different control gains were presented. The first scenario showed the momentum dumping capability of the torque coils, and the other two scenarios showed a first- and second-order response of the spacecraft for a z-axis 90° slew. Then, the chapter explained software issues that were encountered throughout the ADCS development process. These software issues led to schedule delays and are an area of future work. The magnetometers were calibrated by rotating the spacecraft 360° at discrete 10° intervals. An average bias for each magnetometer in each axis was found. For quaternion testing, the spacecraft was manually

92

rotated from -90° to 90° to determine the quaternion estimation accuracy. It was shown that the operation of the reaction wheels do not negatively affect the quaternion estimate from the QUEST algorithm. Each reaction wheel motor was tested to determine the relationship between duty cycle count and the tachometer output. A linear relationship for each reaction wheel was found. However, the test showed that reaction wheel 3 should not be used because of its long initial start-up rate. Next, CubeSat air bearing testing explored the effect on pointing accuracy using different tolerance bands and control gains. The pointing accuracy is undesirably large due to the slow update rates of the control and reaction wheel tasks. The last experimental test determined the actual magnetic moment produced from the torque coils. The torque coils are 83% efficient and yield a magnetic moment of 0.6 A-m^2. Finally, the chapter concluded with a capabilities comparison between the MAI-400 and AFIT's ADCS package. The AFIT ADCS provides capabilities similar to and sometimes greater than the MAI-400. Nonetheless, the use of either ADCS package is dependent on the intended CubeSat mission.

V. Conclusions

5.1 Research Summary

This research focused on establishing one-axis attitude control for AFIT's 6U standard bus. As a part of university CubeSat research, AFIT is exploring the 6U CubeSat form factor, which accommodates a larger payload size and increased power capabilities. Every year, students at AFIT develop a 6U prototype based off of sponsor's needs. With each successive summer, it is envisioned that standard bus components will be further developed to facilitate easier payload integration. An ADCS unit needs to be designed and developed in order to achieve this vision.

Background research was accomplished to gain an understanding of how a spacecraft's attitude is controlled. The spacecraft attitude is the orientation of the spacecraft in reference to an inertial frame. The attitude can be represented in various ways and in different coordinate frames. The most useful attitude representation is the quaternion array because there is no singularity. The satellite dynamics equations can be used to predict the expected behavior of the satellite in orbit. The dynamics equations are used in the development of ADCS models in software such as MATLAB's Simulink.

Related research efforts were explored to gain an understanding of the current state of the art for CubeSat ADCS hardware and software. ADCS Simulink models provide useful analysis tools for various control modes and the integration of component noises. Two pieces of test equipment enable a comprehensive ADCS testing environment. A semi-spherical air bearing creates a near frictionless environment so that the load surface can rotate 360° in one direction and up to 35° in the off axes. A Helmholtz cage produces a uniform magnetic field, which can be used to simulate the magnetic field experienced in orbit.

Some of the ADCS hardware and software was developed prior to starting this research. The 4-wheel reaction wheel assembly did not require modification other than fitting the base plate to the new CubeSat chassis. In addition, the external magnetometer used in previous years proved useful in this research's attitude determination. A 3-axis IMU was used for attitude determination, and custom-built torque coils provided attitude control. Attitude control software was developed using MATLAB's automatic code generation tool for Simulink. In regards to testing, a hand-crank lift and test platform for AFIT's air bearing was designed. The lift and test platform proved invaluable because they greatly eased ADCS testing.

Various tests were performed to establish one-axis control for AFIT's ground-based ADCS. The magnetometers were calibrated in order to provide accurate quaternion estimates. A linear fit between the duty cycle and tachometer readings was found in order to properly control the reaction wheels. Although one-axis control was achieved, the spacecraft controller yielded an undesirably high pointing error. This result along with the addition of a transport delay in the Simulink model gave light to the fact that the software requires faster update rates in order to appropriately respond to the desired control. The torque coils created a sinusoidal motion of the load surface about the x-axis, allowing for the actual magnetic moment of the torque coils to be measured.

5.2   Conclusions

The AFIT ADCS sensor and actuator package is making forward progress towards a flight-ready standard ADCS bus package. However, the work is not complete. Here are the author's conclusions about the state of the requirements that were focused on for this research effort listed in Chapter I:

1. Inertially sense spacecraft attitude using at least magnetometers, Sun sensors, and Earth sensors

   The spacecraft can inertially sense its attitude using a high-precision IMU (magnetometer and accelerometer) and an optional external magnetometer. The spacecraft estimates its attitude using the QUEST algorithm, which accommodates multiple sensor measurements. The spacecraft estimates its attitude to within approximately 3° without measurement filtering (which will improve the spacecraft's attitude estimate). The design for the Sun and Earth sensors exist, but have yet to be developed.

2. Be capable of dumping momentum through the use of external torquers (preferably without propulsion)

   The theoretical momentum dumping capability was established and demonstrated through the ADCS Simulink model. In addition, the magnetic moment of the torque coils was measured and are 92% efficient compared to the predicted magnetic moment. However, momentum dumping capabilities using the air bearing have not yet been demonstrated.

3. Demonstrate ability to de-tumble spacecraft

   Similar to the previous requirement, the magnetic moment of the torque coils was measured and the directionality of each coil has been verified. The B-dot bang-bang controller has been coded in the ADCS software, but has yet to be tested.

Performance and SWAP

4. Have total ADCS power requirement no greater than 5 W

   The measured steady-state power with reaction wheels running is 6.3 W. However, the steady-state power when the reaction wheels are not running is 0.46 W. Most

likely, the majority of the time for a mission, the reaction wheels will not be spinning. Although the steady-state reaction wheel power is greater than the requirement, the maximum power could easily be different dependent upon the CubeSat mission. Therefore, the requirement is of little concern in terms of mitigation because it has not been implemented with an intended payload.

5. Have total ADCS mass requirement no greater than 1.5 kg

   The mass of the ADCS 1U stack is 1.24 kg.

6. Fit reaction wheel assembly and ADCS circuit board within 1U

   Although it is an extremely tight fit, the ADCS circuit board and reaction wheels fit within 1U. Take careful note of the configuration of the ADCS stack because it is difficult to replicate. The external magnetometer is placed elsewhere on the satellite, but does not need to be used based off of the results from quaternion testing.

Interface

7. Integrate ADCS with AFIT 6U CDH and EPS

   The test CubeSat worked as desired in terms of command and data handling. The MATLAB GUI ground station was a valuable resource that greatly aided ADCS testing. In addition, the batteries did not drain quickly, which allowed for increased testing times.

5.3 Recommendations for Future Work

The following section presents recommended work that will need to be done in order to bring the AFIT ADCS unit to full operational capability. Many of these recommendations have been mentioned previously and stem from observations of possibly incorrect assumptions and limitations and also time constraints.

5.3.1 Software Changes and Additions.

Even though the goal of 1-axis control was achieved, the ADCS software still needs to be updated for full flight capability. The major change that needs to occur is the task update rates. As mentioned in Section 4.6, the poor pointing accuracy is most likely due to the slow update rates of the reaction wheels and the attitude control algorithm. The delay between tasks is causing the wheels to overcompensate to the point that the system becomes marginally stable. A quicker update rate for nearly all tasks will greatly increase the fidelity of control.

The ADCS software requires a few additions for full flight capability. Currently, there are no inertial reference models for the sensors. The only inertial reference is the IVR command which is based off of visual observation of the spacecraft not moving. There needs to be inertial reference models for the magnetometers and other sensors to be used in the future. Some work has been started in integrating a magnetic field inertial reference model using free code for the World Magnetic Model (as provided by NOAA). However, this code needs to be developed further to the point where it can be used on the ADCS circuit board. Coupled with the inertial reference models is the need for an orbit propagator. In order for the inertial reference models to give the correct output, the satellite's position in space must be known. It is envisioned that the CubeSat will receive Two Line Elements (TLE) information from a ground station or GPS data that can be used to supplement the orbit propagator on-board the spacecraft. Regardless, there needs to be an orbit propagator somewhere in the bus software to update the inertial reference models.

More work could be done in the field of attitude determination and control filtering and optimization. Although filtering and optimization were not used for this research effort, it may be prudent to add these techniques to the current ADCS software in order to develop a more capable system. A Kalman filter would help give a better attitude estimate, especially as the spacecraft transitions from visual inertial values to orbital inertial

reference models. For attitude control, the optimal gains could be found using a linear quadratic regulator. In addition, various control laws could be explored in order to find the best one for the spacecraft (where "best" is dependent on the spacecraft's mission). There are nearly limitless possibilities for improved techniques of attitude determination and control. However, especially with the current state of the software update rates, these possibilities are limited by the physical capabilities of the ADCS circuit board.

5.3.2 Update Simulink Model.

As mentioned previously in Section 3.4, the AFIT CubeSat Simulink model is at a basic level compared to other universities' Simulink models discussed in Section 2.2.1. Further work could be done to develop the AFIT Simulink model at a level appropriate for full ADCS analysis and testing verification. This includes, but is not limited to, adding environmental torque models; adding sensor and actuator components and their associated noises; incorporating the QUEST algorithm with options for different components and measurement weights; integrating switches or logic for different control modes (i.e. b-dot control and reaction wheel control); and adding an orbit propagator for use with inertial reference models. Ultimately, the model needs to be validated against real data to ensure it captures the system's behavior accurately.

5.3.3 Characterize Magnetic Field Uniformity.

Since the Helmholtz cage moved location, the uniformity of the magnetic field has not been verified. In the previous location, the uniformity in the y-axis fluctuated because the cage was located next to a large steel support beam in the building's walls. The new location could lend itself to the same issue because it is adjacent to a wall with what is assumed similar steel beams. In addition, the objects in the room affected the Helmholtz cage in the previous location, such as a metal desk and numerous computer equipment. Although the same desks did not exist in the new location, there are other components in the new room which could affect the cage's uniformity. It is recommended to fully

characterize the uniformity of the magnetic field in the Helmholtz cage's new location by following the procedure described by Brewer [9]. If the uniformity is not as desired, a new location should be recommended within the space that is allotted to the CSRA.

5.3.4   *MOI Measurements about All Three Axes.*

Currently, only the 6U CubeSat z-axis moment of inertia can be measured because the CubeSat lies flat on the MOI measurement plate. For full, accurate modeling of the satellite, the MOIs about the other two axes need to be measured. The protruding edge on the 6U base plate does not allow for the x- and y-axes to be measured directly. An adapter holder for both the x- and y-axes would need to be designed and developed to ensure that the CubeSat is level on the MOI measurement plate. The adapter holder would also be used for center of mass measurement testing.

5.3.5   *Dynamic Stability.*

For this research, only 1-axis attitude control was tested due to the static stability of the test platform on the air bearing. Static stability aligns the center of mass of the test platform about the center of rotation of the semisphere in the x- and y-axes, but does not raise the center of mass about the z-axis so that the center of mass and center of rotation are coincident. The height difference between the center of mass and center of rotation creates a pendulum motion about the center of rotation. This creates excessive torque on the satellite if commanded to rotate about the off-axes to the point that the reaction wheels will become saturated almost immediately. Dynamic stability (center of mass and center of rotation coincident) eliminates any pendulum motion so that the satellite should stay in any orientation without high demands on the hardware.

The plate mounted to the semisphere is designed to accommodate center of mass adjustments. In addition to the CubeSat moving laterally and horizontally with the CubeSat clamps, there are threaded holes throughout the plate that can be used to raise the

center of mass. The best method in terms of modeling and adjusting the center of mass should be explored in order to ensure dynamic stability.

5.3.6 3U Modeling and Testing.

Although this project analyzed the performance of AFIT's 6U CubeSat only, the ADCS does not need to be limited to the 6U form. Further work can be done to analyze ADCS capabilities in a different form factor. Since the ADCS stack is only 1U, the stack should also work in a 3U spacecraft. The other bus stack (CDH and EPS) can also be used, leaving a 1U space for a payload. Assuming no changes in the control software's structure, the only change that would need to occur in the Simulink model is the spacecraft moment of inertia matrix. For air bearing testing, a 3U adapter plate would need to be designed and developed in order to clamp the CubeSat onto the test platform. In addition, a new test platform made of less dense material may need to be manufactured in order to lower the MOI of the test platform.

Bibliography

[1] "Air Bearing Basics". URL http://www.nelsonair.com/NA_primer.htm.

[2] "CubeTorquer Specification Page", November 2013. URL
http://www.cubesatshop.com/index.php?page=shop.product_details&flypage=
flypage.tpl&product_id=108&category_id=7&option=com_virtuemart&Itemid=69.

[3] "How Air Bearings Work", 2013. URL http://www.airfloat.com/how-it-works/.

[4] Abbate, Evelyn. "GeoLoco Final Report", September 2013.

[5] Advanced Photonix, Inc. "Red Enhanced Quad Cell Silicon Photodiode Technical
Datasheet".

[6] Aerospace, Maryland. "MAI-400 Specification Sheet". URL
http://www.miniadacs.com/miniadacs_012.htm.

[7] Alvenes, Fredrik. *Satellite Attitude Control System*. Master's thesis, Norwegian
University of Science and Technology, 2012.

[8] Branson, Jim. "Euler Angles", October 2012. URL
http://hepweb.ucsd.edu/ph110b/110b_notes/node31.html.

[9] Brewer, Captain Megan R. *CubeSat Attitude Determination and Helmholtz Cage
Design*. Master's thesis, Air Force Institute of Technology, March 2012.

[10] Brown, C.D. *Elements of Spacecraft Design*. AIAA education series. American
Institute of Aeronautics and Astronautics, Incorporated, 2002. ISBN
9781600860515. URL http://books.google.com/books?id=mTSSMhcmVbkC.

[11] Cai, Guowei, Ben M Chen, and Tong Heng Lee. *Unmanned rotorcraft systems*.
Springer, 2011.

[12] Center, NOAA National Geophysical Data. "Using the magnetic field calculator".
URL http://www.ngdc.noaa.gov/geomag-web/calculators/igrfwmmHelp. Model
description on help page of NOAA magnetic field calculator.

[13] Center, NOAA National Geophysical Data. "International Geomagnetic Reference
Field", 2010. URL http://www.ngdc.noaa.gov/IAGA/vmod/igrf.html. IGRF
Descriptive Webpage.

[14] Center, NOAA National Geophysical Data. "The World Magnetic Model", 2013.
URL http://www.ngdc.noaa.gov/geomag/WMM/DoDWMM.shtml. WMM Official
Website.

[15] Claybrook, John. "2012 ASYS 632 Final Briefing - ADCS", 2012. Presentation slides of 2012 ADCS work.

[16] Corporation, Digi-Key. "SD 085-23-21-021 Product Page", 2014. URL http://www.digikey.com/product-search/en?mpart=SD085-23-21-021&vendor=209. Purchasing page from Digi-Key.

[17] Corporation, Planetary Systems. "Flight Heritage", 2013. URL http://www.planetarysystemscorp.com/#!_flight-heritage.

[18] Crowell, Corey. *Development and Analysis of a Small Satellite Attitude Determination and Control System Testbed*. Master's thesis, Massachusetts Institute of Technology, May 2011.

[19] Devices, Analog. "ADIS 16400/ADIS16405 Triaxial Inertial Sensor with Magnetometer Data Sheet", 2009. URL http://www.analog.com/static/imported-files/data_sheets/ADIS16400_16405.pdf.

[20] Firester, Arthur H. "Design of Square Helmholtz Coil Systems". *Review of Scientific Instruments*, 37, 1966. URL http://scitation.aip.org/content/aip/journal/rsi/37/9/10.1063/1.1720478.

[21] Flatley, THOMASW, Wendy Morgenstern, Alan Reth, and Frank Bauer. "A B-dot Acquisition Controller for the RADARSAT Spacecraft". *NASA Conference Publication*, 79–90. NASA, 1997.

[22] Grewal, Mohinder S, Lawrence R Weill, and Angus P Andrews. "Appendix C: Coordinate Transformations". *Global Positioning Systems, Inertial Navigation, and Integration*, 324–369.

[23] Guerrant, Daniel. *Design and Analysis of Fully Magnetic Control for Picosatellite Stabilization*. Master's thesis, California Polytechnic State University, San Luis Obispo, June 2005.

[24] Hall, Christopher D. *Attitude Determination*. Virginia Polytechnic Institute and State University, 2003. URL http://www.dept.aoe.vt.edu/~cdhall/courses/aoe4140/attde.pdf.

[25] Janson, Siegfried, Brian Hardy, Andrew Chin, Daniel Rumsey, Daniel Ehrlich, and David Hinkley. "Attitude Control on the Pico Satellite Solar Cell Testbed-2". 2012.

[26] Kim, Jae Jun and Brij N. Agrawal. "Automatic Mass Balancing of Air-Bearing-Based Three-Axis Rotational Spacecraft Simulator". *Journal of Guidance, Control, and Dynamics*, 32(3), May-June 2009.

[27] Kirschvink, Joseph L. "Uniform Magnetic Fields and Double-Wrapped Coil Systems: Improving Techniques for the Design of Bioelectromagnetic Experiments".

Bioelectromagnetics, 13:401–411, 1992. URL http://www.lepp.cornell.edu/~critten/cesrta/ecloud/doc/Helmholtz_Kirschvink_1992.pdf.

[28] Klesh, Andrew, Sheryl Seagraves, Matt Bennett, Dylan Boone, James Cutler, and Hasan Bahcivan. "Dynamically driven Helmholtz cage for experimental magnetic attitude determination". *Advances in the Astronautical Sciences*, 135(1):147–160, 2009.

[29] Larson, Wiley J, Doug Kirkpatrick, JJ Sellers, D Thomas, and D Verma. *Applied Space Systems Engineering*. McGraw-Hill, 2009.

[30] Li, Junquan, Mark Post, Thomas Wright, and Regina Lee. "Design of Attitude Control Systems for CubeSat-Class Nanosatellite". *Journal of Control Science and Engineering*, 2013, 2013.

[31] Lim, Jun Kyu, Won Hee Lee, and Chan Gook Park. "Simulink-Based FDI Simulator for Autonomous Low Earth Orbit Satellite". *World Congress*, volume 18, 8503–8508. 2011.

[32] Macintyre Electronic Design Associates, Inc. "HCS-01 Three-Axis Helmholtz Coil Magnetic Field Source Data Sheet". Product specification sheet.

[33] Melexis. "MLX90615 Infra Rad Thermometer Specification Sheet", 2013. URL http://www.melexis.com/Infrared-Thermometer-Sensors/Infrared-Thermometer-Sensors/MLX90615-685.aspx.

[34] Mortari, Daniele, Michela Angelucci, and F. Landis Markley. *Spaceflight Mechanics 2000*, volume 105. American Astronautical Society, 2000.

[35] National Aeronautics and Space Administration. *NASA Systems Engineering Handbook*, December 2007.

[36] Poppenk, Fedde M, R Amini, and GF Brouwer. "Design and application of a Helmholtz cage for testing nano-satellites". *Delft University of Technology, The Netherlands*, 2007.

[37] Prado, J, G Bisiacchi, L Reyes, E Vicente, F Contreras, M Mesinas, and A Juárez. "Three-axis air-bearing based platform for small satellite attitude determination and control simulation". *Journal of Applied Research and Technology*, 3(03), 2010.

[38] Prinkey, Meghan. "CubeSat Attitude Control Testbed Design: Merritt 4-Coil per axis Helmholtz Cage and Spherical Air Bearing". AIAA Guidance, Navigation, and Control Conference, August 2013.

[39] Shuster, Malcolm David and S D_ Oh. "Three-axis attitude determination from vector observations". *Journal of Guidance, Control, and Dynamics*, 4(1):70–77, 1981.

[40] Sidi, M.J. *Spacecraft Dynamics and Control: A Practical Engineering Approach*. Cambridge Aerospace Series. Cambridge University Press, 1997. ISBN 9780521787802.

[41] Sunde, Bernt Ove and Jan Tommy Gravdahl. "Attitude Determination for the Student Satellite nCubeII: Kalman Filter". *56 th International Astronautical Congress*. 2005.

[42] Swenson, Eric. "Euler Angles", 2013. MECH 632 Lecture Slides.

[43] Swenson, Eric. "Notation, Reference Frames, and Rotation Matrices", 2013. MECH 632 Lecture Slides.

[44] Swenson, Eric. "Reaction Wheels", 2013. MECH 632 Lecture Slides.

[45] Tuthill, Jason D. *Design and simulation of a nano-satellite attitude determination system*. Master's thesis, Naval Postgraduate School, 2009.

[46] University, Embry-Riddle Aeronautical. Online Topic Notes. URL http://physicsx.pr.erau.edu/HelmholtzCoils/.

[47] University, Utah State. "Polar Orbiting Passive Atmospheric Calibration Spheres", 2013. URL https://sites.google.com/site/usupopacs/.

[48] USA, Maxon Motor. "Maxon Motor Specification Sheet", 2014. URL http://www.maxonmotorusa.com/maxon/view/product/motor/ecmotor/ecflat/ecflat32/339259.

[49] Wertz, James R. *Spacecraft attitude determination and control*, volume 73. Springer, 1978.

[50] Wertz, James R., David R. Everett, and Jeffery J. Puschell (editors). *Space Mission Engineering: The New SMAD*. Microcosm Press, 2011.

[51] Wie, Bong. *Space Vehicle Dynamics and Control*. AIAA, 1998.

REPORT DOCUMENTATION PAGE

1. REPORT DATE *(DD–MM–YYYY)*	2. REPORT TYPE	3. DATES COVERED *(From — To)*
27–03–2014	Master's Thesis	Oct 2012 - Mar 2014

4. TITLE AND SUBTITLE

Design and Analysis of an Attitude Determination and Control Subsystem (ADCS) for AFIT's 6U Standard Bus

5a. CONTRACT NUMBER

5b. GRANT NUMBER

5c. PROGRAM ELEMENT NUMBER

6. AUTHOR(S)

Dannemeyer, Erin R., Second Lieutenant, USAF

5d. PROJECT NUMBER

5e. TASK NUMBER

5f. WORK UNIT NUMBER

7. PERFORMING ORGANIZATION NAME(S) AND ADDRESS(ES)

Air Force Institute of Technology
Graduate School of Engineering and Management (AFIT/EN)
2950 Hobson Way
WPAFB, OH 45433-7765

8. PERFORMING ORGANIZATION REPORT NUMBER

AFIT-ENY-14-M-14

9. SPONSORING / MONITORING AGENCY NAME(S) AND ADDRESS(ES)

Space Vehicles Directorate
Air Force Research Laboratory
3550 Aberdeen SE, Bldg 497
Kirtland AFB, NM 87117
Timothy J. Shuck, Capt, USAF, (505) 853-4513, timothy.shuck@kirtland.af.mil

10. SPONSOR/MONITOR'S ACRONYM(S)

AFRL/RVES

11. SPONSOR/MONITOR'S REPORT NUMBER(S)

12. DISTRIBUTION / AVAILABILITY STATEMENT

DISTRIBUTION STATEMENT A:
APPROVED FOR PUBLIC RELEASE; DISTRIBUTION UNLIMITED

13. SUPPLEMENTARY NOTES

This work is declared a work of the U.S. Government and is not subject to copyright protection in the United States.

14. ABSTRACT

The design and testing of AFIT's 6U Attitude Determination and Control Subsystem (ADCS) are explored to establish 3-axis attitude control. The development of AFIT's 6U CubeSat standard bus is an on-going research effort designed to create in-house CubeSat bus components and software. The 6U chassis measures approximately 11 x 24 x 37 cm^3 and can have a mass up to 12 kg. The larger bus size (as compared to the more common 3U CubeSat) allows for increased power capabilities and potential to host multiple or larger payloads. Individual ADCS hardware components were either commercially purchased or built in-house and include an IMU, external magnetometer, 4-wheel reaction wheel assembly, and three torque coils. The ADCS software developed as part of this research includes the QUEST attitude determination algorithm, B-dot de-tumbling algorithm, and PD control algorithm with momentum dumping capability. To facilitate ADCS testing, an air bearing assembly was designed and set up in AFIT's existing Helmholtz cage. The air bearing provides a near-frictionless environment with $360°$ rotation about one axis and limited ($35°$) rotations about the other two axes. The Helmholtz cage consists of three orthogonal magnetic coil pairs that can create a uniform ± 2 Gauss magnetic field within the cage. This comprehensive ADCS testing environment was used to test a ground-based 6U CubeSat complete with ADCS, CDH, and EPS components. The custom-built torque coils demonstrated torquing abilities on the spacecraft and yield a 0.66 A-m^2 magnetic moment. In addition, single-axis attitude control was achieved using the reaction wheel assembly. Recommendations for further developments and testing are included to achieve the desired 3-axis control.

15. SUBJECT TERMS

CubeSat, ADCS, Simulink, Air Bearing, Helmholtz Cage

16. SECURITY CLASSIFICATION OF:			17. LIMITATION OF ABSTRACT	18. NUMBER OF PAGES	19a. NAME OF RESPONSIBLE PERSON
a. REPORT	b. ABSTRACT	c. THIS PAGE			Dr. Richard G. Cobb (ENY)
U	U	U	UU	124	**19b. TELEPHONE NUMBER** *(include area code)* (937) 785-3636 x4559 richard.cobb@afit.edu